FLUIDIC, SOLID-STATE, AND HYBRID RECONFIGURATION TECHNIQUES IN A FREQUENCY AND POLARIZATION RECONFIGURABLE ANTENNA

A Dissertation

by

JOEL DANIEL BARRERA

Submitted to the Office of Graduate and Professional Studies of
Texas A&M University
in partial fulfillment of the requirements for the degree of

DOCTOR OF PHILOSOPHY

Chair of Committee,	Gregory H. Huff
Committee Members,	Robert Nevels
	Harlan Harris
	Raktim Bhattacharya
Head of Department,	Chanan Singh

December 2014

Major Subject: Electrical Engineering

ABSTRACT

This work presents the development of a hybrid reconfiguration technique used to achieve both frequency and polarization diversity in a 2.4 – 2.5 GHz microstrip antenna. This hybrid solution for the first time combines current state-of-the-art fluidic and solid-state reconfiguration mechanisms in a collaborative effort. Two orthogonally-crossed and co-located narrow microstrip patches with gap discontinuities separating a central probe-fed section from the radiating slots provides the base antenna structure. The fluidic mechanisms use high strength dielectric fluids or liquid metal loaded across the gap discontinuities and the solid-state mechanisms uses readily available RF PIN and varactor diodes integrated across the gaps to enable reconfiguration. Accurate and robust circuit modeling concepts are presented to provide insight on antenna performance and loss mechanisms from each reconfiguration technique.

A polarization-only reconfigurable version of this antenna utilizing dielectric fluids, RF PIN didoes, and liquid metal in separate design iterations were examined to introduce design and circuit modeling concepts and provide a first comparison between the reconfiguration techniques. While all iterations achieved good linear polarization switching, dielectric fluids and the RF PIN didoes are found to have large negative impacts on radiation performance due to ohmic losses (radiation efficiencies between 8 – 35%). In the liquid metal iteration, ohmic losses are significantly reduced to boost radiation efficiencies near that of a tradition patch antenna (near 80%).

The hybrid reconfiguration solution utilizes liquid metal and solid-state varactors for polarization and frequency diversity, respectively. Non-hybrid design iterations using only dielectric fluids and solid-state RF PIN diodes with varactors provide a comparison between all reconfiguration techniques and demonstrate the advantages of the hybrid solution. It was found that broadly variable dielectric strength fluids used as a sole reconfiguration mechanism can achieve a wide frequency tuning range of 700 MHz, maintain linear polarization switching, and have radiation efficiencies near 60%. However, the fluids must have loss tangents less than 0.02 and are currently not readily available. The RF PIN and varactor diode combination provides a realizable solution, however, suffers from excessive DC control power requirements, a limited tuning range of 100 MHz, and low radiation efficiency around 16%. The hybrid solution combines the best aspects of all subsequent design iterations to achieve a realizable frequency and polarization reconfigurable antenna with a tuning range of 263 MHz and 41.7% radiation efficiency average across reconfiguration states.

DEDICATION

This thesis is dedicated to my grandparents Rosa & Octavio Guajardo and Socorro & Hector Barrera.

ACKNOWLEDGEMENTS

I would like to thank my committee chair, Dr. Huff, for his guidance and support throughout the course of this research. I would also like to thank my committee members Dr. Nevels, Dr. Harris, and Dr. Bhattacharya for taking the time to critic this work.

Thanks also goes out to my friends and colleagues and the department faculty and staff for making my many years at Texas A&M University a fantastic experience. I also want to extend my gratitude to the Louis Stokes Alliance for Minority Participation Bridge-to-the-Doctorate and National Defense Science and Engineering Graduate fellowship program for providing funding and confidence during the duration of my M.S. and PhD programs.

Finally, thanks to my mother, father, and brother for their love and encouragement during my entire graduate career.

NOMENCLATURE

ABS	Acrylonitrile butadiene styrene
DC	Direct current
DI	Deionized
EuGI	Eutectic Gallium Indium
FBW	Fractional bandwidth
FPRA	Frequency and Polarization Reconfigurable Antenna
ISM	Industrial, scientific, and medical
I-V	Current and voltage
MEMS	Microelectromechanical systems
MS	Microstrip
PDMS	Polydimethylsiloxane
PIN	P-type, intrinsic, N-type
PN	P-type and N-type
PRA	Polarization Reconfigurable Antenna
RF	Radio Frequency
SIFN	Surface-integrated fluidic network
SMA	Subminiature version A
TE	Transverse electric
TEM	Transverse electric and magnetic
TM	Transverse magnetic

TABLE OF CONTENTS

Page

ABSTRACT ii

DEDICATION iv

ACKNOWLEDGEMENTS v

NOMENCLATURE vi

TABLE OF CONTENTS vii

LIST OF FIGURES ix

LIST OF TABLES xvi

CHAPTER

I INTRODUCTION 1

II BACKGROUND 5

2.1 Network Analysis 5
2.2 Transmission Line Analysis 7
2.3 Microstrip Lines 10
2.4 Microstrip Patch Antennas 16
2.5 Diodes 22

III POLARIZATION RECONFIGURABLE CROSSED MICROSTRIP ANTENNA 27

3.1 Antenna Geometry 28
3.2 Fluidic PRA 29
3.2.1 Concept and Modeling 29
3.2.2 Design and Prototype 34
3.3 Solid-state PRA 38
3.3.1 Concept and Modeling 38
3.3.2 Design and Prototype 41
3.4 Discussion I 43

CHAPTER Page

3.5 Improved Solid-state PRA 47
3.5.1 Concept and Modeling 47
3.5.2 Design and Prototype 49
3.6 Liquid Metal PRA 52
3.6.1 Concept and Modeling 52
3.6.2 Design and Prototype 55
3.7 Discussion II 57

IV FREQUENCY AND POLARIZATION RECONFIGURABLE CROSSED MICROSTRIP ANTENNA 61

4.1 Fluidic FPRA 61
4.1.1 Concept and Modeling 61
4.1.2 Performance Study 63
4.2 Solid-State FPRA 71
4.2.1 Concept and Modeling 71
4.2.2 Control Analysis 74
4.2.3 Design and Prototype 77
4.3 Hybrid FPRA 88
4.3.1 Concept and Modeling 88
4.3.2 Design and Prototype 91
4.4 Discussion 100

V CONCLUSION 104

REFERENCES 106

APPENDIX A 109

LIST OF FIGURES

FIGURE		Page
1	Two-port network showing network variables.	5
2	Transmission line segment (a) with lumped element model (b)	8
3	Transmission line terminated with impedance Z_L	11
4	Microstrip line (a) with electric field distribution for the quasi-TEM propagating model (b)	12
5	Effective dielectric constant model with the superstrate and air replaced by a homogenous medium	12
6	Microstrip-type transmission line analysis	14
7	Rectangular microstrip patch antenna topology	16
8	Electric field distribution of TM_{010} operating mode for a rectangular microstrip patch antenna	18
9	Transmission line model for a rectangular microstrip patch antenna	18
10	Coaxial feed for a microstrip patch antenna (a) and normalized input resistance as a function of the coaxial probe position along the patch length (b)	21
11	A PN junction created by combining two semiconductors doped with positively and negatively charge impurities.	23
12	A PN junction under forward and negative bias from an external voltage.	24
13	PN junction IV characteristic.	24
14	A PN junction diode (left) and PIN junction diode (right).	25
15	Basic PRA geometry formed by co-locating two narrow microstrip patches orthogonally on a probe-fed center section. Gap discontinuities separate the feed from radiation slots.	29
16	The addition of a SIFN on the PRA formed from a superstrate with integrated fluidic channels.	30

17 The SIFN PRA circuit model based on the patch T.L. model with an admittance π-network for the gap discontinuity. 31

18 Improved circuit model for the fluidic PRA with SIFN..... 33

19 The gap capacitance C_g for a generic sampling of dielectric fluids loading the gap discontinuity at 2.45 GHz. 34

20 The gap resistance R_g for a generic sampling dielectric fluids loading the gap discontinuity at 2.45 GHz. 35

21 The prototype SIFN PRA with a PDMS superstrate for the SIFN. The DI water position for *X-pol* and *Y-pol* states are shown. 36

22 The fluidic PRA reflection coefficient from the circuit model, simulation, and measurement. 37

23 Normalized radiation patterns for the fluidic PRA at 2.4 GHz (simulation) and 2.42 GHz (measured). 38

24 The RF PIN diode PRA model with eight diodes oriented along the microstrip gap discontinuities. 40

25 The RF PIN diode PRA circuit model similar to the SIFN PRA circuit model with additional circuit components for the diodes. 40

26 The RF PIN diodes PRA model prototype. Not shown is the bias tee network feeding the antenna..... 42

27 The SIFN PRA reflection coefficient from the circuit model, simulation, and measurement. 42

28 Simulated vs. measured patterns for the RF PIN diode PRA at 2.47 GHz 43

29 Radiation efficiency as a function of RF PIN diodes forward resistance. . 46

30 Radiation efficiency as a function of loss tangent of water with the current PDMS superstrate and lossless air superstrate. 46

31 Improved performance solid-state PRA with 10 RF PIN diodes across each gap discontinuity. 48

32 Circuit model for the improved performance solid-state PRA with 10 RF PIN diodes across each gap. 48

33 Prototype for the improved performance solid-state PRA with 10 RF PIN diodes across each gap. 49

34 Reflection coefficient results for the improved solid-state PRA with 10 RF PIN diodes per gap. 50

35 Normalized radiation patterns for the improved solid-state PRA with 10 RF PIN didoes per gap. 51

36 Diagram for the liquid metal PRA with and updated version of the SIFN housing the fluidic channels 54

37 Circuit model for the liquid metal PRA. 54

38 Static prototype for the liquid metal PRA created by soldering appropriate gaps together and curing a PDMS layer over the structure..... 56

39 Measured, simulated, and circuit model reflection coefficient data for the static liquid metal PRA prototype..... 56

40 Simulated and measured normalized radiation patterns at 2.46 GHz for the static liquid metal PRA prototype..... 58

41 Effective of adding a variable series capacitance to a lumped element transmission line model..... 62

42 Fluidic FPRA with an updated SIFN identical to the SIFN in the liquid metal enabled PRA. 64

43 Circuit model for the fluidic FPRA..... 64

44 Simulated (solid) and circuit model (dashed) reflection coefficient data for the *X–pol* fluidic FPRA for a sampling of different dielectric strength loading fluids a loss tangent of 0. 66

45 Simulated (solid) and circuit model (dashed) reflection coefficient data for the *Y–pol* fluidic FPRA for a sampling of different dielectric strength loading fluids a loss tangent of 0. 66

46 Simulated (solid) and circuit model (dashed) reflection coefficient data for the *X–pol* fluidic FPRA for a sampling of different dielectric strength loading fluids a loss tangent of 0.02. 67

47 Simulated (solid) and circuit model (dashed) reflection coefficient data for the *Y–pol* fluidic FPRA for a sampling of different dielectric strength loading fluids a loss tangent of 0.02. 67

48 Simulated normalized radiation patterns for the fluidic FPRA at six different frequency states for both *X–pol* and *Y–pol* configurations. 68

49 Simulated gain at the center frequency for the dielectric constant cases from 80 to 20 and 0 and 0.02 loss tangents. 69

50 Simulated efficiency at the center frequency for the dielectric constant cases from 80 to 20 and 0 and 0.02 loss tangents. 70

51 Electrical size ratio at each tuning range for the fluidic FPRA. 70

52 Solid-state FPRA utilizing RF PIN diodes for polarization switching and varactors for frequency tuning operating under a single control voltage. 73

53 Circuit model for the solid-state FPRA. 76

54 DC circuit model for the solid-state FPRA control analysis. 76

55 Solid-state FPRA DC circuit model with a positive bias voltage applied.. 77

56 Solid-state FPRA prototype enabled by readily available RF PIN diodes and varactors. 78

57 Forward (series) resistance of the RF PIN diodes utilized in this work..... 78

58 Measured reflection coefficient for the solid-state FPRA with a bias voltage magnitude of 1 V compared to circuit model and simulated results. 81

59 Measured reflection coefficient for the solid-state FPRA with a bias voltage magnitude of 3 V compared to circuit model and simulated results. 81

60 Measured reflection coefficient for the solid-state FPRA with a bias voltage magnitude of 10 V compared to circuit model and simulated results. 82

61 Thermal image of the prototype solid-state FPRA at a bias voltage magnitude above 10 V. 82

62 Potential frequency tuning performance from the simulated solid-state FPRA model assuming a cooling mechanism could be utilized at higher bias voltages. 83

63 Measured and simulated normalized radiation patterns for the solid-state FPRA with a bias voltage magnitude of 1 V at 2.33 GHz. 84

64 Measured and simulated normalized radiation patterns for the solid-state FPRA with a bias voltage magnitude of 3 V at 2.37 GHz. 84

65 Measured and simulated normalized radiation patterns for the solid-state FPRA with a bias voltage magnitude of 10 V at 2.433 GHz. 85

66 Measured gain for the solid-state FPRA across the tuning range achieved using a bias voltage magnitude between 1 – 10 V. 86

67 Simulated radiation efficiency for the solid-state FPRA across the tuning range achieved using a bias voltage magnitude between 1 – 10 V. 87

68 Electrical size ratio for the solid-state FPRA across the bias voltage magnitude range from 1 – 20 V. 87

69 Hybrid FPRA using liquid metal fluidic channels for polarization switching and varactors for frequency tuning. 90

70 Hybrid FPRA circuit model. 91

71 Static Prototype for the hybrid FPRA where appropriate gaps have been solder together and a PDMS layer cure over the gaps to mimic a fluidic channel. 92

72 Measured reflection coefficient for the static hybrid FPRA with a bias voltage magnitude of 0 V compared to circuit model and simulated results. 94

73 Measured reflection coefficient for the static hybrid FPRA with a bias voltage magnitude of 1 V compared to circuit model and simulated results. 94

74 Measured reflection coefficient for the static hybrid FPRA with a bias voltage magnitude of 3 V compared to circuit model and simulated results. 95

75 Measured reflection coefficient for the static hybrid FPRA with a bias voltage magnitude of 5 V compared to circuit model and simulated results. 95

76 Measured reflection coefficient for the static hybrid FPRA with a bias voltage magnitude of 10 V compared to circuit model and simulated results. 96

77 Measured reflection coefficient for the static hybrid FPRA with a bias voltage magnitude of 20 V compared to circuit model and simulated results. 96

78 Measured reflection coefficient for the static hybrid FPRA with a bias voltage magnitude of 30 V compared to circuit model and simulated results. 97

79 Measured and simulated normalized radiation patterns for the static hybrid FPRA with a bias voltage magnitude of 0 V at 2.365 GHz. 97

80 Measured and simulated normalized radiation patterns for the solid-state FPRA with a bias voltage magnitude of 10 V at 2.52 GHz. 98

81 Measured and simulated normalized radiation patterns for the solid-state FPRA with a bias voltage magnitude of 30 V at 2.63 GHz 98

82 Measured gain for the hybrid FPRA across the frequency tuning range achieved using a bias voltage magnitude between 0 – 30 V. 99

83 Simulated efficiency for the hybrid FPRA across the frequency tuning range achieved using a bias voltage magnitude between 0 – 30 V. 100

84 Electrical size ratio for the hybrid FPRA across the bias voltage magnitude range from 1 – 30 V 100

85 HFSS diode simulation model 109

86 Simulation model for computing sheet inductance. 110

LIST OF TABLES

TABLE		Page
1	Limits and physical interpretations of two-port *S* parameters.	6
2	Performance summary for the PRA with the fluidic, solid-state, and liquid metal reconfiguration mechanisms.	58
3	DC control parameters for the solid-state FPRA prototype.	80
4	Performance summary for the FPRA with the fluidic, solid-state, and hybrid reconfiguration mechanisms.	101

CHAPTER I

INTRODUCTION

Wireless applications have illustrated the need for multipurpose and multifunctional antennas with reconfigurable frequency, polarization, and/or other adaptable parameters. For example, in applications involving a multipath environment and gyratory/rotating objects, such as personal communication systems or satellites, polarization diversity can be an essential component for enhancing signal performance (such as reducing fading or improving basic connectivity). Likewise, intelligent cognitive radio applications require consistent updates to operational parameters, such as operating frequency and polarization, in response to the observed RF environment for maximum radio spectrum utilization.

Microstrip patch antennas have provided a lightweight, low profile, and inexpensive vehicle for many of these applications, and polarization diversity and frequency tuning have been achieved by integrating different solid-state approaches such as varactors [1-4], RF PIN diodes [5-8], and RF-MEMS [9-11] on or near the antenna surface. In [1], the authors achieve a widely frequency agile microstrip patch antenna by integrating three pairs of varactor diodes along with a broadband differential feeding scheme. Furthermore, the authors develop a circuit model to analyze the effects on radiation efficiency from the varactor diodes losses. A polarization and frequency reconfigurable dual-feed square-ring microstrip patch antenna using two varactor diodes is described in [2]. In [3], a frequency agile multi-band microstrip antenna is achieved

using one varactor diode connecting a semicircular patch to outer half-rings. An electrically small, frequency reconfigurable microstrip-like antenna structure utilizing three varactor diodes is achieved in [4], and the tuning band enhancement is explained through an equivalent circuit analysis. In [5, 6], current distributions and/or current paths are manipulated using RF PIN diodes to switch between right hand and left hand circular polarization. Multiple polarization schemes (linear, circular, and quadri-polarization) are achieved in [7, 8] using RF-PIN diodes on the feed structure to reduced radiation losses caused by the RF diodes. In [9], a frequency reconfigurable pixel slot antenna is achieved using RF MEMS switches. Lastly, a polarization reconfiguration microstrip patch antenna using RF MEMS switches is presented in [10, 11]. These examples illustrate a mere sample of what has been achieved in the literature, showing the large scope of adaptive and/or reconfigurable antennas using current solid-state state-of-the-art mechanisms.

As a unique alternative, the use of dielectric liquids in fluidic channel networks have been incorporated in RF/microwave devices to serve as the tuning mechanisms. A variable dielectric constant fluid composed of high dielectric particles dispersed in low dielectric oil has been utilized to provide continuous tuning in a frequency tunable dielectric resonator antenna [12], impedance transformer [13], reflect array element for beam steering [14], and frequency reconfigurable substrate integrated waveguide resonator [15]. The authors of [15] discuss the limitations due to high losses when using this variable fluid. However, [12-15] all demonstrate the versatility and potential of implementing these fluidics in RF/microwave devices and antennas to achieve large tuning ranges. Similarly, liquid metals dispersed through fluidic channels have been

implemented in RF/microwave devices and antennas as the primary reconfiguration mechanism. A frequency reconfigurable slot antenna is achieved by displacing liquid metal in an air-filled microchannel to capacitively load the slot and alter its operating frequency in [16]. Liquid metal channels along a microstrip patch antenna are used to physically length the patch for frequency reconfiguration in [17].

In this work a hybrid reconfiguration technique employing both fluidic and solid-state mechanisms is examined in an antenna composed of two orthogonally-crossed and co-located narrow microstrip patches with gap discontinuities separating a central probe-fed section from the radiating slots. The reconfiguration mechanisms are incorporated/integrated along the gaps to capacitively couple or electrically connect antenna arms to a feed section and excite orthogonal polarization states. These techniques can also introduced a variable series capacitance across the gaps to alter the antenna resonant frequency at any polarization state. In the fluidic approach, a pressure driven surface-integrated fluidic network (SIFN) on the antenna surface displaces periodically positioned fluids or liquid metals across the gaps on the antenna's surface. In the solid-state approach, packaged RF PIN diodes and varactor diodes are placed across the microstrip gap discontinuities. The hybrid solution incorporates both these reconfiguration techniques. Circuit models are developed to analyze the impacts on antenna performance from the presence of each reconfiguration mechanism. The models predict the reflection coefficient frequency response, point out ohmic losses, and helps develop an intuitive understanding for the antenna's operation with a specific tuning mechanism present. The reconfiguration mechanisms are examined on seven main performance metrics: (1)

frequency tuning range, (2) electrical size, (3) gain, (4) radiation efficiency, (5) cross polarization level, (6) power requirements, and (7) switching speed. For a fair comparison to be made, the reconfiguration techniques are incorporated with reduced complexities in the control schemes (i.e. number of bias lines and control voltages are minimized). This allows the antenna's basic geometry to remain intact for all tuning mechanism iterations.

A polarization-only reconfigurable antenna (PRA) design with fluidic and solid-state reconfiguration techniques presents the basic antenna geometry, circuit model analysis/development, fabrication techniques, and comparison breakdown. The frequency and polarization reconfigurable antenna (FPRA) design proceeds by, again, incorporating fluidic and solid-state reconfiguration techniques on the antenna. From the observations and findings of these PRA and FPRA design iterations, a hybrid reconfiguration approach for the FPRA is developed and presented. A background chapter proceeds to familiarize the reader with important concepts used in this dissertation.

CHAPTER II

BACKGROUND

2.1 Network Analysis

In this work basic two-port network analysis techniques and concepts are applied to microstrip antennas and their equivalent circuit models. Fig. 1 shows a two-port network with its corresponding variables. The two-port network analysis from [18] follows. Voltmeters and ammeters for directly measuring the voltages and currents in Fig. 1 at microwave frequencies do not exist. Network analyzers measuring the reflected and transmitted waves across a microwave network are utilized instead. However, describing a network in terms of circuit components, voltages, and currents aid electrical engineers in the design process of microwave/RF antennas and devices.

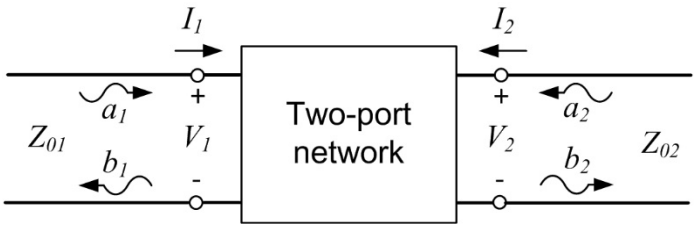

Fig. 1. Two-port network showing network variables.

The *S* parameters of a two-port network relate the incident and reflected or transmitted waves at specific ports and are directly measureable by a network analyzer. The *S* parameters defined in terms of the network wave variables in Fig. 1 are

$$S_{11} = \left.\frac{b_1}{a_1}\right|_{a_2=0} \qquad S_{12} = \left.\frac{b_1}{a_2}\right|_{a_1=0}$$
$$S_{21} = \left.\frac{b_2}{a_1}\right|_{a_2=0} \qquad S_{22} = \left.\frac{b_2}{a_2}\right|_{a_1=0}, \tag{2.1}$$

where $a_n = 0$ implies a perfect impedance match at port n. The S parameters of a two-port network can also be written as a set of linear equations in matrix notation as

$$\begin{bmatrix} b_1 \\ b_2 \end{bmatrix} = \begin{bmatrix} S_{11} & S_{12} \\ S_{21} & S_{22} \end{bmatrix} \begin{bmatrix} a_1 \\ a_2 \end{bmatrix}. \tag{2.2}$$

The general parameter S_{mn} is read as the S parameter from port "n" to port "m". Thus, the S_{11} and S_{22} parameters are the reflection coefficients, and S_{12} and S_{21} are the transmission coefficients. The S parameter magnitudes are often expressed in decibels (dB) as

$$\left|S_{mn}\right|_{dB} = 20\log\left|S_{mn}\right|. \tag{2.3}$$

The limits and physical interpretations of S parameters are defined in Table 1.

Table 1. Limits and physical interpretations of two-port *S* parameters.

Parameter / Value	S_{11}	S_{12}	S_{21}	S_{22}
0 ($-\infty$ dB)	Total transmission through port 1	Zero transmission from port 2 to 1	Zero transmission from port 1 to 2	Total transmission through port 2
1 (0 dB)	Total reflection at port 1	Total transmission from port 2 to 1	Total transmission from port 1 to 2	Total reflection at port 2

2.2 Transmission Line Analysis

In classical circuit analysis the physical distance between two circuit components or nodes is much smaller than the electrical wavelength. At RF and microwave frequencies, transmission lines may be fractions of a wavelength or many wavelengths in size. A distributed parameter network where voltages and currents may vary in magnitude and phase over the length best describes a transmission line at high frequencies [18]. Fig. 2 shows a general two-wire transmission line and its equivalent lumped-element circuit model for an infinitesimally small segment of length Δz. At RF/microwave frequencies, a minimum of two conductors are need to from transverse electric and magnetic (TEM) propagation. The circuit parameters are defined as follows:

R = series resistance per unit length, for both conductors, in Ω/m.

L = series inductance per unit length, for both conductors, in H/m.

G = shunt conductance per unit length, in S/m.

C = shunt capacitance per unit length, in F/m.

The series inductance L represents the total self-inductance for both conductors. The shunt capacitance C represents the capacitance created from the conductors close proximity to each other. The series resistance R and shunt conductance G represent conductive loss from the conductors and dielectric losses from the material separating the conductors, respectively.

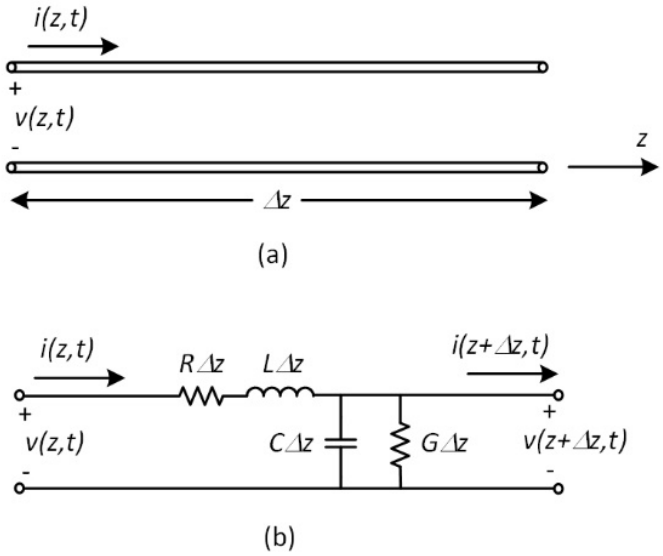

Fig. 2. Transmission line segment (a) with lumped element model (b)

The following analysis is taken from [18]. Basic circuit principles can be utilized to analysis the circuit in Fig. 2 (b). Applying Kirchoff's voltage law results in,

$$v(z,t) - R\Delta z i(z,t) - L\Delta z \frac{\partial i(z,t)}{\partial t} - v(z+\Delta z,t) = 0 \tag{2.4}$$

and applying Kirchoff's current law gives,

$$i(z,t) - G\Delta z v(z+\Delta z,t) - C\Delta z \frac{\partial v(z+\Delta z,t)}{\partial t} - i(z+\Delta z,t) = 0. \tag{2.5}$$

Dividing (2.4) and (2.5) by Δz, taking the limit as $\Delta z \to 0$, and using the phasor form under steady-state conditions results in the transmission line, or telegrapher, equations (2.6) and (2.7).

$$\frac{dV(z)}{dz} = -(R + j\omega L) I(z) \tag{2.6}$$

$$\frac{dI(z)}{dz} = -(G + j\omega C)V(z) \tag{2.7}$$

The parameter ω defines the angular frequency. Solving (2.6) and (2.7) simultaneously by differentiating and substitution yields,

$$\frac{d^2V(z)}{dz^2} - \gamma^2 V(z) = 0 \tag{2.8}$$

$$\frac{d^2I(z)}{dz^2} - \gamma^2 I(z) = 0 \tag{2.9}$$

where,

$$\gamma = \alpha + j\beta = \sqrt{(R + j\omega L)(G + j\omega C)} \tag{2.10}$$

is the complex propagation constant defined by the attenuation constant α (Nepers/m) and propagation constant β (radians/m). The solutions to (2.8) and (2.9) have solutions of the form

$$V(z) = V_0^+ e^{-\gamma z} + V_0^- e^{\gamma z} \tag{2.11}$$

$$I(z) = I_0^+ e^{-\gamma z} + I_0^- e^{\gamma z} \tag{2.12}$$

where the $e^{-\gamma z}$ and $e^{\gamma z}$ terms represent a wave traveling in the positive or negative *z*-direction, respectively. Alternatively *I*(z) can be found by applying (2.8) to the voltage of (2.11) to give

$$I(z) = \frac{\gamma}{R + j\omega L}\left[V_0^+ e^{-\gamma z} - V_0^- e^{\gamma z}\right]. \tag{2.13}$$

The transmission line characteristic impedance can then be found from (2.14).

$$Z_0 = \frac{V(z)}{I(z)} = \frac{R + j\omega L}{\gamma} = \sqrt{\frac{R + j\omega L}{G + j\omega C}} \tag{2.14}$$

For a lossless transmission line $\alpha = 0$ and the propagation constant and characteristic impedance are given in (2.15) and (2.16).

$$\beta = \omega\sqrt{LC} \tag{2.15}$$

$$Z_0 = \sqrt{\frac{L}{C}} \tag{2.16}$$

In this work, the input impedance Z_{in} from a lossless transmission line is of interest. Fig. 3 depicts a lossless transmission line terminated by the load impedance Z_L. The reflection coefficient at the load Γ_L can be computed from (2.17).

$$\Gamma_L = \frac{Z_L - Z_0}{Z_L + Z_0} \tag{2.17}$$

The input impedance Z_{in} a distance l away from the load is found from dividing the voltage by the current at that point along the line (2.18).

$$Z_{in} = \frac{V(-l)}{I(-l)} = \frac{V_0^+\left[e^{j\beta l} + \Gamma_L e^{-j\beta l}\right]}{V_0^+\left[e^{j\beta l} - \Gamma_L e^{-j\beta l}\right]} Z_0 = \frac{1 + \Gamma_L e^{-2j\beta l}}{1 - \Gamma_L e^{-2j\beta l}} Z_0 \tag{2.18}$$

A more suitable from for (2.18) may be obtained by substituting (2.17) in (2.18) to yield

$$Z_{in} = Z_0 \frac{Z_L + jZ_0 \tan\beta 1}{Z_0 + jZ_L \tan\beta l} \tag{2.19}$$

2.3 Microstrip Lines

Microstrip lines are amongst the most popular planar transmission lines due to ease of fabrication and integration with passive and active microwave devices [18]. Fig. 4 (a)

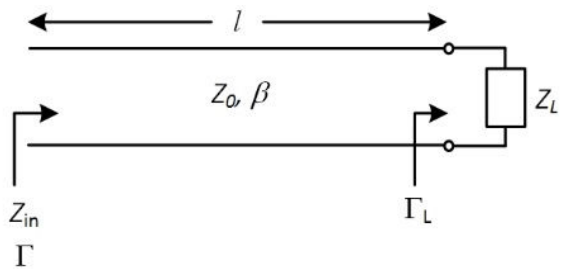

Fig. 3. Transmission line terminated with impedance Z_L

shows a microstrip line of width w printed on a substrate of thickness h and dielectric constant ε_r and the electric field distribution is shown in Fig. 4 (b). The substrate bottom layer ($y = 0$) is completely grounded. If the substrate were air then a simple two-wire transmission line is formed, since the ground plane can be removed from image theory, supporting a pure TEM mode. However, the dielectric substrate ($\varepsilon_r > 1$) presence complicates the structure's analysis since some of the propagating fields exist in the air region above the substrate ($y > h$). The phase velocity in the substrate ($0 < y < h$) produces a slower traveling wave than the portion of the wave traveling above the substrate since $\varepsilon_r > 1$. Thus, a phase match condition for pure TEM waves above and below $y = h$ is impossible to attain. For this reason, the microstrip line supports a quasi-TEM propagating wave. Good approximations from the phase velocity, propagation constant, and characteristic impedance can be obtain from curve-fit solutions found from rigorous quasi-static solutions.

An effective microstrip line dielectric constant can be defined as the dielectric constant of a homogenous medium replacing the substrate and air surroundings (Fig. 5).

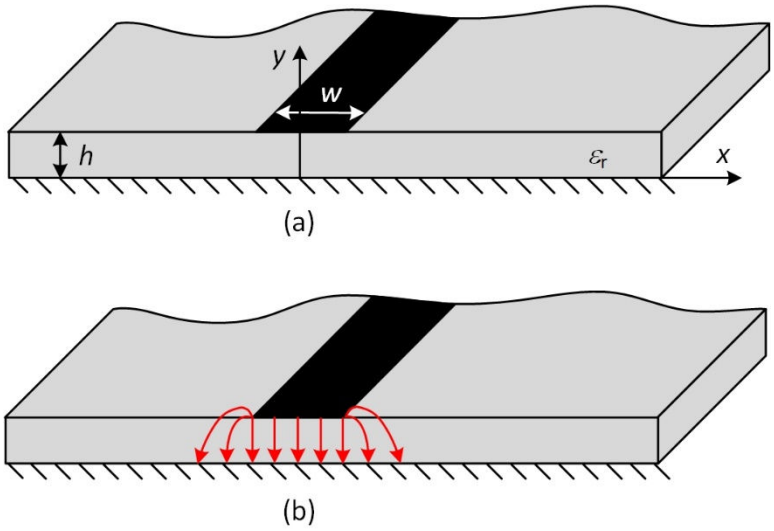

Fig. 4. Microstrip line (a) with electric field distribution for the quasi-TEM propagating model (b)

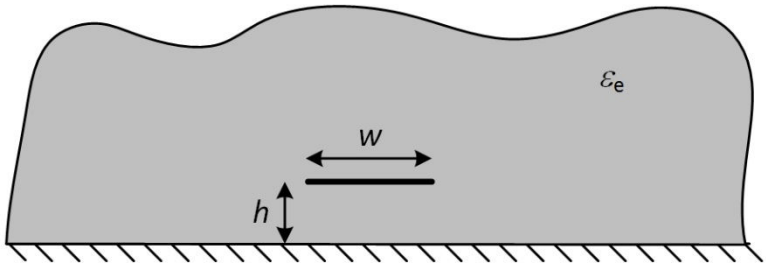

Fig. 5. Effective dielectric constant model with the superstrate and air replaced by a homogenous medium

This effective dielectric constant ε_e can be approximated from (2.20).

$$\varepsilon_e = \frac{\varepsilon_r + 1}{2} + \frac{\varepsilon_r - 1}{2} \frac{1}{\sqrt{1 + 12\,h/w}} \tag{2.20}$$

The microstrip line propagation constant β can be computed from,

$$\beta = k_0 \sqrt{\varepsilon_e} \tag{2.21}$$

where $k_0 = 2\pi/\lambda_0$ is the freespace wavenumber and λ_0 is the freespace wavelength. The microstrip line characteristic impedance Z_0 can be approximated with known dimensions using (2.22).

$$Z_0 = \begin{cases} \dfrac{60}{\sqrt{\varepsilon_e}} \ln\left(\dfrac{8h}{w} + \dfrac{w}{4h}\right) & \text{for } w/h \le 1 \\ \dfrac{120\pi}{\sqrt{\varepsilon_e}\left[w/h + 1.393 + 0.667\ln\left(w/h + 1.444\right)\right]} & \text{for } w/h > 1 \end{cases} \tag{2.22}$$

For a desired characteristic impedance Z_0 with known dielectric constant ε_r, the w/h ratio can be estimated using (2.23).

$$\frac{w}{h} = \begin{cases} \dfrac{8e^A}{e^{2A} - 2} & \text{for } w/h < 2 \\ \dfrac{2}{\pi}\left[B - 1 - \ln\left(2B - 1\right) + \dfrac{\varepsilon_r - 1}{2\varepsilon_r}\left\{\ln\left(B - 1\right) + 0.39 - \dfrac{0.61}{\varepsilon_r}\right\}\right] & \text{for } w/h > 2 \end{cases}$$

$$A = \frac{Z_0}{60}\sqrt{\frac{\varepsilon_r + 1}{2}} + \frac{\varepsilon_r - 1}{\varepsilon_r + 1}\left(0.23 + \frac{0.11}{\varepsilon_r}\right) \tag{2.23}$$

$$B = \frac{377\pi}{2Z_0\sqrt{\varepsilon_r}}$$

Fig. 6 shows the general form for a microstrip-type structure which can be applied to open microstrip lines (as in Fig. 4), inverted microstrip lines, suspended microstrip lines, shield microstrip lines, and microstrip lines on a multiple layer stack-up. A quasi-static approach taken in [19] calculates the transmission characteristics form two capacitances. The first capacitance C_a is computed by removing all dielectric materials and replacing them with air. The second capacitance C has the dielectric materials present in the calculation.

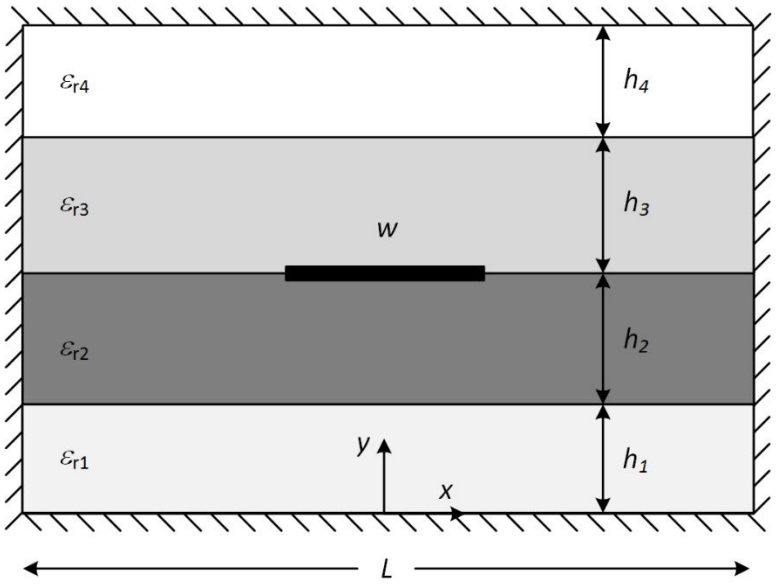

Fig. 6. Microstrip-type transmission line analysis

From these capacitances the characteristic impedance, effective dielectric constant and propagation constant can be computed from

$$Z_0 = \frac{1}{c\sqrt{CC_a}} \tag{2.24}$$

$$\varepsilon_e = \left(\frac{\lambda_0}{\lambda_g}\right)^2 = \frac{C}{C_a} \tag{2.25}$$

$$\beta = k_0\left(\frac{C}{C_a}\right)^{1/2} = k_0\sqrt{\varepsilon_e} \tag{2.26}$$

where c is the speed of light in a vacuum, λ_0 is the freespace wavelength, λ_g is the guide wavelength, and $k_0 = 2\pi/\lambda_0$ is the freespace wavenumber. Using the approach taken in [19], the capacitance C can be computed from

$$C = \frac{\left(1+\frac{A}{4}\right)^2}{\sum_{n\ \text{odd}} \frac{T_n P_n}{Y}} \tag{2.27}$$

where,

$$T_n = \left(L_n + AM_n\right)^2 \tag{2.28}$$

$$L_n = \sin\left(\frac{\beta_n w}{2}\right) \tag{2.29}$$

$$\beta_n = \frac{n\pi}{L} \tag{2.30}$$

$$P_n = \left(\frac{2}{n\pi}\right)\left(\frac{2}{\beta_n w}\right)^2 \tag{2.31}$$

$$\begin{aligned} M_n = \left(\frac{2}{\beta_n w}\right)^3 \Bigg\{ & 3\left[\left(\frac{\beta_n w}{2}\right)^2 - 2\right]\cos\left(\frac{\beta_n w}{2}\right) \\ & + \left(\frac{\beta_n w}{2}\right)\left[\left(\frac{\beta_n w}{2}\right)^2 - 6\right]\sin\left(\frac{\beta_n w}{2}\right) + 6 \Bigg\} \end{aligned} \tag{2.32}$$

$$A = -\frac{\sum_{n\ \text{odd}} \frac{\left(L_n - 4M_n\right) L_n P_n}{Y}}{\sum_{n\ \text{odd}} \frac{\left(L_n - 4M_n\right) M_n P_n}{Y}}. \tag{2.33}$$

The admittance Y in (2.27) can be computed using the transverse resonance technique,

$$Y = Y_2 + Y_3 \tag{2.34}$$

where

$$Y_2 = \varepsilon_{r2}\varepsilon_0 \frac{Y_1 + \varepsilon_{r2}\varepsilon_0 \tanh\left(\beta_n h_2\right)}{\varepsilon_{r2}\varepsilon_0 + Y_1 \tanh\left(\beta_n h_2\right)} \tag{2.35}$$

$$Y_3 = \varepsilon_{r3}\varepsilon_0 \frac{Y_4 + \varepsilon_{r3}\varepsilon_0 \tanh\left(\beta_n h_3\right)}{\varepsilon_{r3}\varepsilon_0 + Y_4 \tanh\left(\beta_n h_3\right)} \tag{2.36}$$

and

$$Y_1 = \varepsilon_{r1}\varepsilon_0 \coth\left(\beta_n h_1\right) \tag{2.37}$$

$$Y_4 = \varepsilon_{r4}\varepsilon_0 \coth\left(\beta_n h_4\right). \tag{2.38}$$

The capacitance C_a is computed using (2.27) with $\varepsilon_{r1} = \varepsilon_{r2} = \varepsilon_{r3} = \varepsilon_{r4} = 1$.

2.4 Microstrip Patch Antennas

Microstrip (MS) antennas consist of a thin metallic strip (known as the patch) on top of a conductive ground plane. Between the patch and ground plane is a dielectric substrate with dielectric constant ε_r and relative permeability μ_r (typically $\mu_r = 1$). These antennas are low profile, conformable to planar and nonplanar surfaces, inexpensive, and easy to manufacture due to their simplicity making them perfect candidates for high-performance aircrafts, space-based applications, and telecommunication devices [20]. Fig. 7 shows a basic MS rectangular patch antenna.

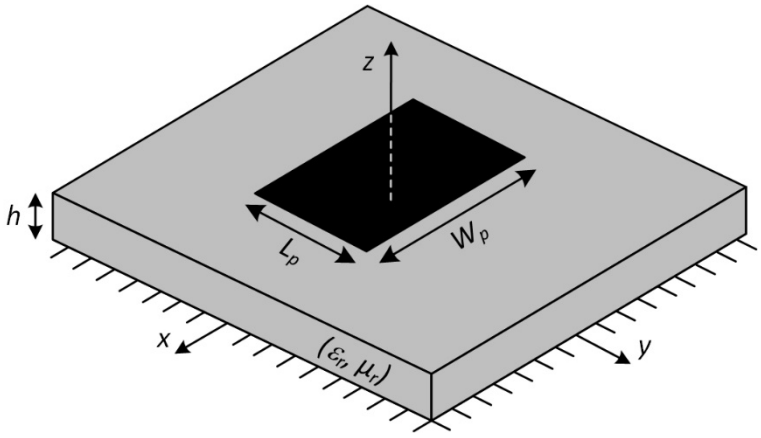

Fig. 7. Rectangular microstrip patch antenna topology

The length of patch (L_p), width of patch (W_p), ε_r and substrate height (h) determine the radiation properties such as the resonant frequency and bandwidth. As a resonant structure, the patch antenna has a narrow bandwidth (typically 1 – 3 % fractional bandwidth). The radiation pattern for this antenna is directed broadside, normal to the plane containing the antenna (positive z-axis in Fig. 7), however, end-fire patterns can be produced by exciting different modal configurations in the patch (not accomplished in this work). The surface current density orients linearly along the patch length axis (y-axis) producing y-directed linear polarization. Patch antenna feeding mechanisms include MS lines, coaxial probes, aperture-coupling, and proximity-coupled feeds.

Fig. 8 depicts a side view profile of a coaxial feed patch antenna and the fundamental TM_{010} mode electric field distribution (shown in red). The coaxial probe is located a distance y_0 from the patch's edge along the length dimension. The field distributes uniformly along the x-axis and can be seen to be roughly a half-wave (at the effective wavelength λ_{eff} under the patch) along the patch. Fringing fields occur at the edges due to the abrupt discontinuity at the patch's edge and dielectric-air boundary. As the fringing fields drift further from the patch (positive z-direction), the fields combine and become radiating fields.

Fig. 9 depicts the classic transmission line model for a rectangular microstrip patch antenna. The antenna's two radiating slots (where the fringing and radiating fields occur in Fig. 8) are modeled as a parallel resonator with equivalent admittances of conductance G and susceptance B (subscripts 1 and 2 describe which radiating slot these belong to).

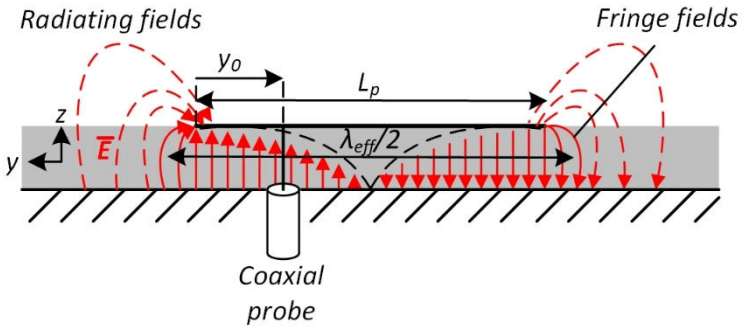

Fig. 8. Electric field distribution of TM_{010} operating mode for a rectangular microstrip patch antenna

The conductance G models the power lost to radiation and susceptance B models the electric fields at the patch's edge. These radiating slots are separated by a transmission line of length L_p with characteristic impedance Z_0 and propagating constant β (functions of W_p and h).

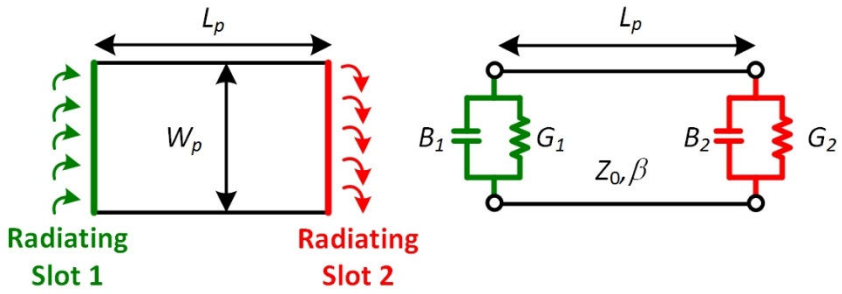

Fig. 9. Transmission line model for a rectangular microstrip patch antenna

The values of B_1 and G_1 can be approximated from the solutions for the equivalent admittance of a finite width slot opening into freespace. The susceptance B_1 and

conductance G_1 can be found from (2.39) and (2.40), respectively, in [20] using this approximation.

$$B_1 = \frac{W_p}{120\lambda_0}\left[1 - 0.636\ln\left(k_0 h\right)\right] \qquad \frac{h}{\lambda_0} < \frac{1}{10} \tag{2.39}$$

$$G_1 = \frac{W}{120\lambda_0}\left[1 - \frac{1}{24}\left(k_0 h\right)^2\right] \tag{2.40}$$

The slot conductance can also be obtained from the field expressions derived by the cavity model in (2.41) [20].

$$G_1 = \frac{-2 + \cos\left(k_0 W_p\right) + k_0 W_p S_i\left(k_0 W_p\right) + \operatorname{sinc}\left(k_0 W_p\right)}{120\pi^2} \tag{2.41}$$

These approximations for (2.40) and (2.41) are similar for certain patch geometries. In this work, these two approximation are averaged to achieve the best estimation in radiation conductance. Since the two slots are identical in a rectangular patch antenna, $B_2 = B_1$ and $G_2 = G_1$.

The design of a patch antenna begins by specifying the substrate parameters h and ε_r and the desired resonant frequency f_0. For the antenna to effectively radiate, the W_p is given by (2.42) from [20].

$$W_p = \frac{c}{2f_0}\sqrt{\frac{2}{\varepsilon_r + 1}} \tag{2.42}$$

The fringing fields at the patch's edge effectively lengthens the patch antenna by $2\Delta L$ (a length ΔL on either side of the patch along the length dimension). The length extension can be approximated from (2.43) in [20] where ε_e is computed from (2.20).

$$\frac{\Delta L}{h} = 0.412 \frac{\left(\varepsilon_e + 0.3\right)\left(\frac{W_p}{h} + 0.264\right)}{\left(\varepsilon_e - 0.258\right)\left(\frac{W_p}{h} + 0.8\right)} \tag{2.43}$$

The patch antenna length can then be approximated from (2.44) [20].

$$L_p = \frac{c}{2 f_0 \sqrt{\varepsilon_e}} - 2\Delta L \tag{2.44}$$

The feed location (for microstrip of coaxial feed structures) along the patch antenna determines the input impedance $Z_{a,in} = R_{a,in} + jX_{a,in}$. At resonance the input impedance becomes real valued ($X_{a,in} = 0$). An equation relating the input resistance to y_0 is (2.45) [20], and Fig. 10 shows a normalized plot of (2.45). The mutual conductance between the two radiating slots G_{12} in (2.45) can be computed from (2.46). The (+) sign in (2.45) is used for modes with odd (anti-symmetric) resonant voltage distribution beneath the patch and between the slots while the (-) sign is used for even (symmetric) resonant voltage distribution.

$$R_{a,in}\left(y_0\right) = \frac{1}{2\left(G_1 \pm G_{12}\right)} \cos^2\left(\frac{\pi}{L} y_0\right) = R_{a,in}\left(y_0 = 0\right) \cos^2\left(\frac{\pi}{L} y_0\right) \tag{2.45}$$

$$G_{12} = \frac{1}{120\pi^2} \int_0^{\pi} \left[\frac{\sin\left(\frac{k_0 W_p}{2} \cos\theta\right)}{\cos\theta} \right]^2 J_0\left(k_0 L_p \sin\theta\right) \sin^3\theta \, d\theta \tag{2.46}$$

A patch antenna fed at the edge, where the electric field magnitude is strongest, leads to the highest input resistance ($R_{a,in}(y_0 = 0)$), since $R_{a,in} \propto |\mathbf{E}|/|\mathbf{H}|$. Typically the value of $R_{a,in}(y_0 = 0)$ ranges from 150 – 300 Ω. When the feed location moves towards the center,

the input resistance shorts ($R_{a,in} = 0$) since zero electric fields exist near the patch's center for the TM_{010} mode. Thus, a y_0 value exists along the patch to provide an input impedance of $Z_{a,in} = 50\ \Omega$ (at the resonant frequency) for a proper impedance match to a 50 Ω system and maximum power transfer to the antenna.

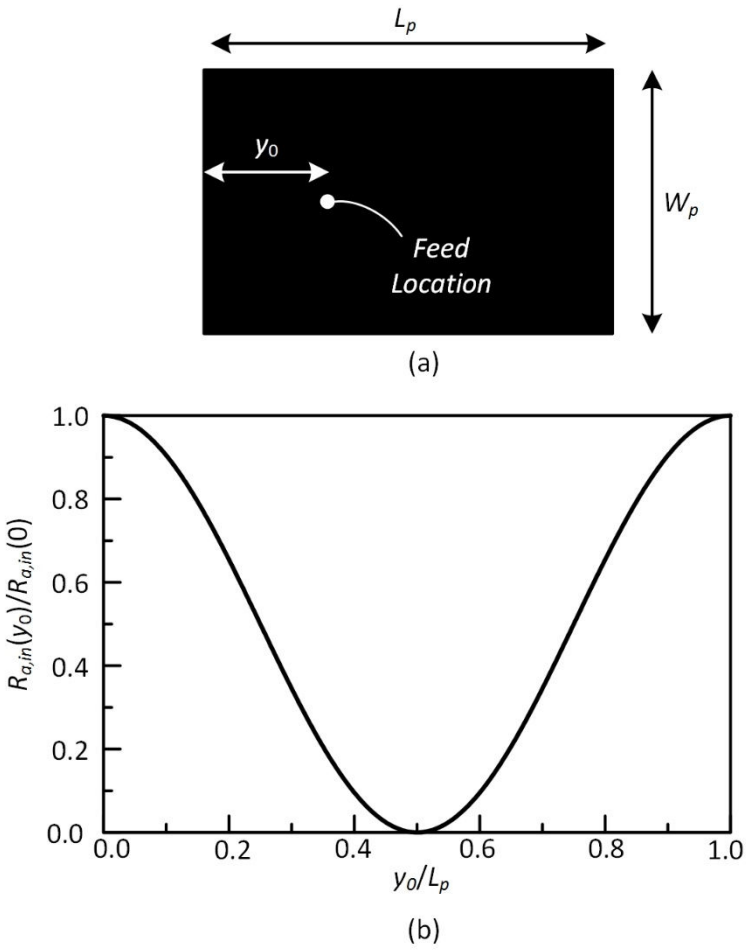

Fig. 10. Coaxial feed for a microstrip patch antenna (a) and normalized input resistance as a function of the coaxial probe position along the patch length (b)

Equations (2.45) and (2.46) can be used to find an approximation for y_0, or a good first-order approximation can be taken as $y_0 = L_p/3$. Since many approximations have been made in the patch antenna analysis, tuning with a full-wave simulator becomes necessary.

2.5 Diodes

This work utilizes RF PIN diodes and varactors as reconfiguration mechanisms in an antenna design. An external bias voltage applied to these solid-state devices alters the non-linear I-V behavior which can be advantages in adaptable performance applications. These devices operate on simple principles from the PN junction shown in Fig. 11. A semiconductor doped with negatively charge atoms creates an excess amount of holes (positively charged carriers) in the material, thus denoting this a P-type (positive-type) semiconductor. Similarly, a semiconductor doped with positively charge atoms creates an excess amount of electrons (negatively charged carriers) in the material, thus denoting this an N-type (negative-type) semiconductor. When these P-type and N-type semiconductors are merged to create a PN junction, diffusion of holes and electrons creates a space charge (depletion) region (with no charge carriers) near the junction as the electrons and holes combine and cancel any excessive charge. The lack of charge carries in this region causes an electric field across the junction to form from the positive and negative atoms doped in the semiconductors. Thus, a potential barrier across the junction pushes holes in the P-

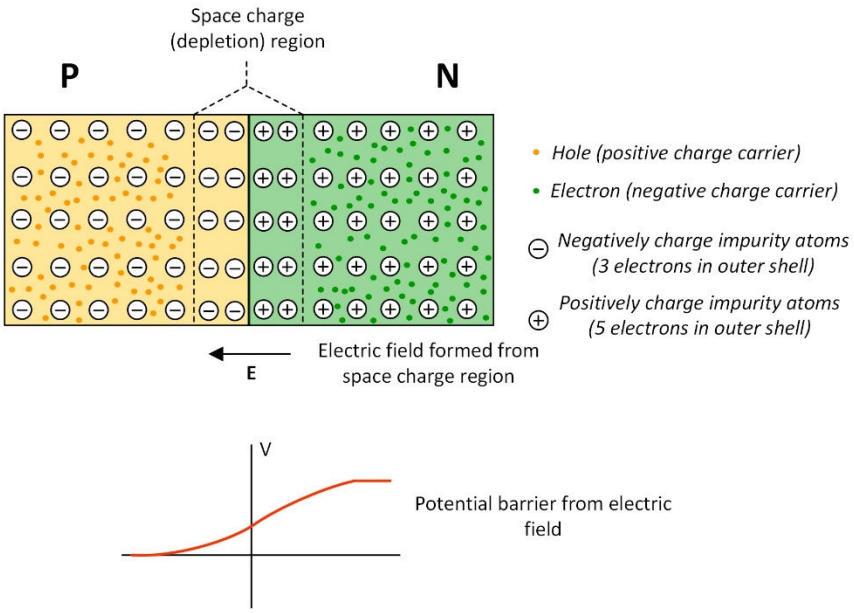

Fig. 11. A PN junction created by combining two semiconductors doped with positively and negatively charge impurities.

type semiconductor and electrons in the N-type semiconductor away from the junction and hinders current flow.

Fig. 12 shows the effects of an external voltage applied to the PN junction ends. Under a forward bias condition, a positive potential applied to the P-type semiconductor terminal repels holes toward the junction. Similarly, the negative potential applied to the N-type semiconductor terminal repels electrons towards the junction. As holes and electrons are forced towards the junction, the space charge region width decreases and lowers the potential barrier allowing holes and electrons to drift across the junction. Under these condition, current will flow from the P- to N-type semiconductor. The opposite effect occurs with a negative bias applied to the PN junction. The negative potential at the P-type terminal attracts holes and the positive potential at the N-type terminal attracts

electrons away from the junction to increase the space charge region width. This increases the potential barrier further reducing the drifting of holes and electrons across the junction and limits any current flow.

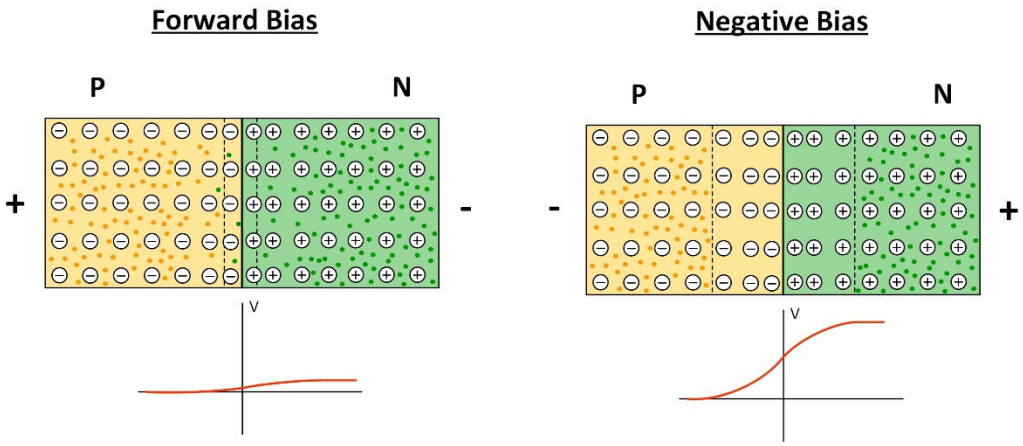

Fig. 12. A PN junction under forward and negative bias from an external voltage.

Fig. 13 summarizes the PN junction I-V characteristics. A negative external voltage applied to the junction results in no current and a positive external voltage results in current flow.

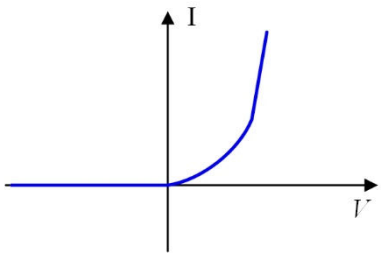

Fig. 13. PN junction IV characteristic.

Based on the characteristics shown, PN junctions can be used as diode switches (Fig. 14) for DC or low frequency and small signal RF applications where under forward bias the switch is “on” and under reversed bias the switch is “off”. When switched from forward to reversed bias, a common diode switch performance metric is the “reverse recovery time”. This describes the amount of time necessary for the stored charge near the junction under forward bias to deplete upon switching to a negative bias condition turning the diode off.

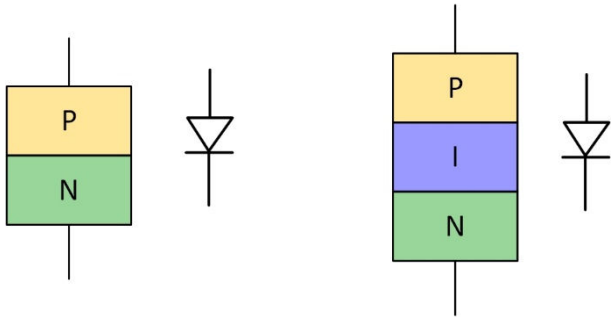

Fig. 14. A PN junction diode (left) and PIN junction diode (right).

For RF applications the RF voltage and current exceed the DC voltage and current applied. The time for the RF signal to complete its negative half cycle voltage may exceed the PN diode switch reverse recovery time causing distortion in the RF signal. Thus, PN diodes are not ideal candidates for RF applications. A PIN junction diode (or PIN diode and shown in Fig. 14) created by placing an un-doped semiconductor layer (known as an intrinsic layer) between the P- and N-type semiconductors resolves this issue at RF frequencies. The intrinsic layer stores charge and largely increases the amount of charge carriers between the P- and N-type regions under forward bias conditions. This increases

the reverse recovery time allowing RF signals to pass with relatively low applied DC bias currents.

Varactor (variable capacitor) diodes take advantage of the PN junction space charge region width under reverse bias conditions. The region's width and thus the capacitance across the junction, can be controlled by the reverse bias voltage magnitude. Since no DC current flows across the junction, varactor diodes are controlled electrostatically (no power) to achieve variable RF characteristics.

CHAPTER III

POLARIZATION RECONFIGURABLE CROSSED MICROSTRIP ANTENNA*

This chapter demonstrates a polarization reconfigurable microstrip patch antenna (PRA) composed of two orthogonally-crossed and co-located narrow microstrip patches with gap discontinuities separating a central probe-fed section from the radiating slots. A pressure driven surface-integrated fluidic network (SIFN) on the antenna surface displaces periodically positioned immiscible fluids with repeating high-low dielectric constants which capacitively load the gap discontinuities and excite the patches independently to create switchable linear polarization. A second design iteration of this antenna with RF PIN diodes connected across the gap discontinuities allows for a benchmark and comparison to this novel fluidic approach. The RF PIN diodes switch between the two independent microstrip patches exciting identical polarization states as in the counterpart fluidic design. Circuit models are developed to explain the impacts on antenna performance for different fluids and diodes utilized in the designs. As a proof-of-concept, room temperature deionized (DI) water and off-the-shelf RF PIN diodes [21] are examined as both are low-cost and readily available. Simulated and measured results from the two prototype antennas are compared with the circuit model for validation. The tuning

mechanisms are compared based on the influence to electrical size, radiation, efficiency, and switching speed. Furthermore, the expected performance improvement from using better fluids and RF PIN diodes are observed from the circuit models and simulation.

The base PRA geometry is shown first. Next, the SIFN PRA is presented with a detailed circuit model. The effects of different fluids on antenna performance are discussed along with simulated and measured impedance and radiation results. A similar treatment of the PRA iteration with RF PIN diodes follows and a comparison between the two approaches, with aid from the circuit models, concludes the paper.

3.1 Antenna Geometry

The base PRA geometry in Fig. 15 shows two orthogonally-crossed co-located narrow microstrip patches of width W. They are electrically isolated at their overlap by four outward-directed microstrip gap discontinuities of width g. The SMA probe feed centered in the overlapping square section excites the antenna, but the capacitive gap widths permit little coupling to the arms without a reconfiguration mechanism present. The length L_3 sets the distance from the probe feed to the gap edge. The antenna arms 1 and 3 are defined by length L_1 and arms 2 and 4 by length L_2.

Operationally, increasing the coupling or switching-on an electrical connection between arms 1 and 2 or arms 3 and 4 and the central feed section excites the narrow microstrip patch along the x- and y-directions, respectively. These two linearly-polarized configurations are referred to as the *X-pol* and *Y-pol* states (each having orthogonal radiation properties). This work also assumes that the individual patches are impedance-matched to Z_0 at a frequency f_0 through the equivalent probe feed location on each arm. A

combined *XY-pol* will therefore result in a poorly matched parallel impedance of $0.5Z_0$ at f_0 and is not considered.

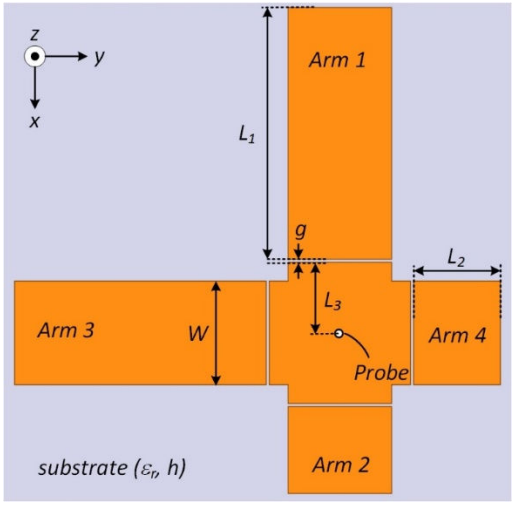

Fig. 15. Basic PRA geometry formed by co-locating two narrow microstrip patches orthogonally on a probe-fed center section. Gap discontinuities separate the feed from radiation slots.

3.2 Fluidic PRA

3.2.1 Concept and Modeling

This novel SIFN tuning mechanism exploits the ability to capacitively load the gaps with dielectric fluids in alternating "high-low" dielectric strengths and a rotational arrangement around the central feed location (illustrated in Fig. 16). This loads the gaps appropriately to independently activate the two antenna states. The fluids have complex dielectric constants $\varepsilon_{r1} = \varepsilon'_{r1}\left(1 - j\tan\delta_{d1}\right)$ and $\varepsilon_{r2} = \varepsilon'_{r2}\left(1 - j\tan\delta_{d2}\right)$, and are housed in a superstrate $\varepsilon_{rs} = \varepsilon'_{rs}\left(1 - j\tan\delta_{ds}\right)$ of dimensions $L_s \times W_s \times H_s$ with integrated fluidic channels of dimensions $W_f \times H_f$ forming the SIFN. This arrangement of fluids is displaced

through the network using a 3D-printed acrylonitrile butadiene styrene (ABS) tubing adapter of dimension $L_a \times L_a \times L_a$ which interfaces external tubing to the rectangular SIFN channels. The superstrate intersects microstrip arms 1 and 3 a distance $p \times L_1$ outwardly from the gap discontinuity, where $0 < p < 1$.

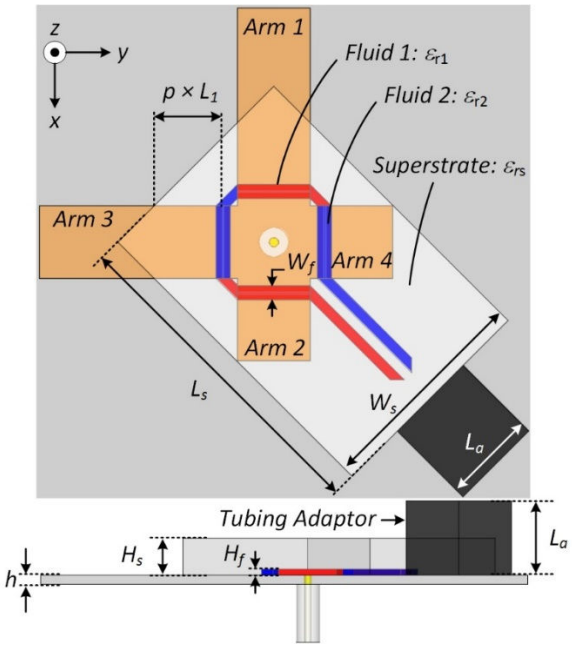

Fig. 16.The addition of a SIFN on the PRA formed from a superstrate with integrated fluidic channels.

Fig. 17 depicts a complete circuit model for the SIFN PRA. The admittance Y_1 denotes the admittance looking from the probe feed locations outward to the radiation slot of arm 2 (and likewise for admittances Y_2, Y_3, and Y_4). The radiation slot parameters G and B are computed using classic transmission-line model techniques of a microstrip patch antenna [20]. The transmission lines sections of arms 1 and 3 (of width W) that are not loaded by the superstrate are denoted T_U. The characteristic admittance Y_c and propagation

constant β of these transmission lines are computed from (2.22) and (2.21), respectively, using classical microstrip line analysis. The transmission lines labeled T_L represent the sections of all arms (of width W) that are loaded by the superstrate. The parameters $Y_{c,L}$ and β_L of all T_L lines are defined by the effective dielectric constant in (2.25), where C and C_a are the electrostatic capacitances computed from the microstrip-type transmission line treatment (Section 2.2). The transmission lines marked T_F are the superstrate-loaded sections near the central feed section (of width $2L_3$). These line parameters are also computed from the microstrip-type transmission line treatment in Section 2.2. A π-network can then be used to model the microstrip gap discontinuity where the admittances are defined by (3.1) and (3.2).

$$Y_p = G_p + j\omega C_p \tag{3.1}$$

$$Y_g = G_g + j\omega C_g \tag{3.2}$$

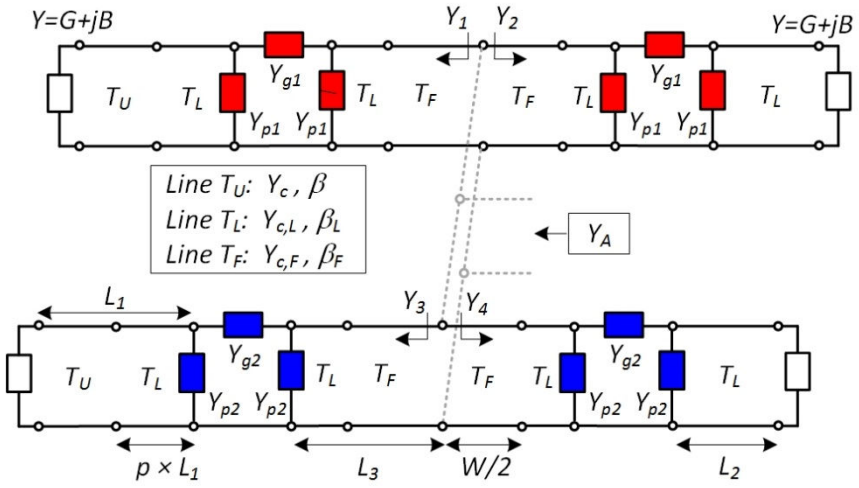

Fig. 17. The SIFN PRA circuit model based on the patch T.L. model with an admittance π-network for the gap discontinuity.

The admittances Y_{g1}, Y_{p1}, Y_{g2}, and Y_{g1} in Fig. 17 signify a gap loaded by ε_{r1} or ε_{r2}, respectively. The conductance G_g and G_p and capacitance C_g and C_p are computed from full-wave simulations [22] of the loaded gap, where the gap edges define the reference planes. This method was chosen as an alternative to analytical gap models [23, 24] to account for complexities generated from the SIFN implementation. The circuit parameters found from the simulated S parameters are

$$\begin{aligned} G_g &= \mathrm{Re}\left[\frac{1}{B}\right], \qquad & C_g &= \mathrm{Im}\left[\frac{1}{B}\right]\frac{1}{\omega}, \\ G_p &= \mathrm{Re}\left[\frac{A-1}{B}\right], \qquad & C_g &= \mathrm{Im}\left[\frac{A-1}{B}\right]\frac{1}{\omega}, \end{aligned} \tag{3.3}$$

where,

$$\begin{aligned} A &= \frac{(1+S_{11})(1-S_{22})+S_{12}S_{21}}{2S_{21}}, \\ B &= Z_0\frac{(1+S_{11})(1+S_{22})-S_{12}S_{21}}{2S_{21}}, \end{aligned} \tag{3.4}$$

with ω and Z_0 defined as the angular frequency and characteristic impedance, respectively. In (3.4), $Z_0 = 1/Y_{c,L}$ since the gap resides along the T_L transmission line sections. This circuit model can be further simplified by noticing in either *X–pol* or *Y–pol* configurations, the active modes will allow only *x*–traveling or *y*–traveling fields underneath the patch. The circuit model transmission lines assume a single directed traveling wave and thus, Y_1 and Y_2 or Y_3 and Y_4 can be ignored in the total antenna input admittance. Ignoring Y_3 and Y_4, the circuit model becomes that shown in Fig. X. This improved circuit model also

includes the probe feed presence effect through a series inductance L_{pr} (computed from the basic equations for the inductance of a wire segment).

The circuit model provides some physical insight on the impact of the materials used in the fluidic reconfiguration mechanism to the antenna's operation. This is accomplished by examining a series of generic dielectric fluids used to load the gap, and computing C_g, C_p, $R_g = 1/G_g$, and $R_p = 1/G_p$ with h = 1.58 mm, W = 10 mm, ε_r = 2.2, and ε_{rs} = 2.66. Fig. 19 and Fig. 20 show the variance of C_g and R_g using nominally low and

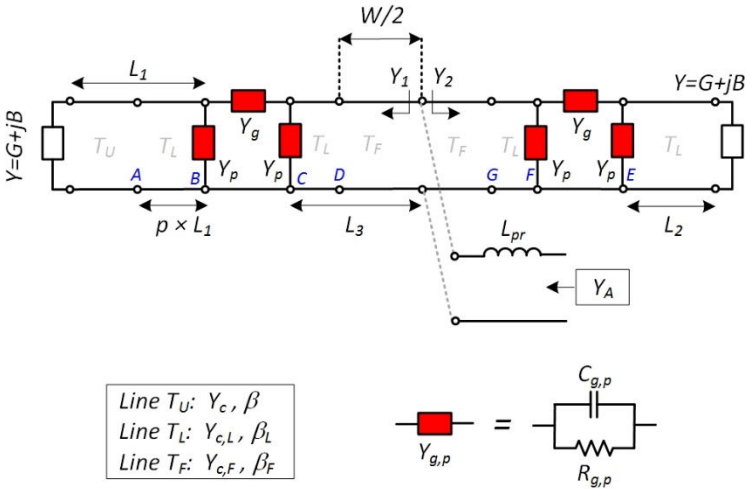

Fig. 18. Improved circuit model for the fluidic PRA with SIFN.

high loss tangent fluids with varying dielectric constants at 2.45 GHz. The fluid dielectric constant strongly impacts the gap coupling capacitance C_g. As the capacitive coupling increases with larger ε'_{r1}, the antenna's operating frequency will shift towards the resonant frequency of a traditional patch (gaps replaced by solid metallization) with similar dimensions, since a short begins to occur across the gap. Utilizing low-loss (or preferably

lossless) fluids largely increases the gap resistance R_g, which signifies the gap admittance Y_g becomes almost strictly imaginary. Thus, the drop in radiation efficiency from ohmic losses stays low for low-loss fluids. High-loss fluids decrease R_g enough to make Y_g a significant component of the antenna impedance as well as decreasing radiation efficiency. The plate resistance R_p and plate capacitance C_p are less affected by the fluid material properties since the substrate properties dominate. Furthermore, the Y_g contribution exceeds that of the plate admittance Y_p towards the overall antenna impedance ($R_p >> R_g$ and $C_p << C_g$).

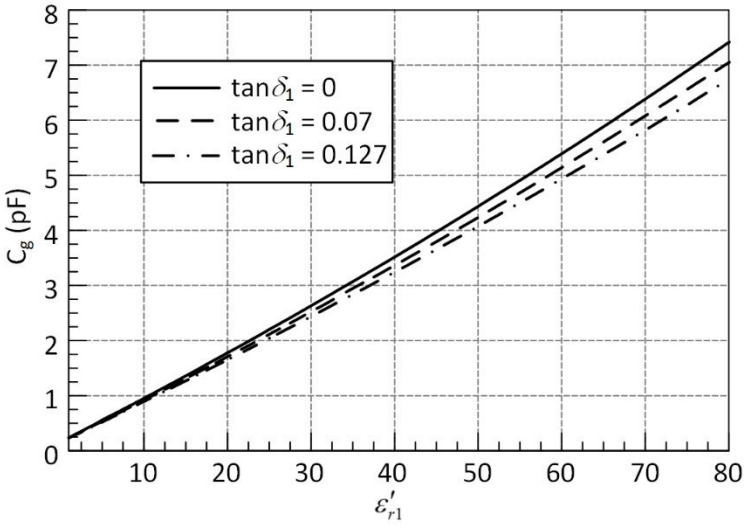

Fig. 19. The gap capacitance C_g for a generic sampling of dielectric fluids loading the gap discontinuity at 2.45 GHz.

3.2.2 Design and Prototype

Readily available DI water $\varepsilon_{r1} = 76.9(1 - j0.127)$ [25] (at room temperature) was used as the high dielectric fluid for a proof-of-concept demonstration. The high dielectric

strength of water sufficiently loads the microstrip gaps to excite the antenna near the resonant frequency of a traditional patch with similar dimensions. In this design, the high

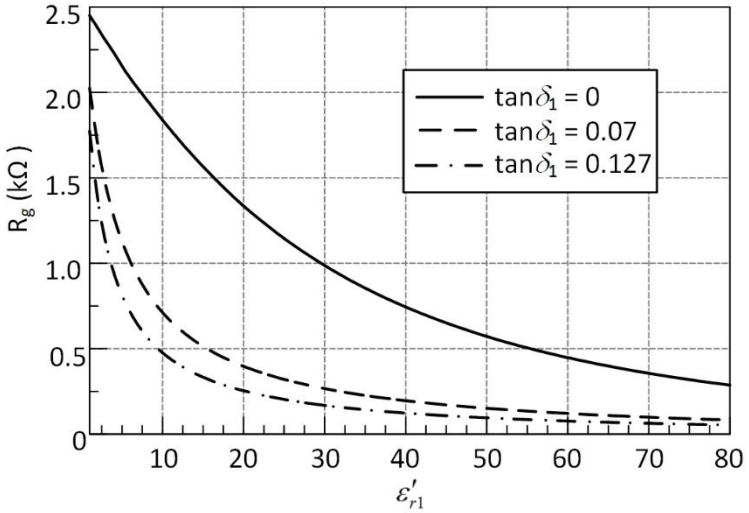

Fig. 20. The gap resistance R_g for a generic sampling dielectric fluids loading the gap discontinuity at 2.45 GHz.

loss tangent of water makes Y_{g1} a significant factor towards the antenna impedance and reduces the antenna efficiency (discussed in Section V). Conversely, air $\varepsilon_{r2} = 1$ ensures the appropriate arms remain electrically isolated from the central feed section.

A SIFN PRA prototype was designed on Duriod 5880 ($\varepsilon_r = 2.2$, $\tan\delta = 0.0009$) for operation in the 2.4 – 2.5 GHz ISM band. The SIFN superstrate was created using polydimethylsiloxane (PDMS) ($\varepsilon'_{rs} \sim 2.66$, $\tan\delta_s \sim 0.04$). The prototype antenna dimensions (in mm) are: $L_1 = 24.44$, $L_2 = 8.44$, $L_s = 45.72$, $W_s = 30.48$, $L_a = 12.85$, $W = 10$, $g = 0.3$, $h = 1.58$, $H_s = 6.35$, $H_f = 1$, $W_f = 2$, where $p = 0.33$. Syringes were used to create the periodic arrangement of fluids shown in Fig. 2, and a peristaltic pump was connected to both ends of the ABS interface creating a closed loop within the SIFN. The

pump operates on a DC voltage away from the PRA radiating surface and applies pressure driven forces to push the two water strips into *X-pol* and *Y-pol* configurations (illustrated in Fig. 21). The antenna can be turned off by pushing air over all microstrip gaps.

The simulated, measured, and analytical reflection coefficient for both antenna states from 2–3 GHz are presented in Fig. 22 and show good correlation. The center frequencies from the *X–pol* state are 2.415, 2.398, and 2.423 GHz from the circuit model, full-wave simulation, and measurement, respectively. For the *Y–pol* state these values are 2.415, 2.398, and 2.434 GHz. The circuit model and simulation center frequencies are in good agreement (better than 0.8%). The fractional bandwidth (FBW) predicted from the circuit model and simulations are 3.2% and 2.82% (both *X–pol* and *Y–pol*), respectively,

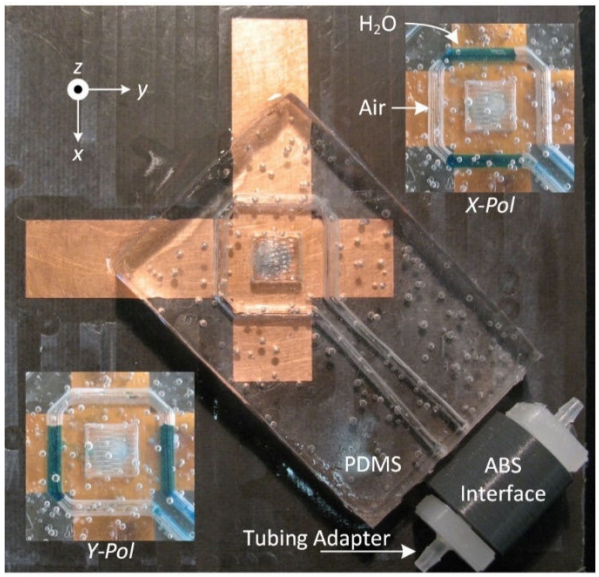

Fig. 21. The prototype SIFN PRA with a PDMS superstrate for the SIFN. The DI water position for *X-pol* and *Y-pol* states are shown.

compared to the measured 2.39% and 2.19% bandwidth for the measured *X–pol* and *Y–pol* states, respectively. The upward shift in the measured center frequency and slightly lower impedance bandwidth can be contributed to fabrication tolerances (manual milling machine limitations and air bubbles trapped in the PDMS superstrate) and uncertainties in the exact dielectric constant of the water caused by impurities at the time of experiment.

As expected, *X–pol* and *Y–pol* states are almost identical due to the design symmetry. The SIFN PRA simulated (at 2.4 GHz) and measured (at 2.42 GHz) normalized radiation patterns shown in Fig. 23 demonstrates switchable linear polarization with low cross polarization can be achieved from the SIFN design. The superstrate asymmetry along the active antenna parasitically tilts the main beam since the wave encounters the PDMS-air boundary, but the basic patch antenna performance is acceptable despite the superstrate presence.

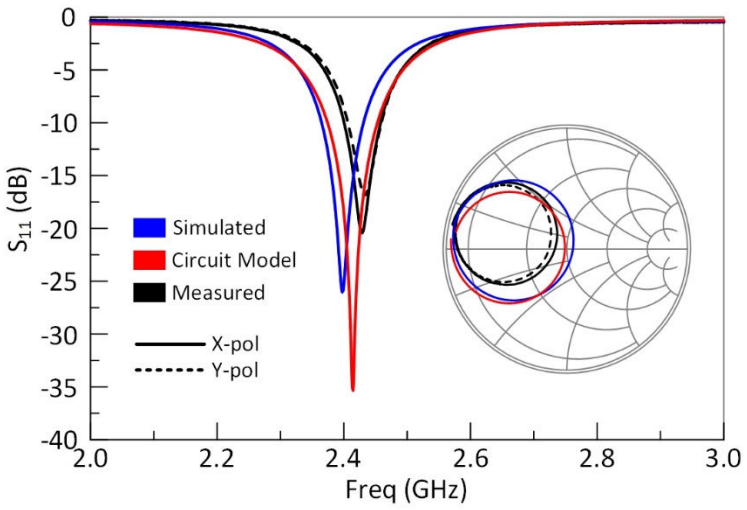

Fig. 22. The fluidic PRA reflection coefficient from the circuit model, simulation, and measurement.

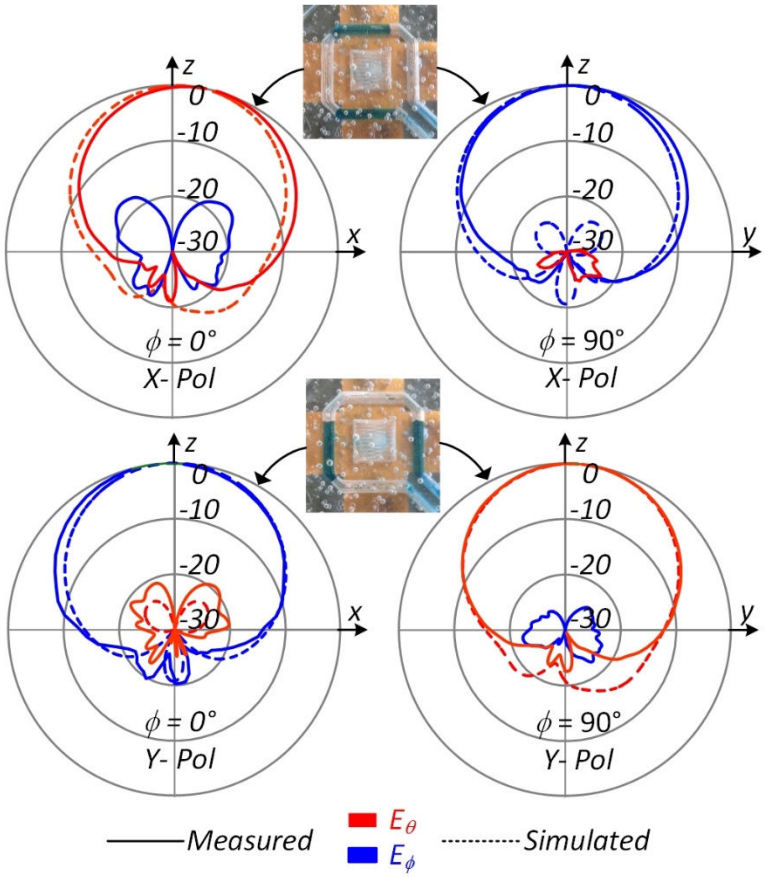

Fig. 23. Normalized radiation patterns for the fluidic PRA at 2.4 GHz (simulation) and 2.42 GHz (measured).

3.3 Solid-state PRA

3.3.1 Concept and Modeling

Next, RF PIN diodes are considered as the solid-state reconfiguration mechanism in comparison to the fluidic approach discussed above. The RF PIN diodes create electrical connections in the antenna instead of capacitively loading the gaps. The diodes are oriented in opposite directions (illustrated in Fig. 24) to electrically connect or disconnect

appropriate arms to the feed section and independently excite the two antenna polarization states. The antenna arms are DC grounded via high impedance RF lines of width W_b and length L_b, acting as quarter-wave RF chokes. Applying a positive bias voltage to the SMA feed, via an external bias tee, forward biases diodes 1, 2, 5, and 6 and negative biases diodes 3, 4, 7, and 8 to activate the *X–pol* state. A negative bias voltage places opposite bias conditions on the diodes to activate the *Y–pol* state. Diodes are strategically placed as close as possible to the non-radiating antenna edges where the highest RF current exists.

Fig. 25 shows the RF PIN diode-enabled PRA circuit model where a similar transmission line treatment provides the base structure. The microstrip arms and center feed section are modeled by transmission line sections with characteristic admittance Y_c and propagation constant β which can be computed from (2.22) and (2.21) using classical microstrip line theory. A π-network of admittances Y_g and Y_p computed from (3.3) models the gap discontinuities. The RF PIN diodes are added to the π-network in the form of a series resistance R_f (typically small) and L under forward bias. The inductance L comes from packaging and shifts the operating frequency below the resonant frequency of a traditional patch with similar dimensions. The resistance R_f also contributes to the overall antenna impedance and impacts radiation efficiency. The values of R_f and L are found in the RF PIN diode datasheet. Note that only the active antenna has been modeled (as in the SIFN PRA improved circuit model discussed above). In addition, the quarter-wave RF choke lines used to DC ground the antenna arms are modeled as a shunt inductor L_b. Full-wave simulations are utilized to compute the value of L_b. Again, the probe feed has been included in the model as the series inductance L_{pr}.

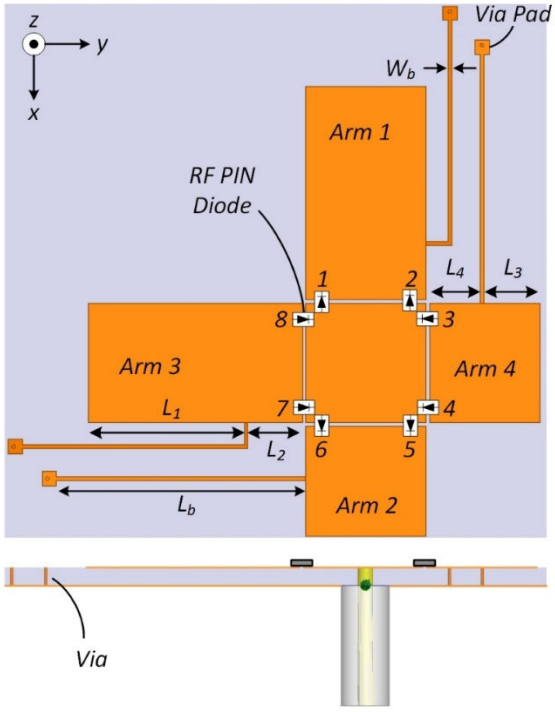

Fig. 24. The RF PIN diode PRA model with eight diodes oriented along the microstrip gap discontinuities.

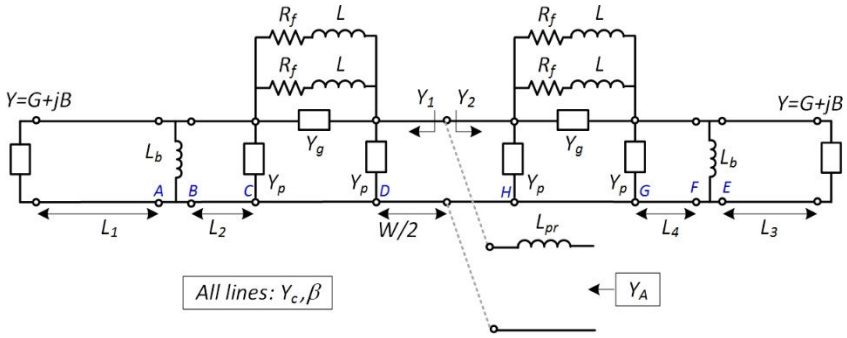

Fig. 25. The RF PIN diode PRA circuit model similar to the SIFN PRA circuit model with additional circuit components for the diodes.

3.3.2 Design and Prototype

Fig. 26 shows the fabricated RF PIN diode PRA prototype. A packaged bias tee applies the bias voltage V_b along with the RF source to the SMA feed. Off-the-shelf RF PIN diodes [21] with R_f = 2–3 Ω and L = 0.7 nH are utilized in this work. The value of R_f varies based on surface mounting effects limiting DC current trough the RF PIN diodes. The antenna was designed to operate in the 2.4 – 2.5 GHz ISM band on Duriod 5880 (ε_r = 2.2, tanδ = 0.0009) with dimensions (in mm) of: L_1 = 13.14, L_2 = 4.68, L_3 = 4.82, L_4 = 4.38, W = 10, g = 0.3, W_b = 0.3, L_b = 20.8, h = 1.58. The positive (*X–pol*) or negative (*Y–pol*) bias voltage should provide approximately 10mA of DC current to active each RF PIN diode. Thus, 40 mA of DC current (4 RF PIN diodes per antenna) are required to operate either *X–pol* or *Y–pol* configurations.

The circuit model, simulated, and measured reflection coefficient data are compared in Fig. 27. The center frequencies and FBW are in excellent agreement. The slight shift in the Smith Chart impedance curve are due to fabrication tolerances (mechanical milling machine limitations, hand placement and soldering of diodes, and resistor tolerances setting the PIN diode's forward resistance). The *X–pol* and *Y–pol* frequency responses are nearly identical due to design symmetry. The simulated and measured normalized radiation patterns at 2.47 GHz presented in Fig. 28 show good agreement and the RF PIN diodes effectiveness for providing switchable linear polarization with low cross polarization levels through a simple biasing scheme.

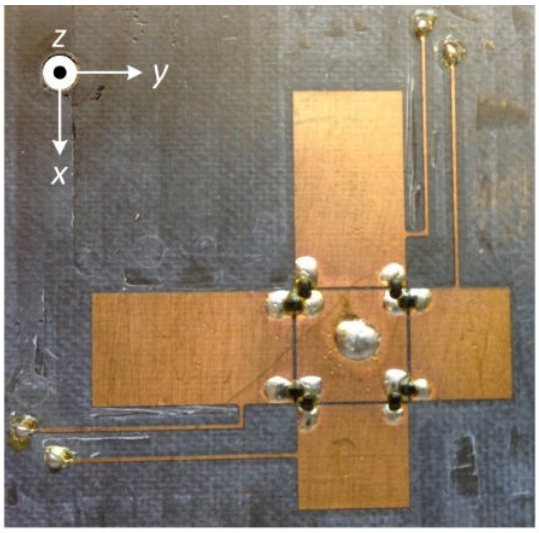

Fig. 26. The RF PIN diodes PRA model prototype. Not shown is the bias tee network feeding the antenna.

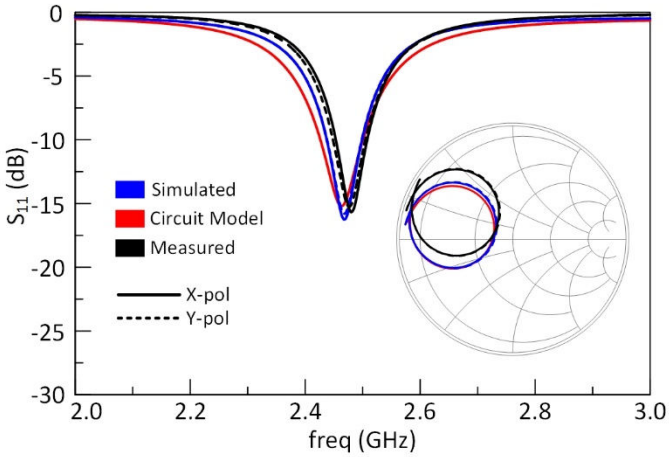

Fig. 27. The SIFN PRA reflection coefficient from the circuit model, simulation, and measurement.

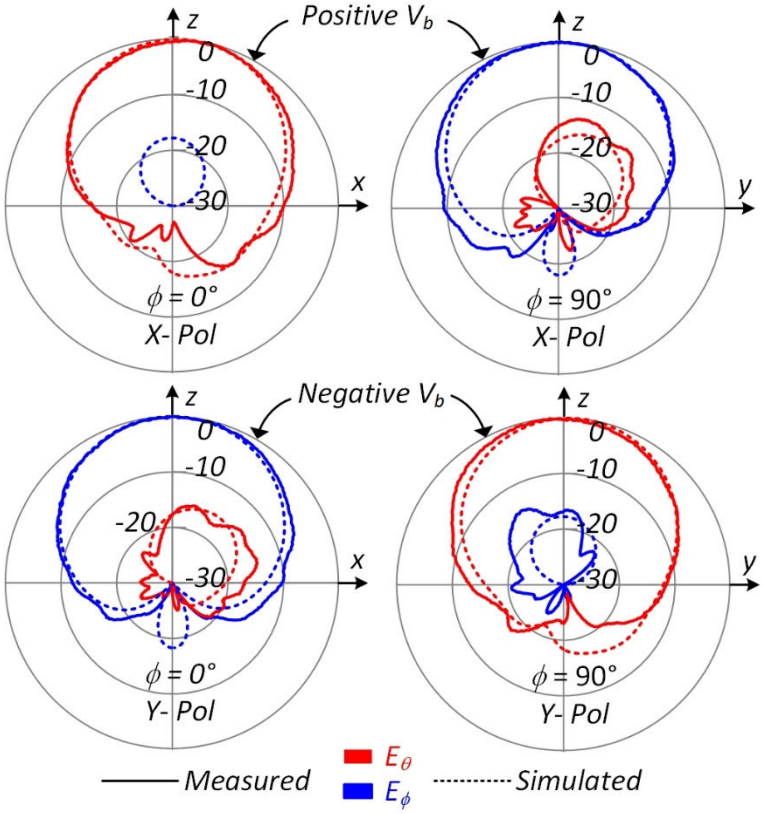

Fig. 28. Simulated vs. measured patterns for the RF PIN diode PRA at 2.47 GHz

3.4 Discussion I

Both fluidic and solid-state reconfiguration mechanism provide good polarization switching performance for the proposed antenna topology. Before exploring subsequent design iterations, a discussion with regard to the impact on antenna performance for the reconfiguration mechanisms discussed above (fluidic vs. solid-state) proceeds. In particular, electrical size, radiation efficiency, radiation patterns and switching speed are examined. This allows us to understand the advantages and disadvantages of each mechanism and aids in developing improvements to the antenna performance.

The antennas electrical size are inspected by considering two traditional patch antennas with the SIFN and RF PIN diodes removed and gap discontinuities replaced with solid metallization (all other dimensions remain the same with the exception of the probe feed location that enables an impedance match). For the SIFN reconfiguration mechanism, capacitive loading from the fluid (C_g) facilitates an electrical lengthening and a higher operating center frequency (f_0 = 2.39 GHz) than a traditional patch antenna with the same dimensions (f_0 = 2.15 GHz). A converse situation occurs for the RF PIN diode who's package inductance L facilitates an electrical shortening and lower operating center frequency (f_0 = 2.42 GHz) than that of a traditional patch antenna (f_0 = 2.68 GHz). This effective lengthening and shortening creates a subtle difference in the physical aperture size (total patch length for solid-state model < total patch length for fluidic model) allowing the overall aperture efficiency for the larger fluidic model to be higher than the smaller solid-state model at the same operating frequency.

A more illuminating comparison of the PRA's radiation efficiency can be observed by considering the ohmic losses present in each reconfiguration technique. The measured gain for the SIFN and RF PIN diodes iterations are 2 dBi and -4.84 dBi respectively. The SIFN and RF PIN diodes iteration simulated radiation efficiencies are 22% and 8%, respectively. Radiation efficiency measurements were not available, but these results are considered as an indication of what the upper bound on measured efficiencies would be since material properties, component tolerances, and other factors will influence the fabricated design. These low gain and efficiency values can be attributed to ohmic loss mechanisms originating from the high loss tangent of water in the SIFN ($R_g \sim 50\ \Omega$) and

the forward resistance ($R_f \sim 3\ \Omega$) in the RF PIN diode. Also, the SIFN model experiences attenuation from the lossy PDMS superstrate forming the fluidic network. The larger value of R_g compared to R_f, along with the PDMS superstrate, creates an assumption that a larger efficiency drop and lower gain would be observed in the fluidic model. However, Fig. 17 shows the admittance Y_g as a parallel load (R_g and C_g) across the gap. Since C_g is large, current is split between the resistive (attenuating) and capacitive (reactive loading) paths, reducing overall attenuation. In Fig. 25, Y_g can be ignored (negligible compared to the impedance from R_f and L) leaving series coupling across the gap of $2R_f$ and $2L$. All current that couples across the gap experiences the combined attenuation from the R_f terms. Thus, the fluidic coupling mechanism is less sensitive to ohmic losses from non-ideal components (dielectric fluids in this case). Moreover, as previously mentioned, the larger electrical size from the SIFN contributes to the higher simulated radiation efficiency and larger measured gain.

Fig. 29 and Fig. 30 show the simulated radiation efficiency as functions of R_f and the water loss tangent ($\tan\delta_{1,2}$) for the RF PIN diode and fluidic PRA models, respectively. In addition, Fig. 30 presents the efficiency with an ideal air superstrate (lossless) compared to the current PDMS superstrate. To achieve 50% radiation efficiency requires an R_f value of less than 0.2 Ω while a fluid with loss tangent as high as 0.02 (with the current PDMS superstrate) achieves the same goal. This loss tangent requirement relaxes to 0.04 with a lossless air superstrate. RF PIN diodes with such low R_f values are difficult to find at the time of publication. However, high dielectric fluids with a loss tangent of less than 0.02 –

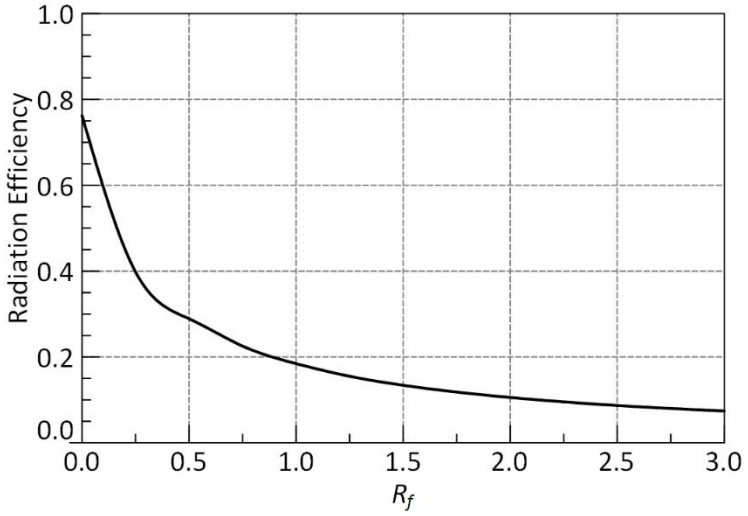

Fig. 29. Radiation efficiency as a function of RF PIN diodes forward resistance.

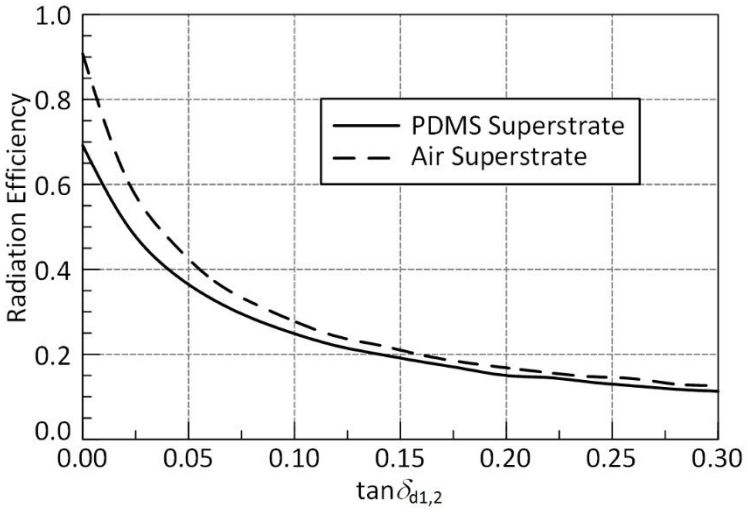

Fig. 30. Radiation efficiency as a function of loss tangent of water with the current PDMS superstrate and lossless air superstrate.

0.04 may be possible with fluids used in [12-15]. With ideal components ($R_f = 0$, $\tan\delta_{1,2} = 0$, and air superstrate), the SIFN PRA achieves better efficiency due to the larger effective aperture.

3.5 Improved Solid-state PRA

3.5.1 Concept and Modeling

The previous discussion revealed key insights on antenna performance from the presence of both fluidic and solid-state reconfiguration mechanisms. Fig. 29 and Fig. 30 shows that the radiation efficiency can be drastically improved by utilizing low-loss (ideally lossless), high-dielectric fluids or very low forward resistance RF PIN diodes. Fluids of such properties are difficult to find at the time of this research and lowering the individual forward resistance of readily available packaged RF PIN diodes proves difficult. An alternative to reducing ohmic losses in the solid-state model would be to reduce the overall series resistance across the gap discontinuities by increasing the number of RF PIN diodes present. Fig. 31 presents the concept of this modification where ten RF PIN diodes have been placed across each gap discontinuity. The circuit model in Fig. 32 shows the changes made from this adaptation. The 10 RF PIN didoes are model by an equivalent admittance Y_{on}, which comprises the parallel combination of the ten didoes, above each gap discontinuity. All other circuit model components from the previous solid-state PRA model remain unchanged and are computed in the same manor.

Increasing the number of RF PIN diodes from two to ten reduces the overall resistance across the gap by 5× and reduces the series inductance seen across the gap (from the diode package) by 5×. Geometrically, this PRA will become electrically larger

compared its two RF PIN diode counterpart from the reduced inductance. Operationally, the PRA will mimic that of the previous solid-state model.

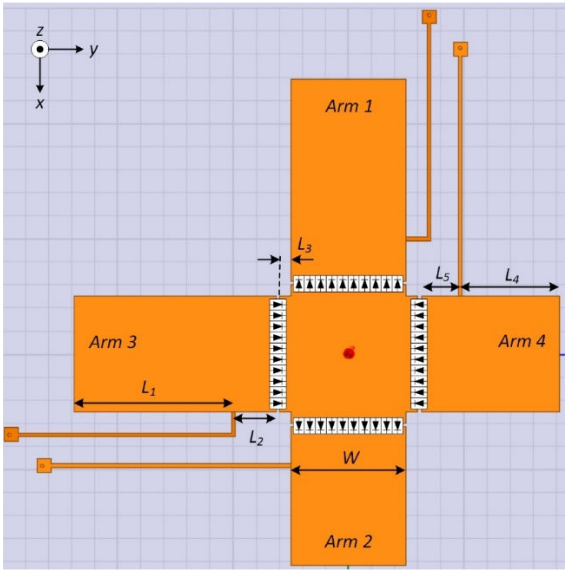

Fig. 31. Improved performance solid-state PRA with 10 RF PIN diodes across each gap discontinuity.

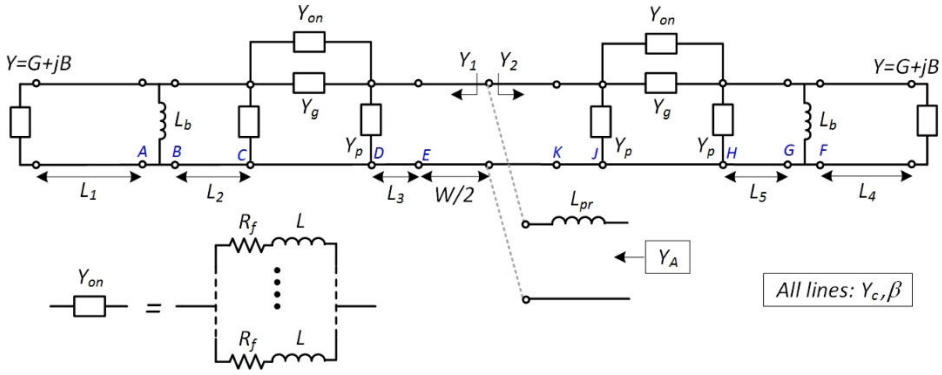

Fig. 32. Circuit model for the improved performance solid-state PRA with 10 RF PIN diodes across each gap.

3.5.2 Design and Prototype

Fig. 33 shows the improved solid-state PRA prototype designed to operate in the same frequency range (2.4 – 2.5 GHz) on the same substrate (Duriod 5880 – ε_r = 2.2, tanδ = 0.0009, h = 1.58 mm) as the previous design iteration. Furthermore, the same readily available, off-the-shelf RF PIN didoes [21] with R_f = 2–3 Ω and L = 0.7 nH are utilized. The dimensions (in mm) of this design are: L_1 = 14.97, L_2 = 3.68, L_3 = 1, L_4 = 7.27, L_5 = 3.38, W = 10, g = 0.3, W_b = 0.3, and L_b = 20.8. A packaged bias tee applies the bias voltage V_b (positive for *X–pol* or negative for *Y–pol* configurations) along with the RF source to central feed section. In order to achieved the desired forward resistance across each RF PIN diode (2 – 3 Ω), a total of 200 mA of DC current (10 mA per diode) must be delivered by the power source to operate either *X–pol* or *Y–pol* configurations. Thus, the power

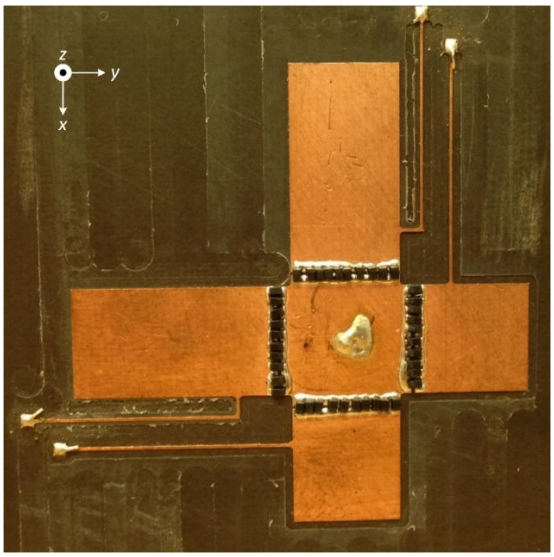

Fig. 33. Prototype for the improved performance solid-state PRA with 10 RF PIN diodes across each gap.

requirements from the control circuits have increased by 5×, revealing a trade-off between the control circuit power requirements and radiation performance.

Fig. 34 shows a comparison between the circuit model, simulated, and measured reflection coefficient data. The center frequencies and FBWs of each model are nearly identical at 2.445 GHz and 1.2%, respectively. The impedance at the center frequency (determining the impedance match strength) slightly differ due to approximations made in computing the circuit model radiation conductance, ideal features in the simulation model, and fabrication tolerances in the prototype.

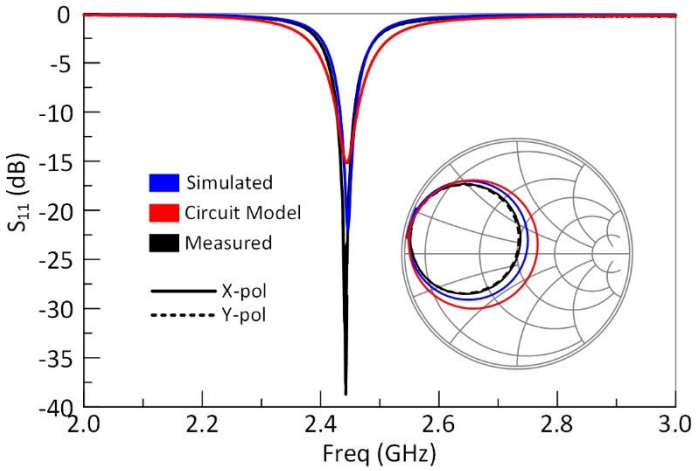

Fig. 34. Reflection coefficient results for the improved solid-state PRA with 10 RF PIN diodes per gap.

Fig. 35 shows the simulated and measured normalized radiation patterns at 2.445 GHz (both simulated and measured curves) for the *X–pol* and *Y–pol* configurations in both principle planes. The RF PIN diodes, again, facilitate linear polarization switching and the simulated and measured patterns are in close agreement. The disagreement in the

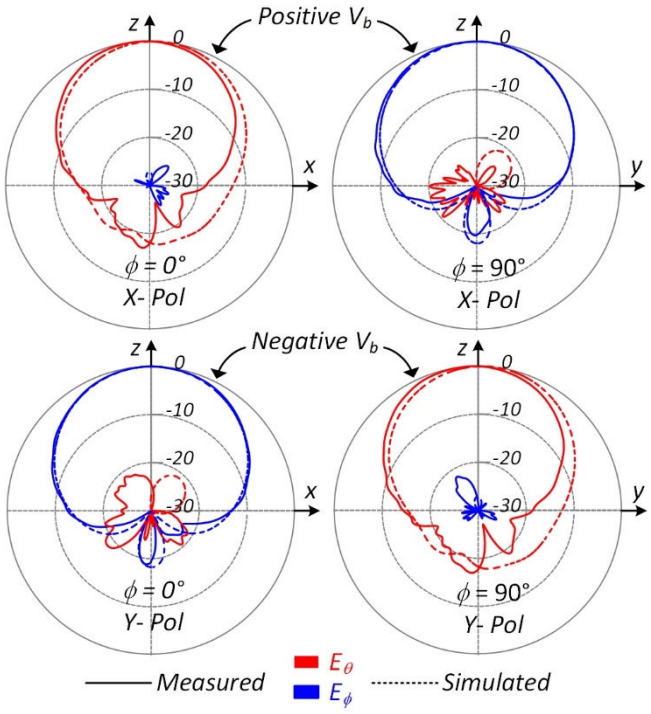

Fig. 35. Normalized radiation patterns for the improved solid-state PRA with 10 RF PIN didoes per gap.

backward radiation (negative *z*–direction) can be attributed to reduced ground plane dimensions in the prototype. The reduction in series resistance across the gap discontinuity leads to an increased measured gain of 3.5 dBi (compared to -4.84 dBi) and simulated radiation efficiency for 35%.

As mentioned, a trade-off between the DC control power requirements and the PRA radiation performance for the solid-state mechanism design was observed. The PRA measured gain and simulated efficiency were increased by 8.34 dBi and 26%, respectively, from increasing the number of RF PIN diodes 5×. While the increased electrically size (from the reducing the inductance across the gap) lead to some improvement, the reduced

ohmic losses from increasing the number of diodes is the main contributor in bettering radiation performance. Although a significant improvement has been achieved, the radiation efficiency from a traditional, unaltered patch antenna still far exceeds the solid-state and fluidic PRA model performance.

3.6 Liquid Metal PRA

The previous fluidic and solid-state reconfiguration mechanisms for polarization diversity both have limitations, mainly in the large reduction in radiation performance. In this design approach, the latest advancements in liquid metal technology are utilized as the reconfiguration mechanism for increased PRA radiation performance.

3.6.1 Concept and Modeling

Eutectic Gallium Indium (EuGI), a liquid metal at room temperature, forms stable fluidic structures due to its rheological properties at room temperature [26]. Replacing the high dielectric fluids used in the SIFN, discussed above, with EuGI creates a liquid metal switch (connecting the antenna arms to the central freed section) capable of exciting the two independent PRA patch antennas. The high conductivity of EuGI ($\sim 3.4\times10^6$ S/m) [26] significantly reduces the ohmic losses introduced by the reconfiguration mechanism. For comparison, gold, copper, and solder have a conductivity of 41×10^6 S/m, 58×10^6 S/m, and 7×10^6 S/m.

EuGI has been reported in a frequency reconfigurable slot antenna [16], where the authors printed a microfluidic channel traversing a slot antenna. Injecting or removing EuGI in the microfluidic channel alters the slot antenna's resonant frequency. In this design, achieving ohmic contact between the EuGI and the slot antenna copper traces was

not possible. Recently, fabrication techniques have been developed overcoming this issue making this fluidic switch a potential candidate as the reconfiguration mechanism in the PRA design discussed above.

Fig. 36 shows a depiction of the liquid metal PRA utilizing an updated SIFN. A superstrate layer of dimensions $W_s \times W_s \times H_s$ and material properties $\varepsilon_{rs} = \varepsilon'_{rs}\left(1 - j\tan\delta_{ds}\right)$ with ellipsoidal cross-section channels of dimensions H_c and W_c forms the SIFN. The SIFN dimensions have been reduced such that the superstrate (composed of a lossy dielectric) does not cover the PRA radiation slots. This reduces the fringing fields (near the slots) exposure to the lossy dielectric superstrate for improved radiation performance. Operationally, two sections of EuGI spanning the antenna arms width W electrically connects appropriate arms to the central feeds section to excited *X–pol* or *Y–pol* configurations. Fig. 36 depicts generalized inlets and outlets for the EuGI for simplicity in the diagram.

Fig. 37 illustrations the liquid metal PRA circuit model based on the principles of the previous circuit models presented in this dissertation. The EuGI high conductivity allows us to model the loaded microstrip gaps as simple transmission lines. In other words, the gap discontinuities can simply be removed and replaced by an equivalent transmission line; in this case, an equivalent transmission line loaded by the SIFN superstrate. Reiterating for clarity, the transmission lines denoted T_U, T_L, and T_F represent the lines of width W unloaded by the SIFN superstrate, the lines of width W loaded by the SIFN superstrate, and the lines of width $W + 2L_6$ loaded by the SIFN superstrate of the central

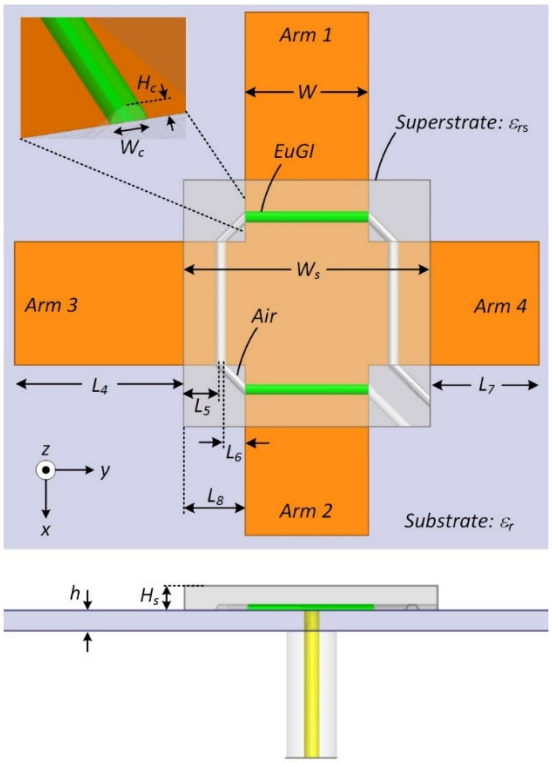

Fig. 36. Diagram for the liquid metal PRA with and updated version of the SIFN housing the fluidic channels

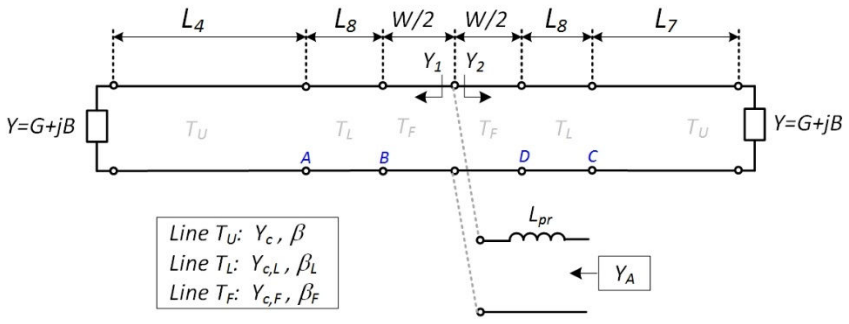

Fig. 37. Circuit model for the liquid metal PRA.

feed section, respectively. Examining the circuit model revels this liquid metal switch adds no additional loss mechanisms in order to achieved polarization diversity. In fact, ignoring

the different types of transmission lines by assuming $T_U = T_L = T_F$, one can observe the circuit model breaks down to the basic transmission line model of a traditional microstrip patch antenna. Thus, the liquid metal PRA operation (resonant frequency and input impedance) and radiation performance (gain and efficiency) should closely follow that of a traditional patch antenna.

3.6.2 Design and Prototype

As a proof-of-concept demonstration a static version of the liquid metal PRA was fabricated on Duriod 5880 (ε_r = 2.2, $\tan\delta$ = 0.0009, h = 1.58 mm) by creating a solder bridges (gaps filled with solder) across appropriate gaps for *X–pol* and *Y–pol* configurations in two separate antennas (Fig. 38). The conductivity of solder and EuGI are very similar and thus, solder provides an accurate estimation of what antenna performance would be achieved using EuGI. In order to account for the SIFN loading effect, a PDMS ($\varepsilon'_{rs} \sim 2.66$, $\tan\delta_s \sim 0.04$) superstrate layer of dimensions W_s = 20 mm and H_s = 2 mm was fabricated on the PRA. The PDMS layer was created by pouring liquid PDMS over the entire PRA top surface (with solder bridges). The liquid PDMS was allowed to cool then cut to specifications. Thus, these static "channels" created by the solder bridges are of unknown and non-uniform dimension, however can be approximated by W_c = 1 mm, H_c = 0.5 mm in the simulation model. The remaining dimension (in mm) are: L_4 = 13.65, L_5 = 2.85, L_6 = 1.85, L_7 = 8.85, L_8 = 5, W = 10.

Fig. 39 presents the static liquid metal PRA prototype measured reflection coefficient data compared to simulated and circuit model results. The measured and simulated center frequencies are in very close agreement near 2.46 GHz for both *X–pol*

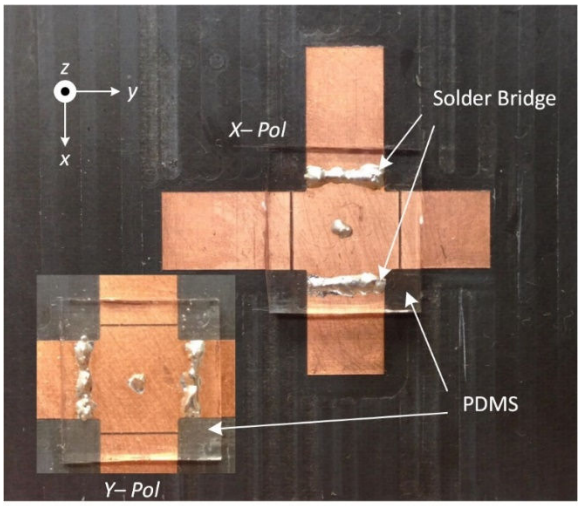

Fig. 38. Static prototype for the liquid metal PRA created by soldering appropriate gaps together and curing a PDMS layer over the structure.

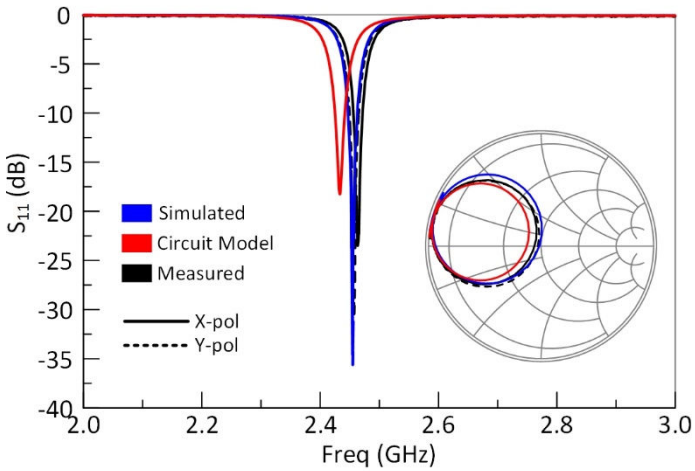

Fig. 39. Measured, simulated, and circuit model reflection coefficient data for the static liquid metal PRA prototype.

and *Y–pol* configurations. The circuit model center frequency at 2.43 GHz differs from simulated and measured results by 1.2 % due to additional capacitive and inductive effects

introduced from the solder bridges (accounted for in simulation, difficult to account for in the circuit model). The FBW and Smith Chart impedance curves are in close agreement.

Fig. 40 shows the simulated and measured static liquid metal PRA normalized radiation patterns in the two principle planes for *X–pol* and *Y–pol* configurations. The simulated and measured patterns are in close agreement and slight difference can be contributed to the prototype's reduced ground plane compared to the simulation model ground plane and the anechoic chamber's measurement accuracy utilized in this experiment. The static liquid metal PRA prototype shows orthogonal polarization switching between the two polarization states and very low cross polarization levels (-18 dB max). A measured gain of 6.93 dBi and simulated efficiency of 78% shows the liquid metal PRA radiation performance approaches that of a traditional patch antenna with the added benefit of polarization diversity.

3.7 Discussion II

All the PRA reconfiguration mechanisms presented above share ability to enable good linear polarization switching. These mechanisms were found to have design trade-offs, limitations, and advantages between them which are summarized in Table 2 with respect to six main performance metrics: (1) electrical size ratio, (2) measured gain, (3) simulated efficiency, (4) cross polarization levels, (5) DC control power requirements, (6) switching speed. In (1), the metric for comparison will be the ratio of the simulated center frequency with the reconfiguration mechanisms present to the simulated center frequency with the mechanism removed, gaps completely metalized, and all other dimensions kept the same (this denotes a traditional patch antenna). Thus, an electrical size ratio greater

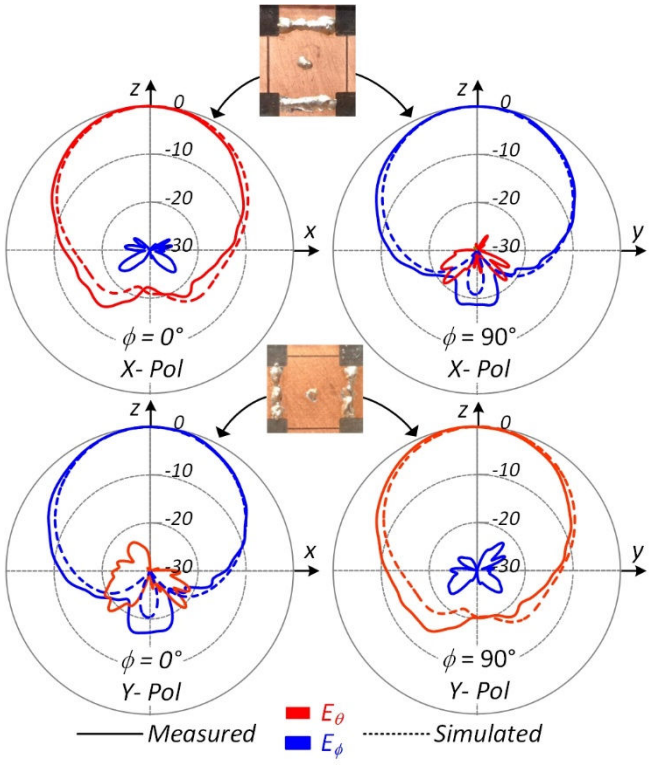

Fig. 40. Simulated and measured normalized radiation patterns at 2.46 GHz for the static liquid metal PRA prototype.

Table 2. Performance summary for the PRA with the fluidic, solid-state, and liquid metal reconfiguration mechanisms.

	Electrical Size Ratio	Measured Gain	Simulated Efficiency	Cross polarization level	DC Control Power Requirements	Switching Speed
Fluidic	1.11	2 dBi	22 %	-17.5 dB	N/A	~ ms
2 RF PIN Diodes/Gap	0.90	-4.84 dBi	8 %	-13.3 dB	40 mA	~ μs
10 RF PIN Diodes/Gap	0.97	3.5 dBi	35 %	-18.4 dB	200 mA	~ μs
Liquid Metal	0.99	6.93 dBi	78 %	-18.4 dB	N/A	N/A

than 1 signifies an electrical shortening and less than 1 signifies an electrical lengthening with the reconfiguration mechanism present. In (4) the maximum measured cross polarization levels are compared.

The electrical size ratio shows the fluidic PRA model operates electrically larger than a traditional patch antenna (from the series capacitance introduced across the gap), while all other PRA models are electrically shortened (from the series inductance across the gap). However, the 10 RF PIN diode and liquid metal PRA add little inductance, thus resembling the electrical size of a traditional patch antenna. As mentioned, the reduced ohmic loss from the series resistance terms across the gap greatly increase the measured gain and simulated efficiency in the 10 RF PIN diode and liquid metal PRA models. The liquid metal PRA gain and efficiency numbers are highest, nearing those of a traditional patch antenna, and show the most attractive radiation performance.

The cross polarization levels are almost consistence between the reconfiguration mechanisms (near -18 dB) with the exception of the 2 RF PIN diode PRA model at -13.3 dB. The source of this difference arises from the DC grounding lines coupling RF current from the active patch antenna. Cross polarization levels are increased when these RF currents are orthogonal to the active radiating patch. These DC grounding lines are most susceptible to RF coupling in the 2 RF PIN diode PRA as RF currents are forced through a small number of current paths increasing the probability of coupling.

The DC control requirements for the solid-state PRA models are easily quantified where a trade-off was found between power requirements and radiation performance. The fluidic and liquid metal reconfiguration mechanisms require a peristaltic pump (operating

on a DC voltage) in a closed loop system to push the fluid or liquid metal sections in appropriate positions of *X–pol* or *Y–pol* configurations. A low-power, low-cost, small portable pump was utilized to test the fluidic PRA however, the pump proved unreliable as it was difficult to position the DI water sections appropriately. A more robust and efficient higher cost pump could mediated issues encounter during experiment. The power requirements of such pump are unknown and thus not reported in Table 2. No dynamic testing was completed for the liquid metal PRA and thus, no power requirements are reported as well. However, the power requirements for both fluidic and liquid metal PRA iterations will be identical since the same pump can likely operator both designs.

Finally, the switching speed of each reconfiguration mechanism is discussed. The electrically driven solid-state PRAs can be switched at speeds on the order of ~ 1 μs whereas fluidic and liquid metal PRAs will have inherently slower switching speeds due to the kinetic operation of a pump. In the fluidic PRA testing with a basic, low-cost, and readily available peristaltic pump ~ ms switching speeds were observed to be possible. No dynamic testing was completed for the liquid metal PRA since only a static prototype with the solder bridges was developed and thus, no switching speed performance is reported. Peristaltic pumps capable of moving small volumes of fluids at high speeds may improve speed performance, but these were not extensively surveyed so an objective comparison between switching speed was limited to this physical argument on the switching mechanism.

CHAPTER IV

FREQUENCY AND POLARIZATION RECONIFURABLE CROSSED MICROSTIRP ANTENNA

This chapter presents a frequency and polarization reconfigurable antenna (FPRA) based on the same antenna topology utilized in Chapter III. Fluids with varying dielectric properties are utilized to achieve frequency tuning and linear polarization switching with a similar SIFN as discussed in Section 3.2. Variable capacitors (varactors) are added to the solid-state PRA to achieve similar frequency and polarization reconfiguration capabilities. Circuit models are utilized as before to explain the impacts on antenna performance from the tuning mechanism presence in the FPRA designs. Similar comparisons between the fluidic and solid-state approaches highlight the reconfiguration mechanisms key design trade-offs, limitations, and advantages. From this comparison, a hybrid solution employing both fluidic and solid-state mechanisms is presented and exhibits the best achievable performance.

4.1 Fluidic FPRA

4.1.1 Concept and Modeling

In order to achieve frequency tuning in the fluidic PRA model, no changes to the design are necessary. Fig. 19 shows that varying the loading fluid dielectric changes the series capacitive coupling along the antenna arms. Fig. 41 depicts the loading fluid effect along a small section of the antenna (since the antenna circuit model models the antenna arms as transmission lines). The antenna's resonant frequency will be proportional to the

loading capacitance by (4.1). Thus, by varying the fluid dielectric constant, the antenna's resonant frequency can be controlled.

$$\omega_0 \propto \frac{1}{\sqrt{L\left(C+C'\right)}} \tag{4.1}$$

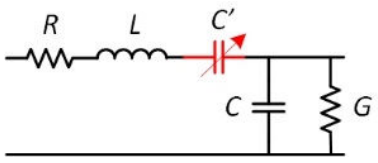

Fig. 41. Effective of adding a variable series capacitance to a lumped element transmission line model.

Although no design changes are necessary to achieve the desired frequency diversity, more advanced fabrication techniques are utilized to improve the overall radiation performance. Fig. 42 presents the fluidic FPRA using the modified SIFN (as used in the liquid metal PRA). The SIFN dimensions ($W_s \times W_s \times H_s$) have been reduces such that the superstrate (a lossy dielectric material) does not cover the radiating slots, reducing the fringing fields exposure to the lossy dielectric material for improved radiation performance. Channels etched in the superstrate with elliptical cross sections of dimensions W_c and H_c compose the SIFN. A dielectric fluid with material properties $\varepsilon_{r1} = \varepsilon'_{r1}\left(1 - j\tan\delta_{d1}\right)$ loads appropriate gaps to excite *X–pol* (show in Fig. 42) or *Y–pol* configurations. The fluid dielectric constant ε'_{r1} controls the FPRA resonant frequency. From (4.1) and Fig. 19, as the loading fluid dielectric constant decreases, the resonant

frequency will increase and vice versa. The gaps along the inactive antenna are unloaded (channels only contain air).

Fig. 43 shows the fluidic FPRA circuit model used to computed to antenna input impedance ($Z_A = 1/Y_A$) and developed using the same principles as the previous circuit models presented in this work. The loaded microstrip gap discontinuities are model by a π–network of admittances Y_g and Y_p, defined by (3.1) and (3.2), respectively, and computed from full-wave simulations using (3.3) and (3.4). The transmission lines denoted T_U, T_L, and T_F represent the lines of width W unloaded by the SIFN superstrate, the lines of width W loaded by the SIFN superstrate, and the lines of width $W + 2L_6$ loaded by the SIFN superstrate at the central feed section, respectively. Again, the probe inductance L_{pr} has been accounted for and the inactive antenna has been ignored. This circuit model highly resembles the fluidic PRA model with updated dimensions for the FPRA. Thus, the operation and radiation principles learned from the PRA directly apply to this FPRA model. Specifically, the loading fluid loss tangent effect on radiation (Fig. 30) should be consider when choosing appropriate fluids. Defining an acceptable radiation efficiency as > 50%, requires a fluid loss tangent of < 0.02 for the fluidic PRA (with a PDMS superstrate) to meet this performance metric. Thus, fluids processing a loss tangent up to 0.02 will be considered.

4.1.2 Performance Study

Fluids with a wide range of dielectric constants and a 0.02 maximum loss tangent in the desired frequency range are difficult to come by at the time of this report. Thus, no

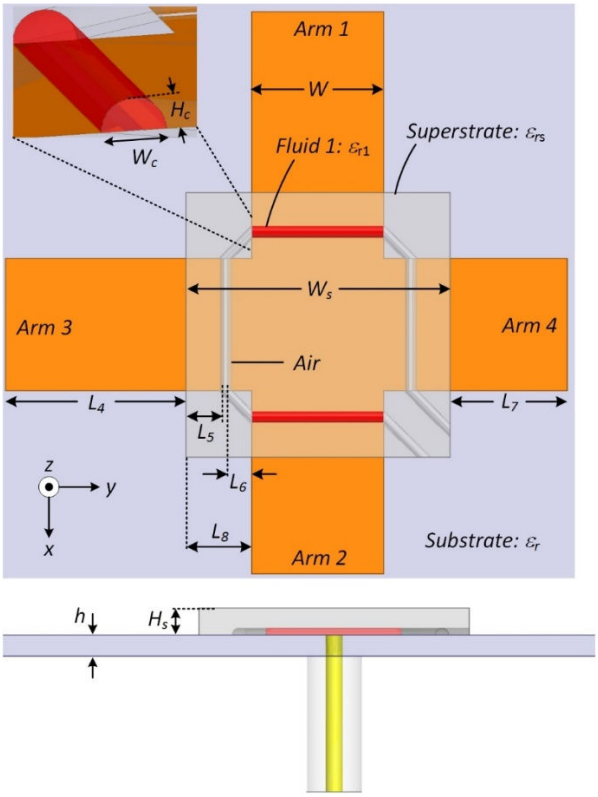

Fig. 42. Fluidic FPRA with an updated SIFN identical to the SIFN in the liquid metal enabled PRA.

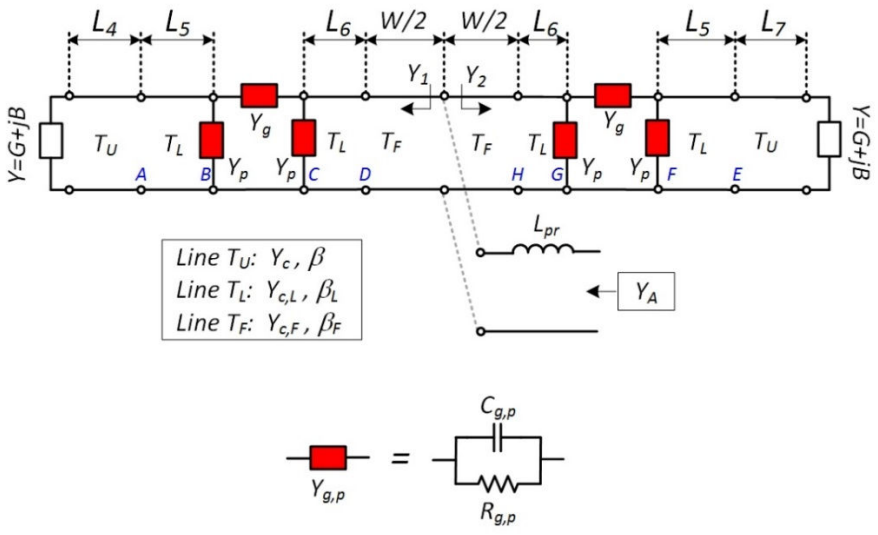

Fig. 43. Circuit model for the fluidic FPRA.

measured data from a prototype will be available. However, the fluidic FPRA potential performance can be examined from simulation and analytical models in order to find any design considerations. Fig. 44 – Fig. 47 show the simulated and circuit model reflection coefficient data for a sampling of dielectric strength loading fluids with loss tangents of 0 and 0.02. The FPRA dimensions (in mm) are: L_4 = 19.15, L_5 = 2.85, L_6 = 1.85, L_7 = 9.15, L_8 = 5, W = 10. A PDMS ($\varepsilon'_{rs} \sim 2.66$, $\tan\delta_s \sim 0.04$) superstrate and Duriod 5880 (ε_r = 2.2, $\tan\delta$ = 0.0009, h = 1.58 mm) substrate are consider in the simulated and analytical models.

Fig. 44 – Fig. 47 show a 700 MHz simulated center frequency tuning range from 2.645 GHz (ε'_{r1} = 80) to 3.345 GHz (ε'_{r1} = 20) when utilizing lossless fluids for both *X–pol* and *Y–pol* configurations. This tuning range slightly decreases when using more realistic fluids possessing a 0.02 loss tangent as the log magnitude of S_{11} goes above -10 dB at ε'_{r1} = 20. However, this can be accounted for by altering the probe feed location for the best impedance match with $tan_{\delta 1}$ = 0.02 (since the current feed location was found assuming lossless fluids). The close agreement between the circuit model and simulated results show the circuit model's versatility of predicting accurate performance across a wide range of fluids. The tuning range can be further increased using fluids with dielectric constants above 80. The upper limit of 80 was chosen to resemble water (this highest dielectric strength fluid know to be readily available at the time of this work).

Fig. 48 shows the simulated normalized radiation patterns for the ε'_{r1} = 80, 40, and 20, with $tan_{\delta 1}$ = 0 and 0.02, states (corresponding to frequencies of 2.465, 2.963, and 3.345

GHz, respectively) for both *X–pol* and *Y–pol* configurations. The curves indicate good linear polarization switching throughout the frequency tuning range. The nearly identical

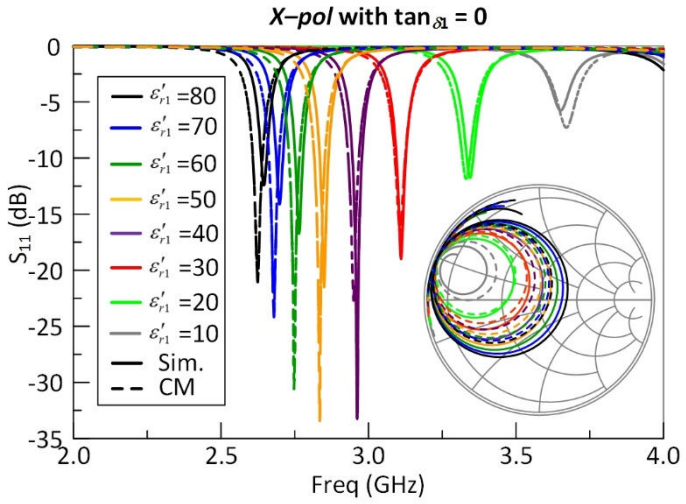

Fig. 44. Simulated (solid) and circuit model (dashed) reflection coefficient data for the *X–pol* fluidic FPRA for a sampling of different dielectric strength loading fluids a loss tangent of 0.

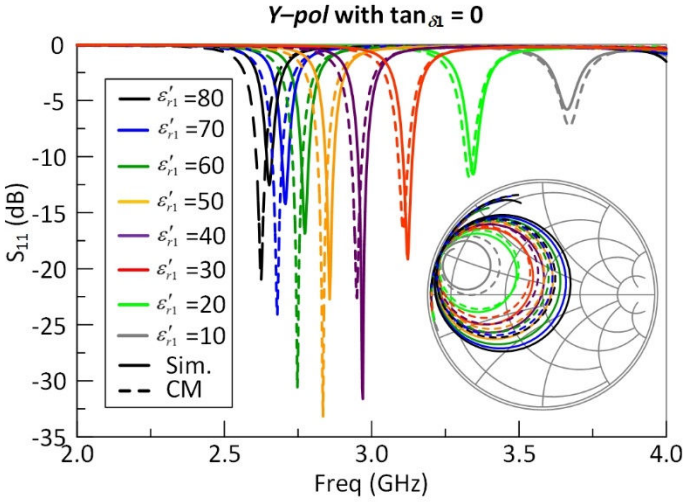

Fig. 45. Simulated (solid) and circuit model (dashed) reflection coefficient data for the *Y–pol* fluidic FPRA for a sampling of different dielectric strength loading fluids a loss tangent of 0.

main beam patterns indicate the resonant mode field structure and basic patch behavior remains intact despite the loading fluid presence across the gap. Furthermore, the fluidic

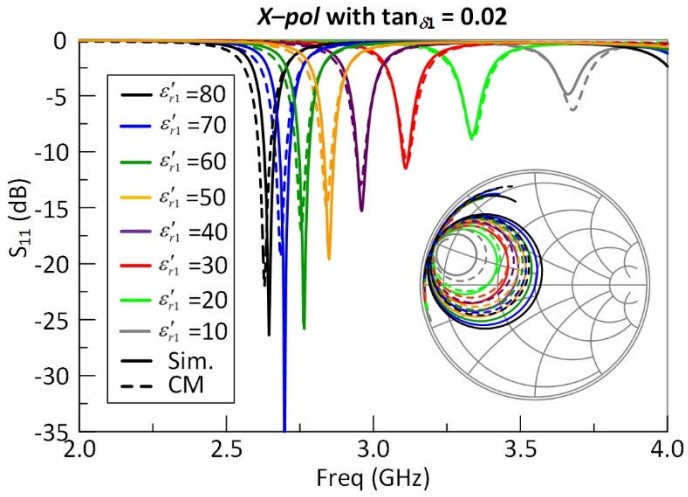

Fig. 46. Simulated (solid) and circuit model (dashed) reflection coefficient data for the *X–pol* fluidic FPRA for a sampling of different dielectric strength loading fluids a loss tangent of 0.02.

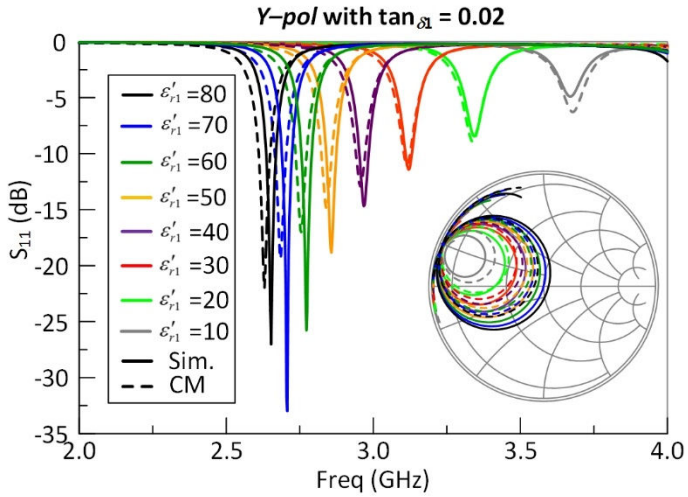

Fig. 47. Simulated (solid) and circuit model (dashed) reflection coefficient data for the *Y–pol* fluidic FPRA for a sampling of different dielectric strength loading fluids a loss tangent of 0.02.

tuning mechanism maintains classic patch antenna performance throughout reconfiguration. A maximum cross polarization level of -20 dB proves little coupling to the isolated arms occurs.

Fig. 49 and Fig. 50 display the fluidic FPRA simulated gain and radiation efficiency performance across the frequency tuning range (2.465 – 3.345 GHz) achieved

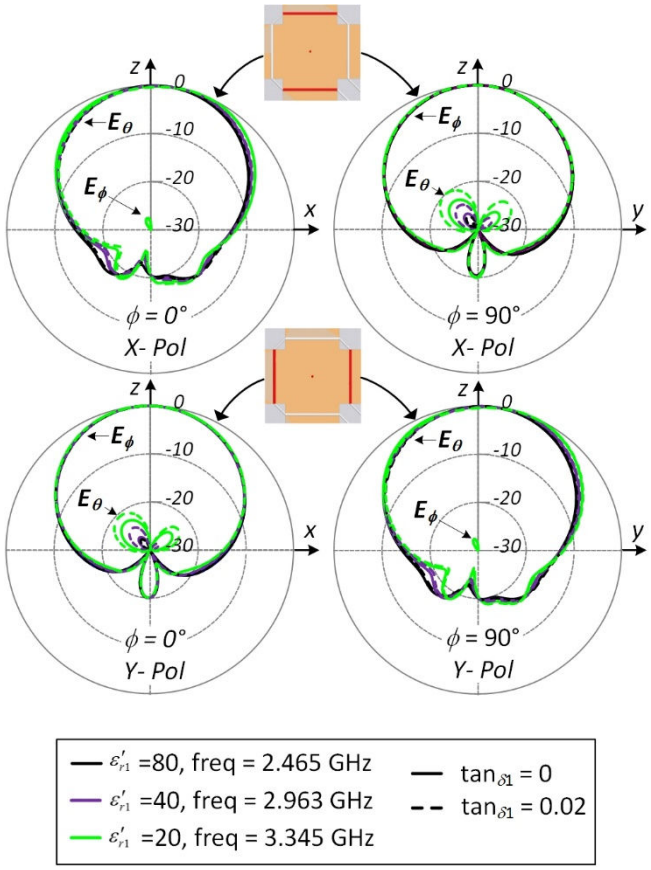

Fig. 48. Simulated normalized radiation patterns for the fluidic FPRA at six different frequency states for both *X–pol* and *Y–pol* configurations.

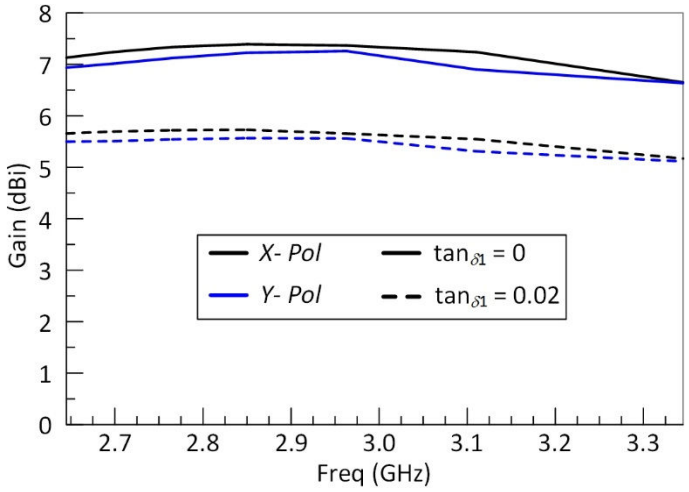

Fig. 49. Simulated gain at the center frequency for the dielectric constant cases from 80 to 20 and 0 and 0.02 loss tangents.

using fluids with 80 > ε'_{r1} > 20 dielectric constants. The results are presented with both lossless ($tan_{\delta 1}$ = 0) and lossy ($tan_{\delta 1}$ = 0.02) fluids for comparison. As expected from previous results with the fluidic PRA model, utilizing lossless fluids maintains the classical radiation performance of a traditional patch antenna (gain near 8 dBi and efficiency between 80 – 90%) for each tuning state. The gain and efficiency performance suffer as the fluid loss tangent increases. The gain and efficiency drop to 5.1 dBi and 56 %, respectively, at $tan_{\delta 1}$ = 0.02. The gain values drop a higher frequencies since the aperture efficiency (radiation efficiency only factors in the power accepted by the antenna, thus, does not include losses from the impedance mismatch).

Fig. 51 shows the electrical size ratio (resonant frequency at the tuning state/resonant frequency with SIFN removed and gaps metalized) increases as the loading

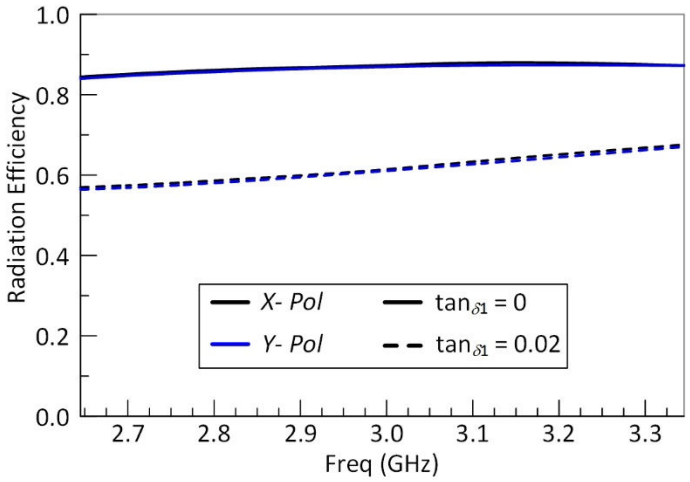

Fig. 50. Simulated efficiency at the center frequency for the dielectric constant cases from 80 to 20 and 0 and 0.02 loss tangents.

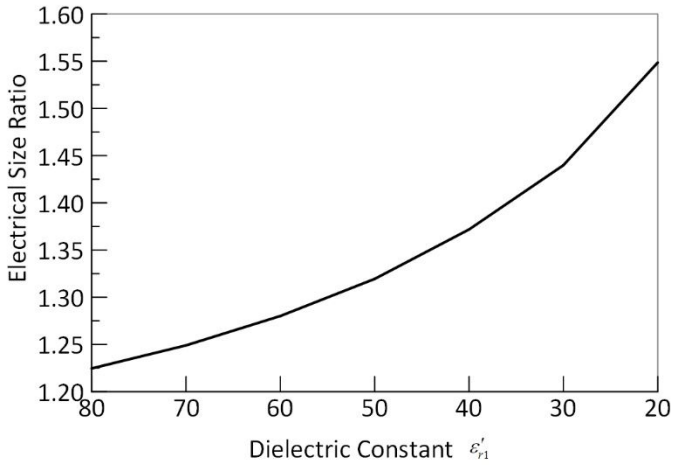

Fig. 51. Electrical size ratio at each tuning range for the fluidic FPRA.

fluid dielectric constant deceases causing the operating frequency to increase.

The results from this performance study with fluids of hypothesized dieletric properties proves with proper fluids, the FPRA fluidic reconfiguration mechansim facilitates traditional patch antenna radaition performance across the tuning states

(frequency and polarization). Unfortunatly, at the time of this report, fluids with such diversity are difficult to find. Thus, only the potiental performance can be examined at this point in time. As such fluids become available or are found through experimentation, the simulation and analytical models developed can be helpful tools in designing an FPRA for a specific application and frequency range.

4.2 Solid-State FPRA

The previous section showed a fluidic reconfiguration mechanism has potential to be utilized for a FPRA. However, the feasibility of this approach suffers from a lack of available low-loss dielectric fluids with a wide range of dielectric strengths. This further encourages research for finding such fluids via a joint effort between material science and RF/microwave engineers. At the time being, an operational FPRA using present day solid-state technologies will be explored as the tuning mechanism. The RF PIN diodes introduced in the solid-state PRA designs from the previous chapter are combined with packaged varactor diodes in order to achieve both frequency and polarization tuning.

4.2.1 Concept and Modeling

In the solid-state FPRA design, RF PIN didoes are used to achieve polarization switching (as before) and varactors are introduced to enable frequency tuning. Thus, the design principles and conclusions draw from the solid-state PRA models can be employed. It was found that increasing the number of RF PIN diodes across the gap, largely increases radiation performance at the cost of DC control power requirements. This work assumes no power restriction to drive the control circuit. Another important design consideration for this FPRA model is the simplicity involved in controlling the reconfiguration

mechanism. The PRA models presented in the previous chapter share this design trait by easily positioning fluids/liquid metals via a single voltage (operating a peristaltic pump) or changing the bias voltage polarity (on a bias tee network) to enable polarization switching. In other words, a single control voltage operates the reconfiguration mechanisms under simple biasing schemes (if any) to reduce complexity. The fluidic FPRA model also shares this design trait by having multiple sections of different dielectric strength fluids in a closed loop system where the pump "on" duration time (again via a single control voltage) defines which fluids are pushed over appropriate gaps. This solid-state FPRA design will operate on a single control voltage and simple bias scheme as well for proper comparison between reconfiguration mechanisms.

Fig. 52 presents the solid-state FPRA model which employs the same basic structure of the solid-state PRA model presented in the previous chapter. Although Fig. 52 shows five RF PIN diodes and four varactors, the following discussion and analysis will apply to any number of diodes. Varactors are placed across additional gaps along each microstrip arm which introduce a variable series capacitance C_v, similar to the series capacitance introduced by the loading dielectric fluid in the fluidic FPRA. Thus, the value of C_v will determine the antenna's resonant frequency. In order for the antenna to operate on a single control voltage, both RF PIN diodes and varactor must be appropriately biased under the same bias voltage. RF PIN diodes operate as a switch and turned "on" under forward bias conditions when a forward DC current (from anode to cathode) or positive bias voltage applied at the anode. Varactors operate under an electrostatic (zero current) reverse voltage (voltage drop from cathode to anode). As this reverse voltage increases,

the capacitance decreases. The varactors are placed in opposite anode-cathode orientations as the corresponding RF PIN diodes for each antenna arm, as seen in Fig. 52. Furthermore, the RF choke bias lines are placed after the varactors (away from the center feed section) such that the bias voltage will operated on both PIN diodes and varactors simultaneously. Therefore, when the PIN diodes are under forward bias conditions (forward current applied), the varactors are under reversed bias conditions. In order to keep these conditions meet since the varactor diodes are open at DC breaking the current across the PIN diodes, a resistor R_v must be placed in parallel with the varactors. This maintains the current on the PIN didoes and the voltage drop across the varactors. Operationally, the DC bias

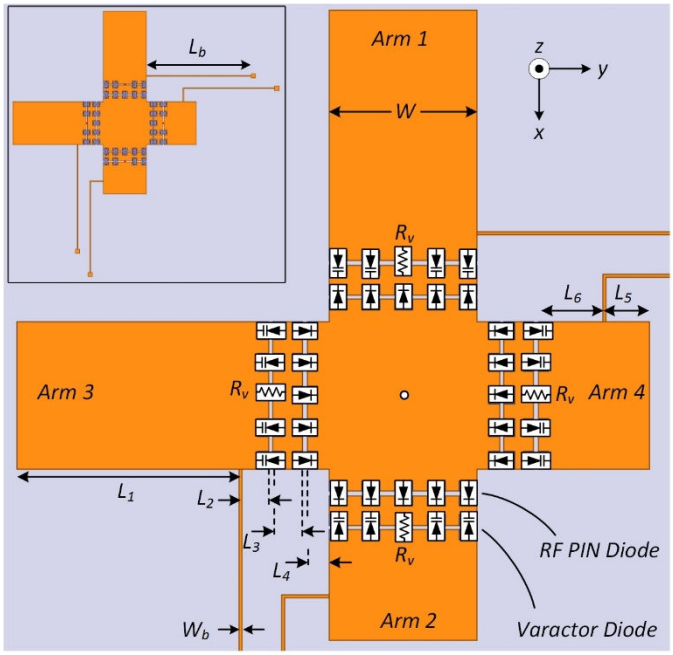

Fig. 52. Solid-state FPRA utilizing RF PIN diodes for polarization switching and varactors for frequency tuning operating under a single control voltage.

voltage V_b polarity applied to the center feed section controls *X–pol* (positive) or *Y–pol* (negative) configurations and the V_b magnitude dictates the antenna's resonant frequency.

Fig. 53 shows the solid-state FPRA antenna circuit model based off the solid-state PRA circuit model. Additional π–network models for the gap discontinuities with integrated varactors are included at appropriate locations. The varactors have been classically modeled as a series resistance R_{vi}, the varactor internal resistance, variable capacitor C_v, and inductance L, from packaging. These values are found in datasheets. Once again, a shunt inductance L_b (computed from full-wave simulations) models the bias lines and a series inductance L_{pr} (computed from basic wire inductance equations) models the feed probe. The presence of both series capacitive coupling and series inductance across the gaps means this antenna can operate electrically larger or smaller than its traditional counterpart (diodes removed and gaps filled). Furthermore, ohmic losses from small values of R_v may affect the radiation efficiency as RF current is allowed to dissipate across the resistor. To avoid this, R_v should be kept as large as possible (discussed more in the proceeding section).

4.2.2 Control Analysis

While the previous circuit model (Fig. 53) models the solid-state FPRA's RF performance, the DC circuit model (shown in Fig. 54) allows us to find the design parameters for proper antenna operation. The model in Fig. 54 is generalized to include n_d RF PIN diodes and n_v varactor diodes. As mention previously, the PIN diodes operate as a switch and are activated with an applied forward current (anode to cathode). The applied current magnitude sets the PIN diode forward resistance R_f and is typically rated for a

current magnitude range which sets $R_f <$ some desired value. Fig. 55 shows the DC circuit with a positive applied bias voltage (a negative bias voltage will switch the current directions and voltage polarities in the figure). The PIN diodes are modeled as a forward voltage drop V_f with current i_p across each diode. The resistor in parallel with the varactor diodes R_v sets the current i_p and thus, the PIN diode forward resistance R_f. From Fig. 55 it can be show that the current across the PIN diodes i_p, the current drawn from the power source i_s, and the voltage across the varactors V_{var} are (4.2), (4.3), and (4.4), respectively. The V_{var} term defines the varactor series capacitance C_v and consequentially the FPRA resonant frequency. From (4.2), as V_b increases, i_p increases and changes R_f. Thus, at different frequency reconfiguration states, the value of R_f alters the FPRA impedance match and radiation performance.

$$i_p = \frac{V_b - V_f}{n_d \cdot R_v} \tag{4.2}$$

$$i_s = 2n_d i_p \tag{4.3}$$

$$V_{\text{var}} = V_b - V_f \tag{4.4}$$

Combining (4.2), (4.3), and (4.4) we find that,

$$i_s = \frac{2V_{\text{var}}}{R_v} \tag{4.5}$$

From (4.5), in order to reduce the source current (reducing the power drawn by the source, $V_b i_s$) R_v should be kept as large as possible. A large R_v value also make this integrated resistor negligible at RF frequencies to reduce ohmic losses and maintain radiation performance, as previously mentioned. The current on the integrated resistor i_{rv}

(a surface mounted chip resistor) must also be kept to a minimum in order to reduce heating on the antenna surface. This current can be computed from (4.6) and shows that as more PIN diodes are utilized to reduce ohmic losses and boost radiation performance, heating on the antenna surface will increase as the current on the integrated chip resistor raises pointing to another design trade-off.

$$i_{rv} = n_d i_p \tag{4.6}$$

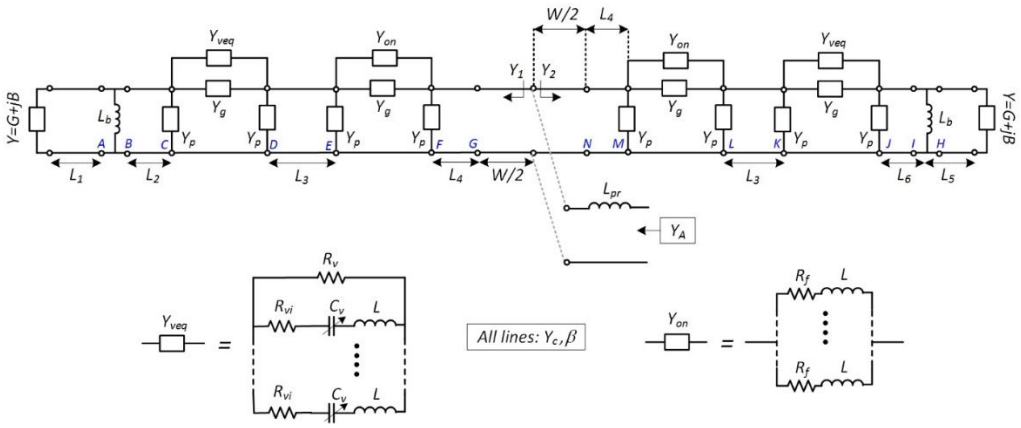

Fig. 53. Circuit model for the solid-state FPRA.

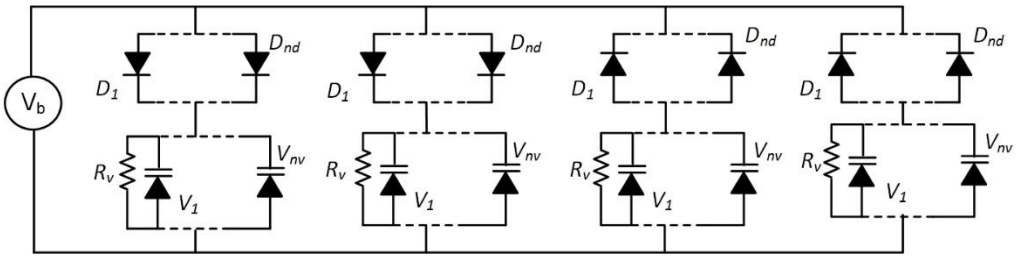

Fig. 54. DC circuit model for the solid-state FPRA control analysis.

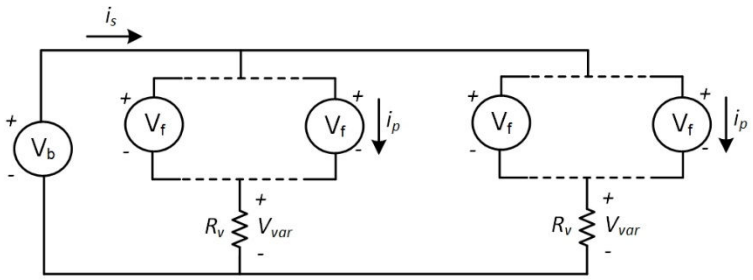

Fig. 55. Solid-state FPRA DC circuit model with a positive bias voltage applied.

4.2.3 Design and Prototype

Fig. 56 displays the solid-state FPRA prototype designed on Duriod 5880 ($\varepsilon_r = 2.2$, $\tan\delta = 0.0009$, $h = 1.5748$ mm) with mounted readily available RF PIN [21] and varactor diodes [27] with $L = 0.7$ nH, $R_{vi} = 0.35$ Ω, and $1.77 \text{ pF} < C_v < 9.24$ pF (roughly 5:1 ratio capacitance range) for $30 \text{ V} > V_{var} > 0$ V. Fig. 57 shows a plot of the forward (also referred to as series) resistance R_f with respect to the applied forward current i_p. As i_p increases R_f decreases, and when i_p reaches 1 mA R_f drops to ~ 3 Ω. Moreover, when $10 \text{ mA} < i_p < 100$ mA, R_f remains nearly constant around 1 Ω. The plot in Fig. 57 depicts an ideal scenario. Surface mounting effects from soldering and placement along the shared gap will limit the i_p of each individual diode causing R_f to increase. This work assumes a minimum achievable value of $R_f = 2 - 3$ Ω.

As seen in the solid-state PRA from the previous chapter, utilizing 10 RF PIN diodes per gap yields reasonable radiation performance. In this FPRA design, using 10 PIN diodes per gap forces large current dissipation on the integrated chip resistor since a high bias voltage must be applied to the varactor. The solid-state FPRA design utilizes 5 RF PIN diodes (as seen in Fig. 56) to maintain radiation performance and limit current

dissipation (reducing heating) on the integrated chip resistor. Furthermore, 4 varactor diodes (Fig. 56) are placed across the additional gaps to reduce the effects of R_{vi} on

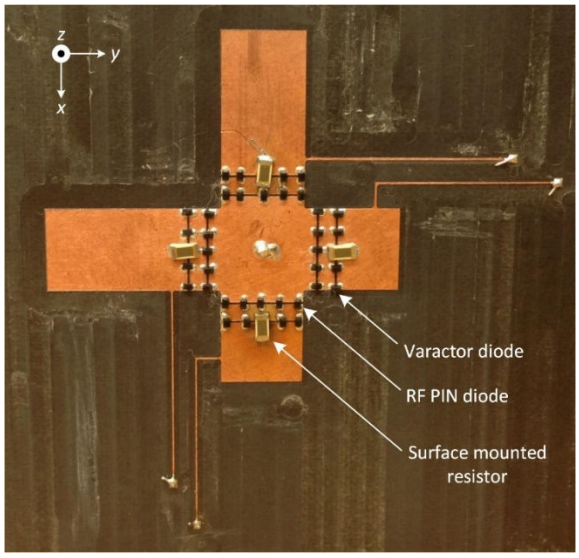

Fig. 56. Solid-state FPRA prototype enabled by readily available RF PIN diodes and varactors.

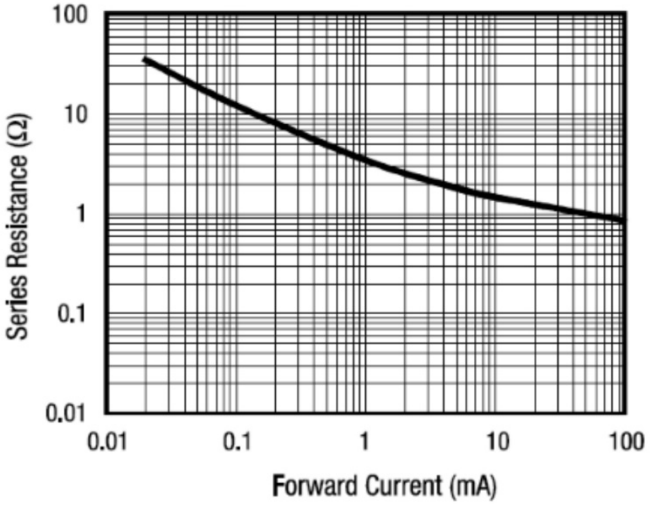

Fig. 57. Forward (series) resistance of the RF PIN diodes utilized in this work. [21]

radiation performance. With these diode numbers, R_v = 100 Ω to set the forward current of i_p > 1 mA (for reasonable R_f values) at $|V_b|$ > 1.4 V. In this work two 200 Ω surface mounted resistors are combined in parallel (stack one on top of the other in Fig. 56) to reduce the current dissipated on individual resistors. The remaining prototype dimensions in Fig. 56 (in mm) are: L_1 = 15.1, L_2 = 1.9, L_3 = 2, L_4 = 1.5, L_5 = 3, L_6 = 4.5, L_b = 24.4, W_b = 0.3, W = 10.

Table 3 shows the solid-state FPRA prototype DC control parameters of interest where P_s and P_r refer to the power drawn by the source and the power dissipated on the integrated chip resistor, respectively. Fig. 58 – Fig. 60 show the prototype's measure reflection coefficient data compared to the simulated and circuit model data for $|V_b|$ = 1, 3, and 10 V (C_v = 8.83, 5.14, and 3.01 pF), respectively. The simulated and circuit model data assume R_f = 3 Ω for all reconfigurations states. Only results at $|V_b| \leq$ 10 V are presented as at $|V_b| >$ 10 V the surface resistors begin to heat up past their thermal threshold, as seen in Fig. 61. The resistors are rated up to 1 W of dissipated power, however, a cooling mechanism must be introduced to dissipate excessive heating. As stated previously, control simplicity was a requirement for this antenna to properly compare the fluidic, solid-state, and hybrid reconfiguration mechanisms. A cooling system adds complexities and is out of the scope for this project.

The results in Fig. 58 – Fig. 60 demonstrate a measured center frequency tuning range of 100 MHz from 2.33 GHz ($|V_b|$ = 1 V) to 2.43 GHz ($|V_b|$ = 10 V) for both *X–pol* and *Y–pol* configurations. Simulated and measure response curves are in close agreement. The upward shift in center frequency (up to 1.6 % different than measurement) occurs

because an additional series inductance (difficult to account for in the circuit model) exists in the measured and simulated models from currents combining and reforming between the two gap discontinuities. The FBWs for all curves are in good agreement and typical for a resonant patch antenna (~ 1.6 %). At $|V_b|$ = 1 V (Fig. 58) the measured Smith Chart curves has a large contrast to the simulated and circuit model curves because the low current applied to the RF PIN diodes sets R_f higher in measurement than the assumed value of 3 Ω in the analytical and full-wave models. For $|V_b|$ = 3 and 10 V, R_f reaches a more desired value, and all curves in Fig. 59 and Fig. 60 show good agreement. For completeness, Fig. 62 presents the potential performance assuming a cooling system was present and the full range of tuning voltages could be utilized. The center frequency could be shifted up to 2.555 GHz at $|\underline{V_b}|$ = 20.89 V and still achieve good impedance matching. This more than doubles the center frequency range from 100 MHz with no cooling system to ~ 215 MHz with active cooling at higher bias voltage magnitudes.

Table 3. DC control parameters for the solid-state FPRA prototype.

$\|V_b\|$ (V)	C_v (pF)	i_p (mA)	P_s (mW)	P_r (mW)
1	8.83	0.22	2.0	0.01
2	6.22	2.22	44.0	0.06
3	5.14	4.22	127	2.23
5	4.06	8.22	411	8.45
10	3.01	18.22	1.82k	41.5
20	2.18	38.22	7.64k	182.6
30	1.80	58.22	17.5k	423.7

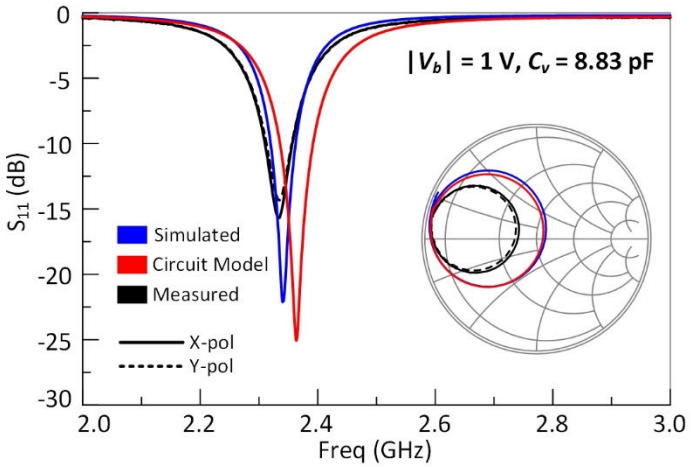

Fig. 58. Measured reflection coefficient for the solid-state FPRA with a bias voltage magnitude of 1 V compared to circuit model and simulated results.

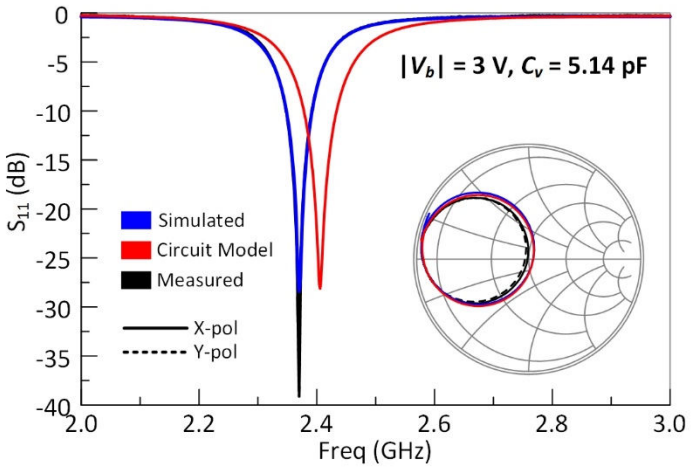

Fig. 59. Measured reflection coefficient for the solid-state FPRA with a bias voltage magnitude of 3 V compared to circuit model and simulated results.

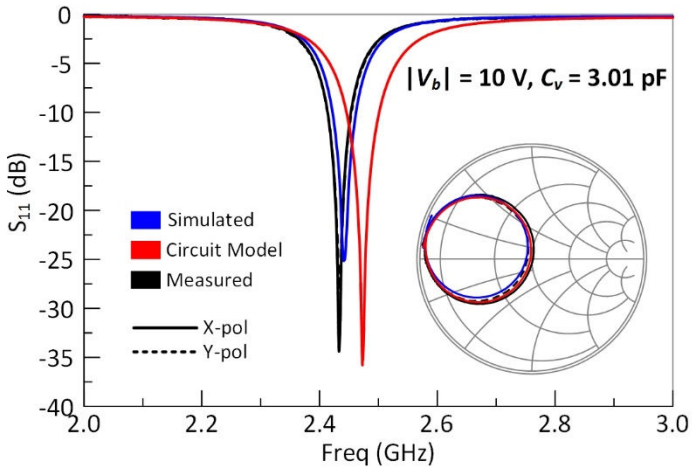

Fig. 60. Measured reflection coefficient for the solid-state FPRA with a bias voltage magnitude of 10 V compared to circuit model and simulated results.

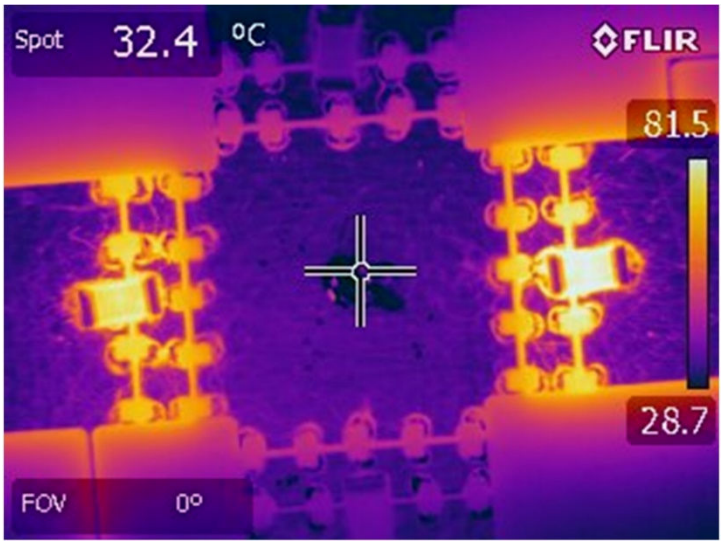

Fig. 61. Thermal image of the prototype solid-state FPRA at a bias voltage magnitude above 10 V.

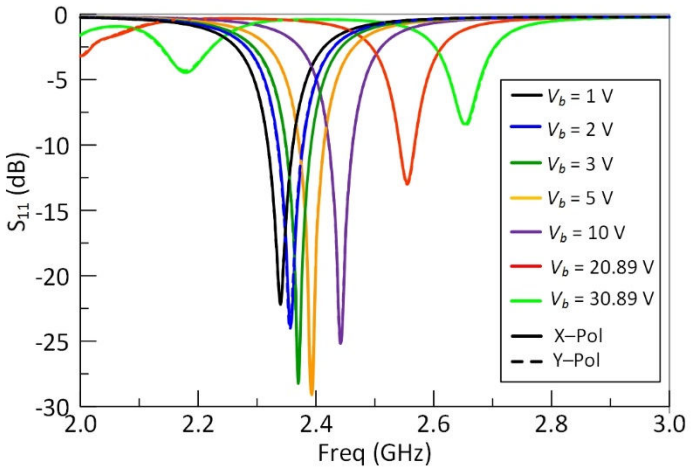

Fig. 62. Potential frequency tuning performance from the simulated solid-state FPRA model assuming a cooling mechanism could be utilized at higher bias voltages.

Fig. 63 – Fig. 65 present the simulated and measured normalized radiation patterns for $|V_b|$ = 1, 3, and 10 V, respectively, at the corresponding reconfiguration state center frequencies. The patterns demonstrate good linear polarization switching between *X–pol* and *Y–pol* states. The main beams resemble classic patch antenna performance and are nearly identical for all three reconfigurations states. The measured results show a reasonable maximum cross polarization level of -15 dB which agree with results from the solid-state PRA models in the previous chapter (Table 2). Differences in the simulated and measured results can be attributed to measurement tolerances and the measured prototype smaller ground plane size.

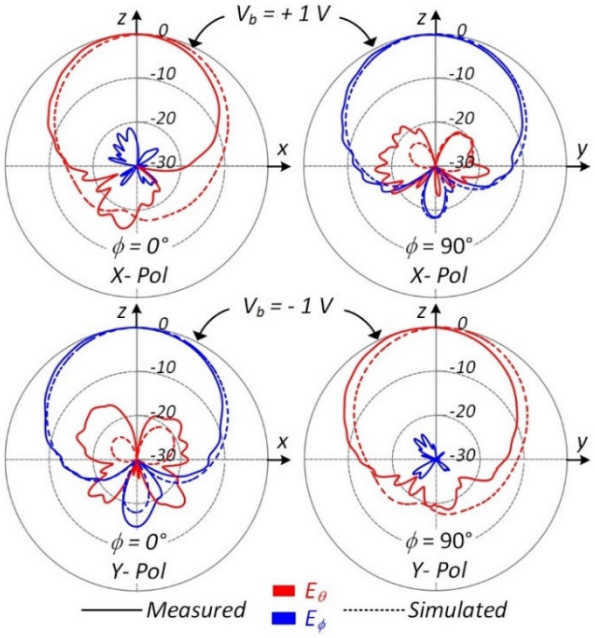

Fig. 63. Measured and simulated normalized radiation patterns for the solid-state FPRA with a bias voltage magnitude of 1 V at 2.33 GHz.

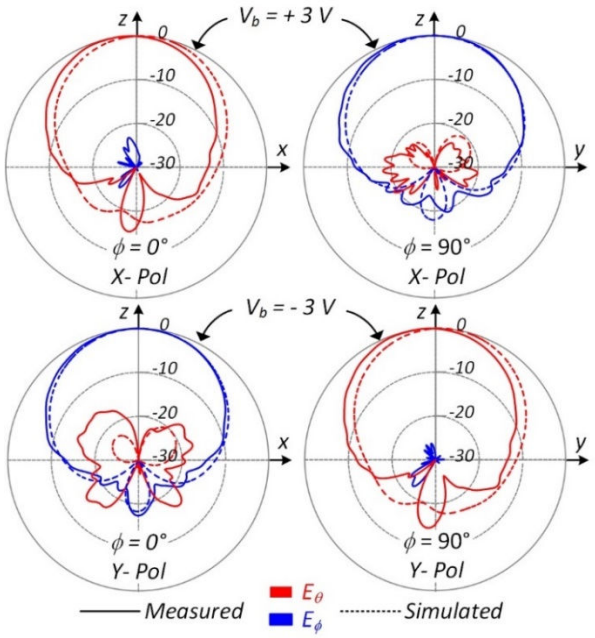

Fig. 64. Measured and simulated normalized radiation patterns for the solid-state FPRA with a bias voltage magnitude of 3 V at 2.37 GHz.

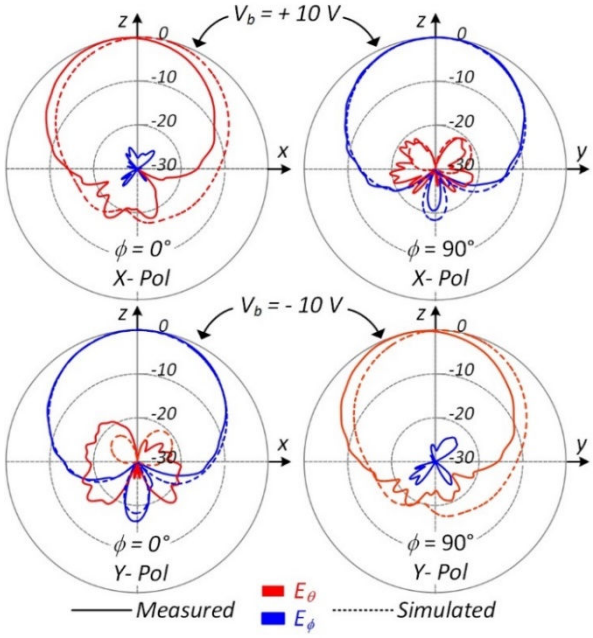

Fig. 65. Measured and simulated normalized radiation patterns for the solid-state FPRA with a bias voltage magnitude of 10 V at 2.433 GHz.

Fig. 66 displays the measured gain across the tuning range of 2.33 – 2.433 GHz using a bias voltage magnitude between 1 – 10 V. *X–pol* and *Y–pol* configurations are in good agreement where differences can be attributed to measurement error. At lower frequencies, where the bias voltage magnitude is low, the gain suffers from larger values of R_f than desired. As the bias voltage increases (increasing the resonant frequency), the value of R_f drops as the current across the RF PIN diodes increases to more desired values. The reduced R_f ohmic losses promote the increase in gain at higher frequency reconfiguration states. The simulated radiation efficiency of 16.5 – 18 % (Fig. 67) shows ohmic loss are still hindering radiation performance. Fig. 68 illustrates the solid-state FPRA electrical size ratio at bias voltage magnitudes of 1 – 20 V (20 V has been included

for completeness). The solid-state FPRA operates near the resonant frequency of a traditional patch antenna showing that the series capacitances and inductances at play nearly negate each other.

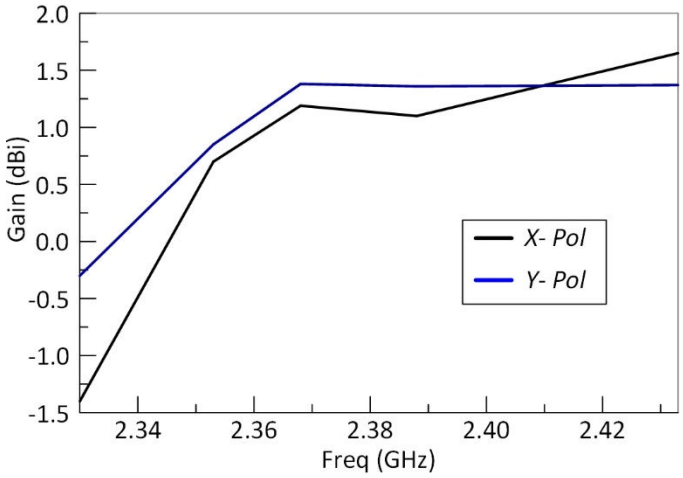

Fig. 66. Measured gain for the solid-state FPRA across the tuning range achieved using a bias voltage magnitude between 1 – 10 V.

The solid-state FPRA presented in this section exhibits both frequency and polarization diversity through a single control voltage. DC circuit biasing and complexities are reduced with the PIN diode/varactor configuration shown in Fig. 52. Excessive heating on the integrated chip resistor forces a limited tuning range of 100 MHz. The resistor heating also limits the potential number of RF PIN diodes across each gap and causes the radiation efficiency/gain to suffer from large ohmic losses. The high DC control power requirements to operate this antenna (even in the current state with no cooling mechanism)

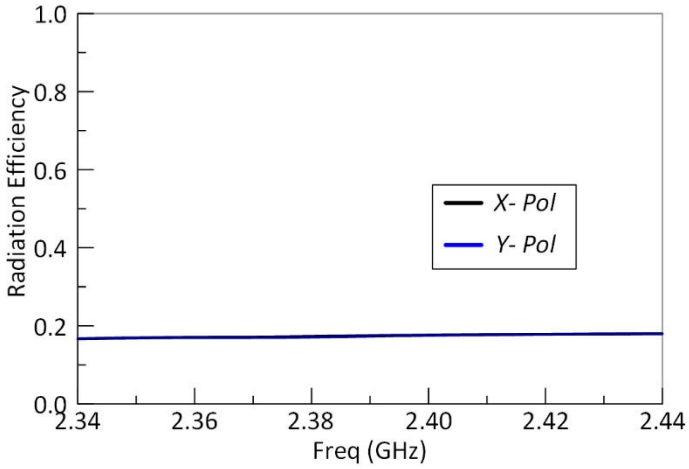

Fig. 67. Simulated radiation efficiency for the solid-state FPRA across the tuning range achieved using a bias voltage magnitude between 1 – 10 V.

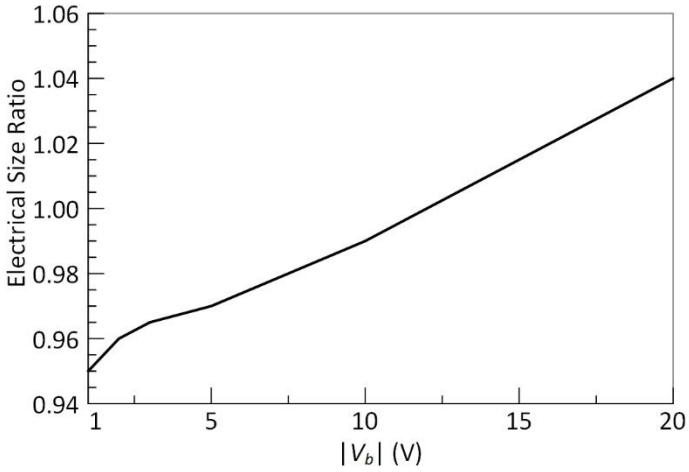

Fig. 68. Electrical size ratio for the solid-state FPRA across the bias voltage magnitude range from 1 – 20 V.

limit the antenna's use in many applications. This antenna can greatly benefit from relaxing the single control voltage requirement. This will significantly reduce the power requirements and allows the utilization of more RF PIN didoes to increase radiation

performance. Also, the full bias voltage magnitude range can be used to increase the tuning range. However, multiple control voltages will increase the bias line schemes complexity and potentially alter the crossed antenna design itself. While this more complex solid-state FPRA antenna design should be explored in the future, the purposes of this report require only a simple control scheme as presented.

4.3 Hybrid FPRA

The findings in the previous chapter for the PRA design proved a liquid metal switch could provide linear polarization switching with minimal impacts on radiation performance (gain and efficiency). This chapter has shown that low-loss, varying strength dielectric fluids are capable of achieving a large frequency tuning range, in addition to polarization switching, with good radiation performance. The availability and/or existence of this dielectric fluids are in question making this solution unrealistic at the time of this work. A solid-state solutions incorporating varactor and RF PIN diodes demonstrated a realistic solution with current technologies, however, high power requirements, limited tuning range, and low radiation efficiency limit usage in many wireless applications. In this section, a novel hybrid approach combining reconfiguration techniques to mitigate power requirements and increases radiation performance proceeds.

4.3.1 Concept and Modeling

Fig. 69 presents a hybrid FPRA solution which incorporates a liquid metal switch and solid-state packaged varactor diodes to reconfigure polarization and frequency states. The liquid metal switch design mimics the liquid metal PRA where a superstrate layer of dimensions $W_s \times W_s \times H_s$ and material properties $\varepsilon_{rs} = \varepsilon'_{rs}\left(1 - j\tan\delta_{ds}\right)$ with ellipsoidal

cross-section channels of dimensions H_c and W_c forms the SIFN. The SIFN dimensions reduced the fringing field exposure to the lossy dielectric material composing the superstrate for improved radiation performance. The two sections of EuGI spanning the antenna arms of width W electrically connects appropriate arms to the central feeds section to excited *X–pol* or *Y–pol* configurations. Fig. 69 depicts generalized EuGI inlets and outlets for simplicity in the diagram. Varactor diodes are placed across separate gap discontinuities away from the SIFN to introduce a variable series capacitance C_v and means of frequency tuning. The number of varactors utilized will be discussed in the next subsection. The varactors are oriented such that a positive bias voltage V_b applied to the center feed section places a reverse voltage (voltage drop from cathode to anode) when corresponding gaps in the SIFN are switched "on" with EuGI (i.e. the filled EuGI channels are both RF and DC switches). When the gaps in the SIFN are "off" (no EuGI) no voltage drop exist across the diodes. RF choke bias line ground the microstrip arms at DC to achieve this reverse bias voltage condition. This hybrid solution requires zero DC power to enable frequency tuning since the varactors operate on an electrostatic voltage with no integrate chip resistor. Thus, the full range of varactor capacitances (and tuning frequencies) can be achieved in this design.

As a short recap, the electrostatic bias voltage magnitude controls the resonant frequency and the EuGI sectional positions control the polarization states. Although this approach will need two control voltages (one for a peristaltic pump to position the EuGI sections and one to operate the varactors), the biasing scheme remains simple. Furthermore, the varactors require no current to operate and draw zero power from the

controller's power source, reducing potential cooling system complexities. Thus, the simplicity of control for this reconfiguration solution remains valid.

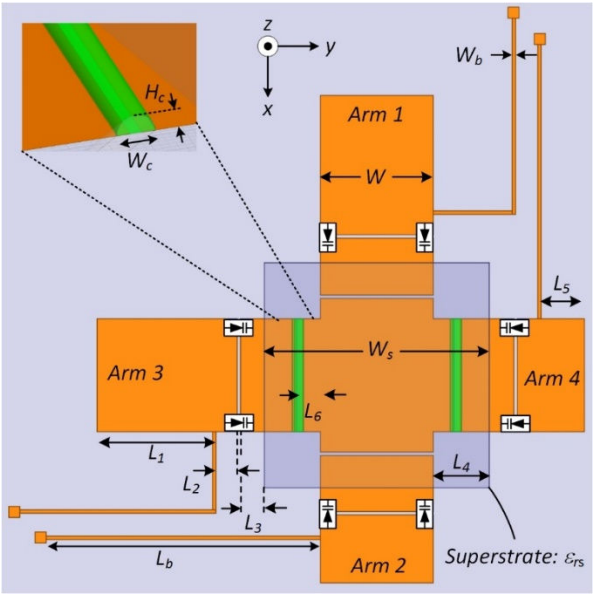

Fig. 69. Hybrid FPRA using liquid metal fluidic channels for polarization switching and varactors for frequency tuning.

Fig. 70 illustrates the circuit model based off a combination of the liquid metal PRA (Fig. 37) and the solid-state FPRA (Fig. 53) models. The gaps loaded by EuGI are modeled as equivalent transmission lines loaded by the SIFN superstrate. The transmission lines denoted T_U, T_L, and T_F represent the lines of width W unloaded by the SIFN superstrate, the lines of width W loaded by the SIFN superstrate, and the lines of width $W + 2L_6$ loaded by the SIFN superstrate of the central feed section, respectively. The varactors are classically modeled as a series resistance R_{vi}, the varactor internal resistance, variable capacitor C_v, and inductance L, from packaging. These values are found in

datasheets. Again, a shunt inductance L_b (computed from full-wave simulations) models the bias lines and a series inductance L_{pr} (computed from basic wire inductance equations) models the feed probe. The presence of both series capacitive coupling and series inductance means this antenna can operate electrically larger or smaller than its traditional counterpart (diodes removed and gaps filled). The only ohmic losses present are the varactor internal resistance R_{vi} (much smaller than R_f).

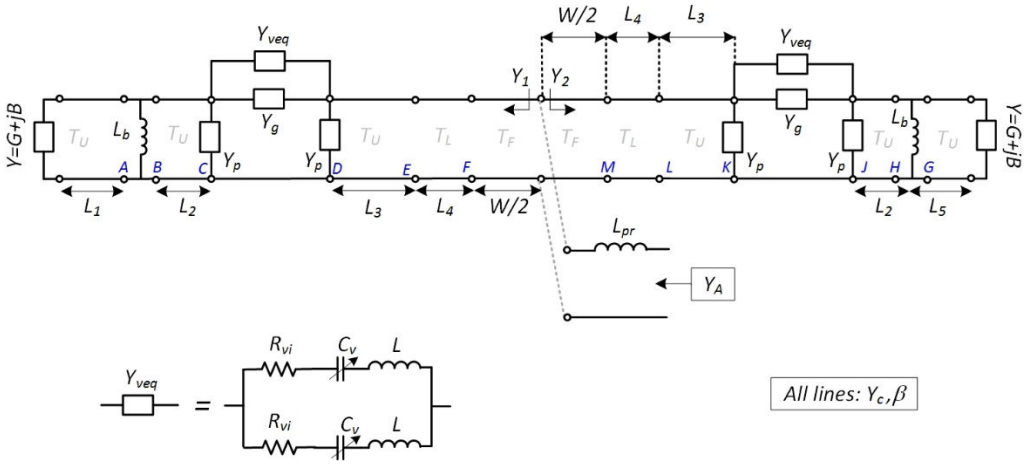

Fig. 70. Hybrid FPRA circuit model.

4.3.2 Design and Prototype

As a proof-of-concept demonstration a hybrid FPRA static version was fabricated on Duriod 5880 (ε_r = 2.2, tanδ = 0.0009, h = 1.58 mm) by creating solder bridges (gaps filled with solder) across appropriate gaps for *X–pol* and *Y–pol* configurations in two separate antennas as seen in Fig. 71. The conductivity of solder closely resembles the conductivity of EuGI and provides a fair comparison to the performance expected using

EuGI. In order to account for the SIFN loading effect, a PDMS ($\varepsilon'_{rs} \sim 2.66$, $\tan\delta_s \sim 0.04$) superstrate layer of dimensions $W_s = 20$ mm and $H_s = 2$ mm was fabricated to act as the SIFN. The PDMS layer was created by pouring liquid PDMS over the entire FPRA top surface (with solder bridges). The liquid PDMS was allowed to cool then cut to specifications. Thus, these static "channels" created by the solder bridges are of unknown and non-uniform dimension, however can be approximated by $W_c = 1$ mm, $H_c = 0.5$ mm. The remaining dimension (in mm) are: $L_1 = 10.4$, $L_2 = 2$, $L_3 = 2.15$, $L_4 = 5$, $L_5 = 4$, $L_6 = 1.85$, $W = 10$, $L_b = W_b = 0.3$. The same varactor diodes [27] utilized in the previous FPRA design with $L = 0.7$ nH, $R_{vi} = 0.35$ Ω, and $1.77 \text{ pF} < C_v < 9.24$ pF (roughly 5:1 ratio capacitance range) for $30 \text{ V} > V_{var} > 0$ V are used.

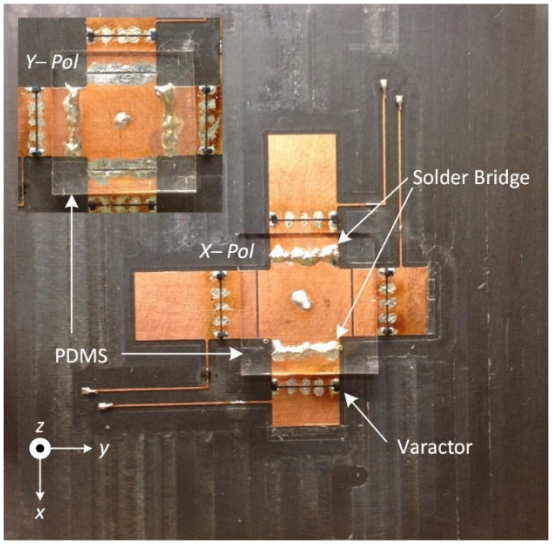

Fig. 71. Static Prototype for the hybrid FPRA where appropriate gaps have been solder together and a PDMS layer cure over the gaps to mimic a fluidic channel.

The varactors are mounted using a pick-and-place machine, solder paste, and heat gun near 250° C. The varactors were exposure to this heat (above the specified non-operating temperature) for a brief period of time to reflow the solder paste. The varactor diode's internal resistance increased to approximately R_{vi} = 0.6 Ω in response to this heat. Although more varactors in parallel would reduce the ohmic loss from R_{vi}, only two varactor diodes are employed to avoid a resonance condition found using 3 – 5 varactors/gap. The resonance manifested from the $L - C_v$ parallel combination and caused an impedance mismatch to occur at a specific frequency in the tuning range. Using two varactors per gap increases the tuning range since smaller capacitance terms are achieved across the gaps.

Fig. 72 – Fig. 78 shows the measured reflection coefficient data comparted to simulated and circuit model results for the static hybrid FPRA prototype at a detailed sampling of tuning states (V_b = 0, 1, 3, 5, 10, 20, and 30 V). The analytical, simulated, and measured results are in close agreement and show a ~ 263 MHz center frequency tuning range from 2.362 – 2.625 GHz for *X–pol* and *Y–pol* configurations. The FBW are in close agreement and common for a resonant antenna (< 1.5 %).

Fig. 79 – Fig. 81 present the simulated and measured normalized radiation patterns for V_b = 0 , 10 and 30 V at the corresponding center frequencies for each reconfiguration state. The patterns demonstrate good linear polarization switching between *X–pol* and *Y–pol* states. The main beams resemble classic patch antenna performance and are nearly identical for all three reconfigurations states. The measured results show a reasonable maximum cross polarization level of -16.4 dBi which agree with results from the solid-

state PRA models (Table 2) and solid-state FPRA model. Differences in the simulated and measured results can be attributed to measurement tolerances and the measured prototype smaller ground plane size.

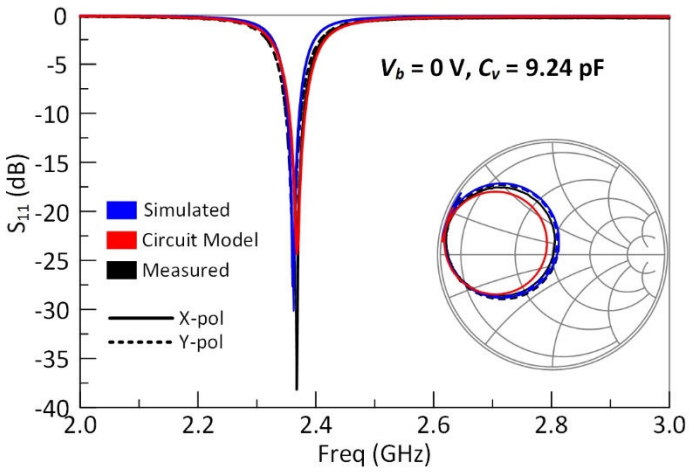

Fig. 72. Measured reflection coefficient for the static hybrid FPRA with a bias voltage magnitude of 0 V compared to circuit model and simulated results.

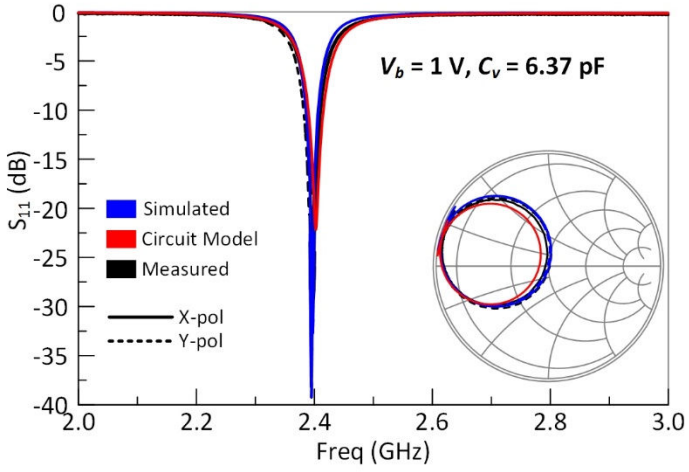

Fig. 73. Measured reflection coefficient for the static hybrid FPRA with a bias voltage magnitude of 1 V compared to circuit model and simulated results.

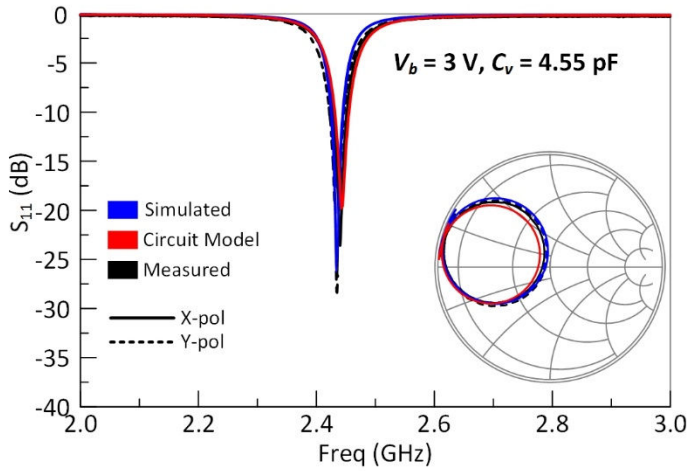

Fig. 74. Measured reflection coefficient for the static hybrid FPRA with a bias voltage magnitude of 3 V compared to circuit model and simulated results.

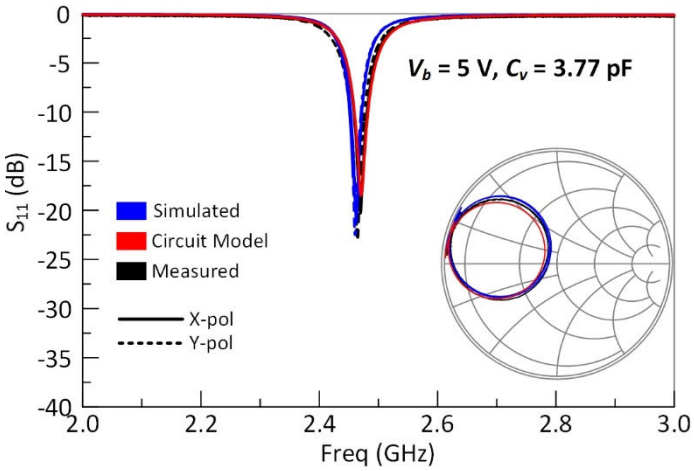

Fig. 75. Measured reflection coefficient for the static hybrid FPRA with a bias voltage magnitude of 5 V compared to circuit model and simulated results.

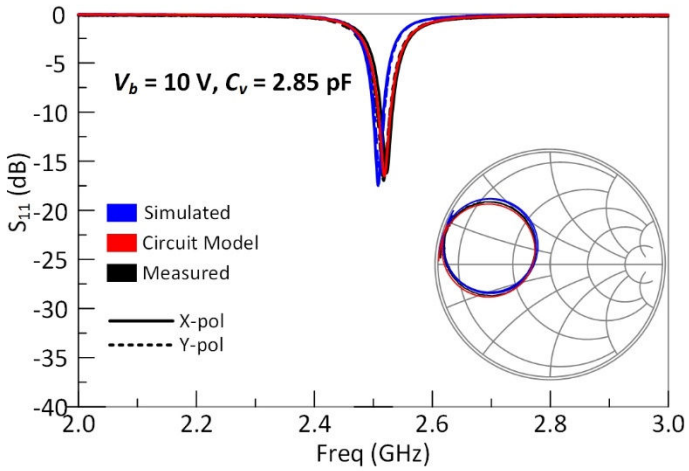

Fig. 76. Measured reflection coefficient for the static hybrid FPRA with a bias voltage magnitude of 10 V compared to circuit model and simulated results.

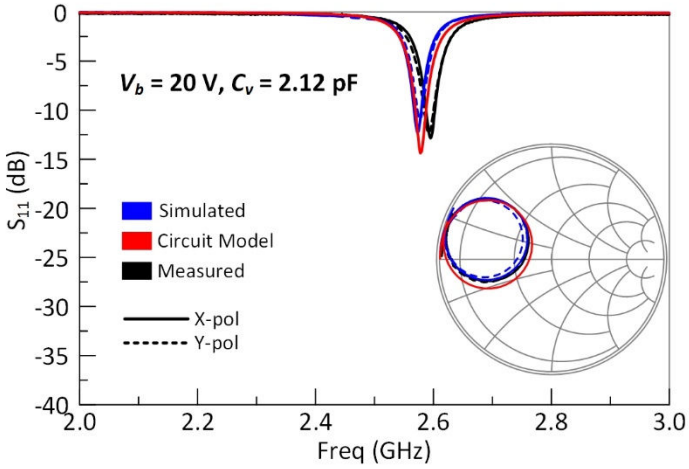

Fig. 77. Measured reflection coefficient for the static hybrid FPRA with a bias voltage magnitude of 20 V compared to circuit model and simulated results.

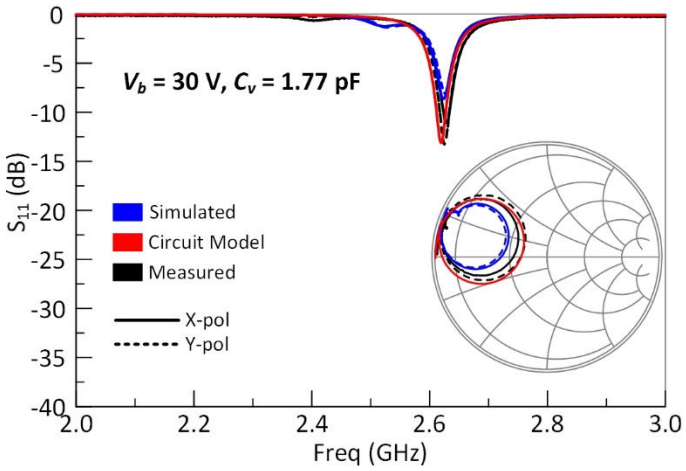

Fig. 78. Measured reflection coefficient for the static hybrid FPRA with a bias voltage magnitude of 30 V compared to circuit model and simulated results.

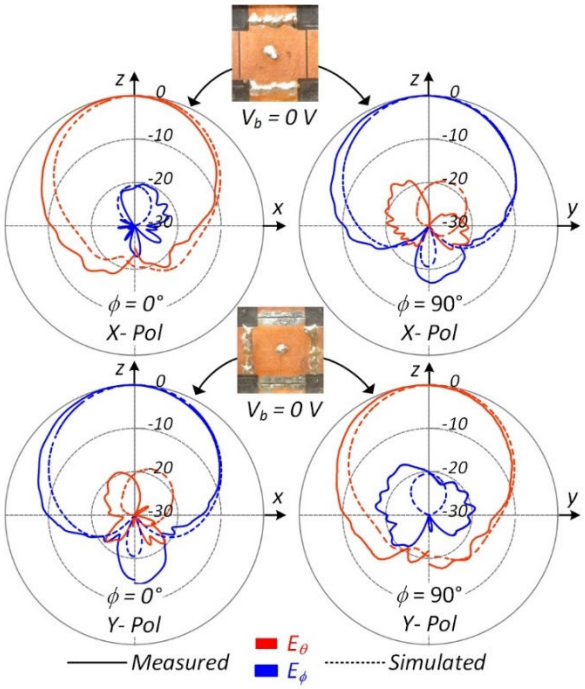

Fig. 79. Measured and simulated normalized radiation patterns for the static hybrid FPRA with a bias voltage magnitude of 0 V at 2.365 GHz.

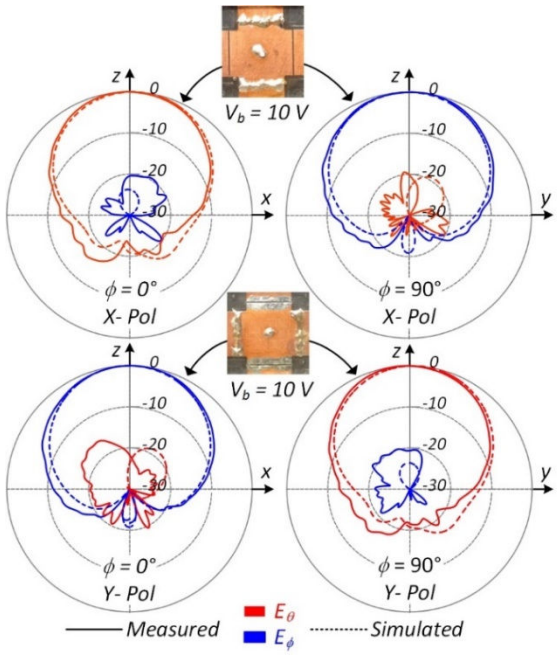

Fig. 80. Measured and simulated normalized radiation patterns for the solid-state FPRA with a bias voltage magnitude of 10 V at 2.52 GHz.

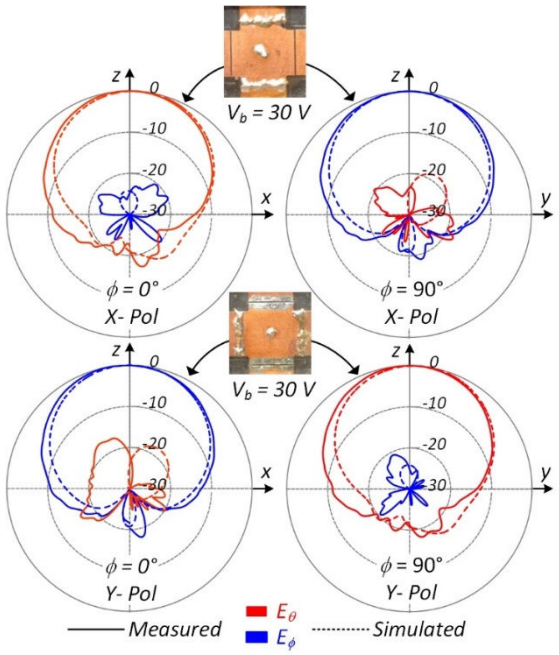

Fig. 81. Measured and simulated normalized radiation patterns for the solid-state FPRA with a bias voltage magnitude of 30 V at 2.63 GHz

Fig. 82 displays the measured gain across the tuning range of 2.362 – 2.625 GHz using a bias voltage between 0 – 30 V. *X–pol* and *Y–pol* configurations are in good agreement where difference can be attributed to measurement error. The gain remains fairly constant and fluctuates by less than 0.7 dB across the tuning range. The ~ 3.8 dBi average gain between all reconfigurations states shows a large increased from the solid-state FPRA model since many sources of ohmic losses were removed. Further, the simulated results from Fig. 83 show an efficiency of ~ 40 % across the reconfiguration states, more than doubling the efficiency from the solid-state FPRA. Fig. 84 shows the electrical size is near that of a traditional patch antenna over all reconfiguration states.

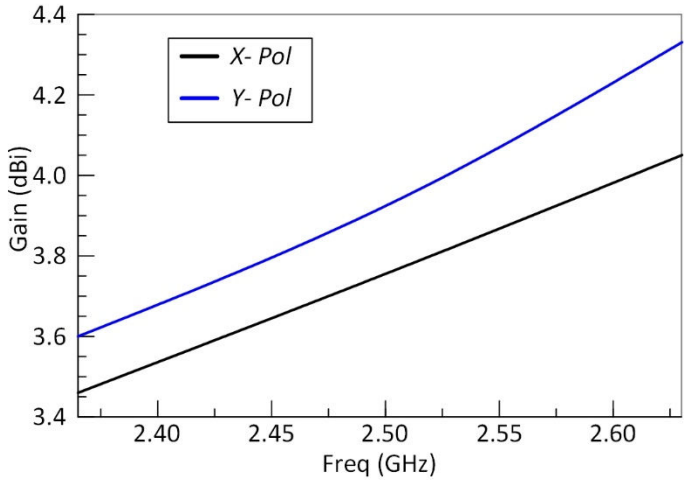

Fig. 82. Measured gain for the hybrid FPRA across the frequency tuning range achieved using a bias voltage magnitude between 0 – 30 V.

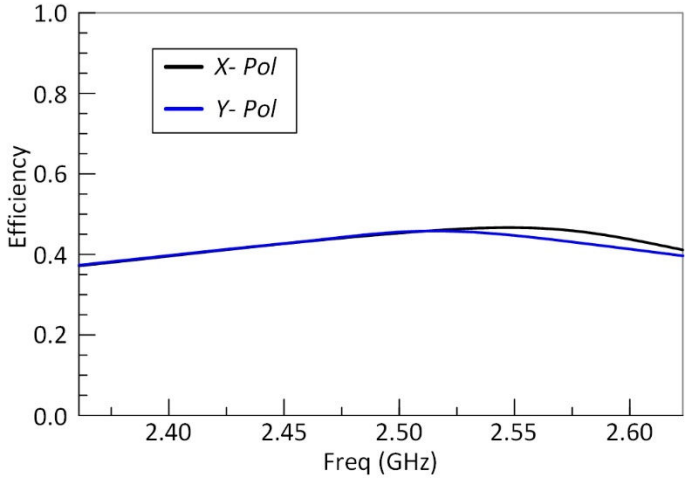

Fig. 83. Simulated efficiency for the hybrid FPRA across the frequency tuning range achieved using a bias voltage magnitude between 0 – 30 V.

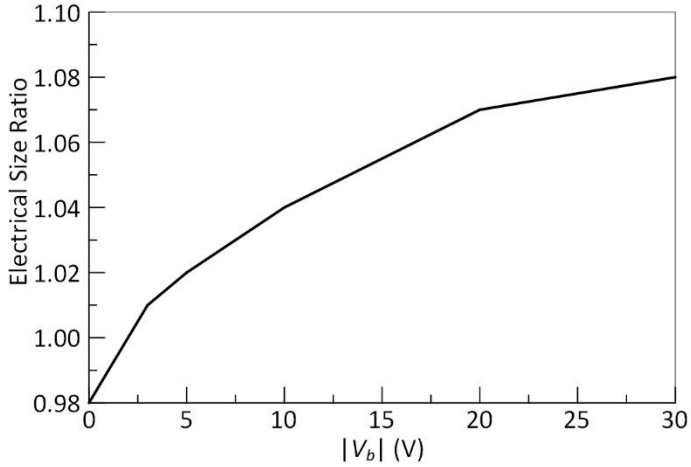

Fig. 84. Electrical size ratio for the hybrid FPRA across the bias voltage magnitude range from 1 – 30 V

4.4 Discussion

The FPRA reconfiguration mechanisms presented facilitate both polarization and frequency diversity through simple control schemes. As with the PRA design, these

mechanisms were found to have design trade-offs, limitations, and advantages between them which are summarized in Table 4 with respect to seven main performance metrics: (1) frequency tuning range, (2) electrical size ratio, (3) measured gain, (4) simulated efficiency, (5) cross polarization levels (measured), (6) DC control power requirements, (7) switching speed. In (2), (3), and (4) the average value among all reconfiguration states for each mechanisms is listed.

The fluidic FPRA achieves the largest tuning range and simulated efficiency. The average efficiency of 60.2% assumes $tan_{\delta l} = 0.02$ since lossless fluids may never be realistic. The absence of inductive coupling (from no package inductors) in the fluidic FPRA model leads to the largest electrical size and aperture efficiency. However, fluids with widely varying dielectric constants and loss tangents < 0.02 are not currently available. As collaboration between material science and RF/microwave engineers increases, such fluids may manifest and the analytical and simulated models developed in this work will help design future fluidic FPRAs.

Table 4. Performance summary for the FPRA with the fluidic, solid-state, and hybrid reconfiguration mechanisms.

	Frequency Tuning Range	Electrical Size Ratio	Measured Gain	Simulated Efficiency	Cross polarization level	DC Control Power Requirements	Switching Speed
Fluidic	700 MHz	1.35	N/A	60.2 %	N/A	N/A	~ ms
Solid-State	100 MHz	0.98	0.79 dBi	17.2 %	-15 dB	1.82 W	~ μs
Hybrid	263 MHz	1.03	3.87 dBi	41.7 %	-16.4 dB	0 mW	N/A

The solid-state FPRA metrics listed are for the realizable bias voltage magnitudes up to 10 V where no cooling mechanism is necessary. The solid-state FPRA has limited performance and functionality as the integrated chip resistor heats up excessively for high bias voltage magnitudes and draws large power outputs from the source. The radiation performance suffers since a limited number of RF PIN diodes per gap are used in order to reduce power dissipation on the chip resistor. Removing the single control voltage requirement would reduce power requirements, allow more PIN diodes to be used across each gap, increase radiation performance, and expand the tuning range. However, the complexities from introducing more control voltages and bias lines on the antenna could alter the radiation patterns and/or completely change the base crossed antenna structure. This is a topic for a separate project and will not be discussed further.

The hybrid FPRA demonstrates a viable solution with current technologies at play. Although the fluidic FPRA may outperform the hybrid counterpart one day, the hybrid solution shows good radiation performance (3.87 dBi average measured gain and 41.7% average measured efficiency) with a limited number of varactors employed. The hybrid model gain and efficiency can be increased by utilizing a larger number of varactors across each gap. In order to do this, varactors with different C_v ranges and package inductance are need to avoid the mentioned resonance condition in the operating frequency range. Alternatively, the FPRA can be tuned to operate away from the 2.4 – 2.5 GHz ISM band to avoid this unwanted LC resonance. Although no dynamic testing was completed with liquid metal EuGI, the static prototype's performance with solder bridges represents a good estimation of what the dynamic performance would be since EuGI and solder share

similar conductivities. Furthermore, a joint effort between the author and a graduate student in material science at the University of Illinois will produce dynamic testing with EuGI in the near future.

CHAPTER V

CONCLUSION

This work demonstrates a hybrid approach for frequency and polarization diversity in a crossed microstrip antenna design. A surface integrated fluidic network with fluidic channels guides liquid metal sections to appropriate locations on the antenna and excites *X–pol* or *Y–pol* configurations. This liquid metal approach was use in the polarization-only reconfigurable antenna design and achieved radiation performance similar to an unaltered rectangular patch antenna. Varactors integrated on the antenna's surface create a variable series capacitance along the antenna to control the resonant frequency. Ohmic losses introduced by the varactors decreased radiation performance. These losses are acceptable and considered necessary trade-offs to achieve the desired reconfiguration performance with available technologies. This work also presented a means of reducing ohmic losses in both PRA and FPRA iterations by incorporating more RF PIN and varactor diodes on the antenna. Increasing more RF PIN diodes creates a design trade-off between power requirements and radiation performance when minimizing the number of control voltages (and bias lines). More varactors do not create this trade-off as they operate on an electrostatic voltage. Variable low-loss dielectric fluids are alternatives to the varactor and liquid metal switch hybrid approach and achieve nearly unaltered patch antenna performance. However, such fluids are unavailable at the time of this work. This encourages joints efforts from material science and RF/microwave engineers to explore and design low-loss, variable dielectric fluids. The analytical and simulation models

developed in this work can be used as these fluids manifest to design future FPRAs. The circuit models developed in this work for each PRA and FPRA design iterations are in good agreement to full-wave simulations and measurements. The principles from these models can be applied to other reconfigurable microstrip antenna designs to help understand the tuning mechanism impacts on the antenna's performance.

REFERENCES

[1] S. V. Hum and X. Hui Yuan, "Analysis and Design of a Differentially-Fed Frequency Agile Microstrip Patch Antenna," *IEEE Trans. Antennas Propag,* vol. 58, pp. 3122-3130, 2010.

[2] T. Jia-Fu and R. Jeen-Sheen, "Reconfigurable Square-Ring Microstrip Antenna," *IEEE Trans. Antennas Propag.,* vol. 61, pp. 2857-2860, 2013.

[3] M. N. M. Kehn *et al.*, "Reconfigurable Loaded Planar Inverted-F Antenna Using Varactor Diodes," *IEEE Antennas Wireless Propag. Lett. ,* vol. 10, pp. 466-468, 2011.

[4] Y. Yufeng *et al.*, "An Electrically Small Frequency Reconfigurable Antenna With a Wide Tuning Range," *IEEE Antennas Wireless Propag. Lett. ,* vol. 10, pp. 103-106, 2011.

[5] B. Li and Q. Xue, "Polarization-Reconfigurable Omnidirectional Antenna Combining Dipole and Loop Radiators," *IEEE Antennas Wireless Propag. Lett.,* vol. 12, pp. 1102-1105, 2013.

[6] M. S. Parihar *et al.*, "Polarization reconfigurable microstrip antenna," in *Asia-Pacific Microw. Conf. Proc.*, 2009, pp. 1918-1921.

[7] C. Rui-Hung and J. S. Row, "Single-Fed Microstrip Patch Antenna With Switchable Polarization," *IEEE Trans. Antennas Propag.,* vol. 56, pp. 922-926, 2008.

[8] Y. Xue-Xia *et al.*, "A Polarization Reconfigurable Patch Antenna With Loop Slots on the Ground Plane," *IEEE Antennas Wireless Propag. Lett.,* vol. 11, pp. 69-72, 2012.

[9] C. Chi-Yuk *et al.*, "Frequency-Reconfigurable Pixel Slot Antenna," *IEEE Trans. Antennas Propag.,* vol. 60, pp. 4921-4924, 2012.

[10] G. H. Huff and J. T. Bernhard, "Integration of packaged RF MEMS switches with radiation pattern reconfigurable square spiral microstrip antennas," *IEEE Trans. Antennas Propag.,* vol. 54, pp. 464-469, 2006.

[11] T. J. Jung *et al.*, "Polarization reconfigurable antenna on RF-MEMS packaging platform," in *Asia-Pacific Microw. Conf. Proc.*, 2009, pp. 579-582.

[12] G. H. Huff *et al.*, "A Frequency Reconfigurable Dielectric Resonator Antenna Using Colloidal Dispersions," *IEEE Antennas Wireless Propag. Lett.,* vol. 9, pp. 288-290, 2010.

[13] G. H. Huff and S. Goldberger, "A Coaxial Stub Microfluidic Impedance Transformer (COSMIX)," *IEEE Microw. Wireless Compon. Lett.,* vol. 20, pp. 154-156, 2010.

[14] S. A. Long and G. H. Huff, "A Fluidic Loading Mechanism for Phase Reconfigurable Reflectarray Elements," *IEEE Antennas Wireless Propag. Lett.,* vol. 10, pp. 876-879, 2011.

[15] J. D. Barrera and G. H. Huff, "Analysis of a Variable SIW Resonator Enabled by Dielectric Material Perturbations and Applications," *IEEE Trans. Microw. Theory Tech.,* vol. 61, pp. 225-233, 2013.

[16] A. J. King *et al.*, "Microfluidically Switched Frequency-Reconfigurable Slot Antennas," *IEEE Antennas Wireless Propag. Lett. ,* vol. 12, pp. 828-831, 2013.

[17] M. Kelley *et al.*, "Frequency reconfigurable patch antenna using liquid metal as switching mechanism," *Electronics Letters,* vol. 49, pp. 1370-1371, 2013.

[18] D. M. Pozar, *Microwave engineering*. Hoboken, NJ: J. Wiley, 2005.

[19] P. Bhartia and I. J. Bahl, *Millimeter wave engineering and applications*. New York :: Wiley.

[20] C. A. Balanis, *Antenna theory: analysis and design*. Hoboken, NJ: John Wiley, 2005.

[21] Skyworks. (2012). *Data Sheet: SMP1345 Series: Very Low Capacitance, Plastic Packaged Silicon PIN Diodes*. Available: www.skyworksinc.com. 12/4/2014.

[2.2] Ansoft, "HFSS v15.0," Pittsburg, PA, 2009.

[23] H. Y. Yang *et al.*, "Microstrip open-end and gap discontinuities in a substrate-superstrate structure," *IEEE Trans. Microw. Theory Techn.,* vol. 37, pp. 1542-1546, 1989.

[24] N. G. Alexopoulos and W. Shih-Chang, "Frequency-independent equivalent circuit model for microstrip open-end and gap discontinuities," *IEEE Trans. Microw. Theory Techn.,* vol. 42, pp. 1268-1272, 1994.

[25] U. Kaatze, "Complex permittivity of water as a function of frequency and temperature," *J. of Chemical and Eng. Data,* vol. 34, pp. 371-374, 1989.

[26] M. D. Dickey *et al.*, "Eutectic Gallium-Indium (EGaIn): A Liquid Metal Alloy for the Formation of Stable Structures in Microchannels at Room Temperature," *Advanced Functional Materials,* vol. 18, pp. 1097-1104, 2008.

[27] Skyworks. (2013). *Data Sheet: SMV1405 to SMV1430 Series: Plastic Packaged Abrupt Junction Tuning Varactors*. Available: www.skyworksinc.com. 12/4/2014.

APPENDIX A

HFSS SHEET INDUCTANCE

In order to simulate RF PIN and varactor diodes with HFSS, 2D sheets where place in the appropriate locations on the antenna where the physical diode would be and assigned a parallel RLC impedance boundary condition. A separate sheet (and separate boundary condition) is necessary for each diode component since the diodes are models as series components. Fig. 85 show the 2D sheets with applied boundary conditions for RF PIN diodes. The forward bias diodes have a sheet for the series inductance L and forward resistance R_f while the negative bias diodes replace the forward resistance with a reverse capacitance C_r. The values for R_f, C_r, and L in the boundary condition are expresses in terms of resistance/square, capacitance/square, and inductance/square, respectively. Thus, the sheet geometries are perfect squares.

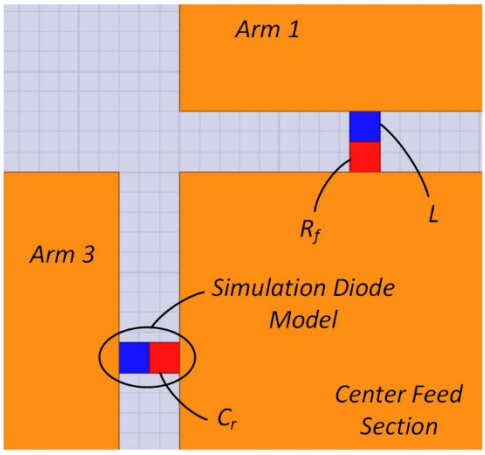

Fig. 85. HFSS diode simulation model.

When modeling the diodes in this manor, and additional inductance in the simulation model arises from 2D sheets. This inductance originates from the RF currents flowing across the small, narrow sheets allow RF current to flow across them. The actual diodes inductance is the equivalent inductance between the terminals (includes inductances from packaging and the device itself). Thus, the additional inductance from the 2D sheets in simulation, denoted L_{sheet}, cause a mismatch between simulated and measured data if not account for. To remove this inductance from the simulation model the boundary condition for the diode inductance in HFSS can be assigned a value of $L - L_{sheet}$. The value of L_{sheet} can be computed from the additional simulation model shown in Fig. 86.

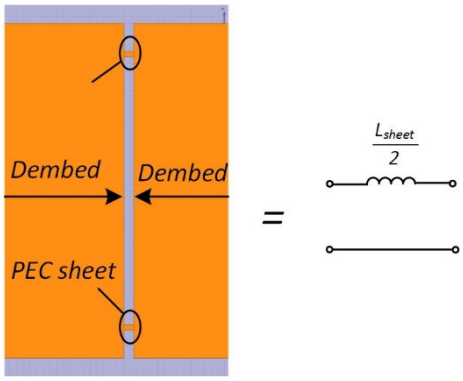

Fig. 86. Simulation model for computing sheet inductance.

Two transmission lines of width W, separated by a gap of width g including 2D sheets for the diodes with no impedance boundaries forms the simulation model. The post-processing results are de-embedded to the gap edges. The inductance can be computed from the input impedance at any ports from (A.1).

$$\frac{L_{sheet}}{2} = \frac{\mathrm{Im}(Z_{in})}{2\pi f} \tag{A.1}$$

This concept can be generalized to any number of diodes (sheets), n_d, placed along the gap by (A.2).

$$\frac{L_{sheet}}{n_d} = \frac{\mathrm{Im}(Z_{in})}{2\pi f} \tag{A.2}$$